Spring 2018

Chemistry, design, and processing of two-stage TRIP steel

Daniel M. Field

Department: Materials Science and Engineering

Recommended Citation

Field, Daniel M., "Chemistry, design, and processing of two-stage TRIP steel" (2018). *Doctoral Dissertations*. 2672.
https://scholarsmine.mst.edu/doctoral_dissertations/2672

CHEMISTRY, DESIGN, AND PROCESSING OF TWO-STAGE TRIP STEEL

by

DANIEL MORYE FIELD

A DISSERTATION

Presented to the Faculty of the Graduate School of the

MISSOURI UNIVERSITY OF SCIENCE AND TECHNOLOGY

In Partial Fulfillment of the Requirements for the Degree

DOCTOR OF PHILOSOPHY

in

METALLURGICAL ENGINEERING

2018

Approved

David C. Van Aken, Advisor
Matthew J. O'Keefe
Ronald J. O'Malley
William G. Fahrenholtz
Julia E. Medvedeva

PUBLICATION DISSERTATION OPTION

This dissertation has been prepared in the form of three manuscripts for publication. Paper I, pages 18-53 were published February 2017 online and in print in Metallurgical and Materials Transactions A volume 48A, May 2017. Paper II, pages 54-92 has been prepared to the Metallurgical and Materials Transactions A format and was submitted for review September 2017, and accepted with minor revisions. Paper III, pages 93-136 have been prepared in the style utilized by the Materials & Design. The Introduction, Literature Review, and Proposed Future Alloy Design provide supplemental information and discussion to the dissertation topic and have been formatted to Missouri University of Science and Technology specification.

ABSTRACT

A regular solution model was developed to calculate the chemical driving force for α-martensite formation, $\Delta G_{Chem}^{\gamma\rightarrow\alpha}$. A model for the strain energy, $\Delta G_{str}^{\gamma\rightarrow\alpha}$, was formulated utilizing the Young's modulus (E), lattice misfit squared (δ^2), and molar volume (Ω) which opposed the chemical driving force for α-martensite formation. The M_S^{α} was determined at a temperature at which $\Delta G_{Chem}^{\gamma\rightarrow\alpha} + \Delta G_{str}^{\gamma\rightarrow\alpha} = 0$. In conjunction with a previously developed ε-martensite model, a means of predicting the volume fraction of γ-austenite was determined; and it was shown that for values of $\Delta Ms < 0$, defined as $Ms^{\varepsilon} - Ms^{\alpha}$ produced the greatest amounts of retained γ-austenite in the as quenched microstructure. These models were tested, and confirmed, with a new alloy formulated to produce a steel with chromium replacing the traditional aluminum to obtain a $\Delta Ms = -100$ C° that exhibited the two-stage TRIP behavior. From this substitution the dynamic strain aging response could be mitigated through $M_{23}(C,N)_6$ precipitation trapping carbon and nitrogen. The work hardening behavior of these steels was found to be due to the Stage II (ε→α) martensitic reaction and not the dynamic strain aging of the steels. Eight medium-Mn steels were processed and it was found that when the intrinsic stacking fault energy was less than 10.5 mJ/m^2 the two-stage TRIP response was activated. Empirical relationships for the strength and ductility were determined for the two-stage TRIP steels. The developed models have been used to optimize alloy composition and a designed steel with composition Fe-13.8Mn-1.0Si-3.0Cr-0.15C-0.003N (wt. pct.) is recommended for future investigation.

ACKNOWLEDGMENTS

This work has been supported by the Kent D. Peaslee Steel Manufacturing Research Center (PSMRC) as part of the project development of New 3rd Generation Advanced High Strength Steels.

First and foremost I would like to express my extreme gratitude to my wife Melissa Field for being a supporting and understanding partner. Throughout this entire process she has supported me with her unwavering faith in me and being a sounding board for my troubles. I also appreciate all of the sacrifices my wife and children have made to make it possible for me to finish my degree. I am enormously grateful to Dr. David. C. Van Aken for his guidance, instruction, and encouragement during my time as a student and a researcher. His dedication to education has been an inspiration. I would like to thank Dr. Ronald J. O'Malley, Dr. Matthew J. O'Keefe, Dr. William G. Fahrenholtz, and Dr. Julia E. Medvedeva for their role as committee members. Further gratitude is extended to Todd M. Link at U.S. Steel, Eric Gallo of Nucor Steel, Narayan Pottore and Bernard Chukwulebe of ArcelorMittal, and Luis Garza of AK Steel for their advice, support, and technical discussion as acting industry representatives of the Kent D. Peaslee Steel Manufacturing Research Center.

I would like to extend my appreciation to the staff of the Materials Research Center including Dr. Clarissa Wisner and Dr. Jingjing Qing for their guidance and training in electron microscopy and Dr. Eric Bohannon for conducting numerous X-ray diffraction experiments in support of this project. I also wish to thank Dr. Mingzhi Xu for his assistance in the research foundry, assisting with the casting of the alloys investigated, and Dr. Mario Buchely for his assistance with hot rolling and high strain rate testing of the alloys. I also acknowledge my colleagues, Scott Pisarik for his initial ground work on the two-stage TRIP steels as well as Terrell Webb, Seth Rummel, Viraj Athavale, and Jie Wan. The Materials Science and Engineering Department staff of Teneke Hill and Denise Eddings were integral in their daily help in overcoming life's daily hurdles. Undergraduate student assistance was provided by Travis Zerna, Jackson Riley, and Sonya Snyder, who have helped me be in two or more places at once.

TABLE OF CONTENTS

Page

SECTION

PAPER

SECTION

LIST OF ILLUSTRATIONS

PAPER I

PAPER II

PAPER III

SECTION

LIST OF TABLES

PAPER I

PAPER II

PAPER III

SECTION

1. INTRODUCTION

The automotive industry is currently working towards reducing its carbon footprint, increasing both fuel economy and the crashworthiness of the average vehicle. The current benchmark standard is the corporate average fuel economy (CAFÉ) that defines the average vehicle obtain 54.5 miles per gallon by the year 2025 [1]. Many avenues have been explored and implemented to obtain this goal: improved aerodynamics, more efficient engines, and optimized component systems. Reducing the total weight of the vehicle by decreasing the gauge thickness of metallic components is another means to obtain the CAFÉ goals. Low density materials like aluminum, magnesium, and polymers are becoming more attractive to the automaker for light weighting. However, for steel to stay competitive with the strength to weight ratio of these lightweight metals the strength of the steel must exceed 900 MPa [2]. In an effort to increase energy absorbed upon impact and to maintain ease of manufacturing, these future high strength steels must also have significant ductility and formability.

The department of energy (DOE) has defined the breakthrough new generation of steels to obtain ultimate tensile strengths of 1500 – 1200 MPa, and respective ductility of 25 – 30 pct. Two potential means of obtaining the targeted properties that have been investigated: quench and partitioning (Q&P), and medium-Mn steels. Quench and partitioned steels have shown ultimate tensile strengths in excess of 1500 MPa with elongation to failure of 20 pct. [3]. Medium-Mn steels which exhibit the two-stage transformation induced plasticity (TRIP) character [4-11] have shown strengths in excess of 1200 MPa and elongation to failure of greater than 30 pct.

Recent work with elevated manganese steels in the range of 10-17 wt. pct., carbon contents of 0.05-0.3 wt. pct., 1-4 wt. pct. silicon and 0-2 wt. pct. aluminum [4-11] have been investigated to obtain lowered SFE that produce a metastable γ-austenite, that will TRIP to ε-martensite upon straining. Pisarik and Van Aken [12] showed that the ε-martensite subdivides the prior γ-austenite grain into thin ~3 μm bands during athermal formation. They also observed that α-martensite crystallites formed within ε-martensite are 1/3rd the size compared to the α-martensite formed from the direct γ→α reaction. The inherent grain refinement obtained from the two-stage response (γ→ε→α) is what provides an enhancement of strength and elongation in the form of a dynamic Hall-Petch effect. Work by Kinney et al. [13] showed that athermal α-martensite formed within the ε-martensite was twin related with 6-variates occurring.

McGrath et al. [4] investigated the work hardening mechanism and transformation mechanism of a 0.07C-2.8Si-15.3Mn-2.4Al-0.017N-balFe (in wt. pct.) two-stage TRIP steel and showed that the γ-austenite in the investigated steel underwent two consecutive martensitic transformations. The first reaction (Stage I) was the transformation of γ → ε-martensite, the Stage II reaction was the subsequent transformation of ε-martensite to α-martensite. McGrath determined that the work hardening exponent, n, and work hardening rate, K, reached a maximum of $n = 1.4$, and $K = 8{,}500$ MPa during the Stage II reaction. Work by Van Aken et al. [5] and Pisarik et al. [6] showed that the alloy content could be adjusted, specifically reducing Al, to obtain similar tensile response in the hot rolled condition, and the composition of the three alloys and properties are summarized in Table 1.1. McGrath et al. showed that the transition from Stage I → II occurred at ~4 pct. strain and it is interesting to note that in the ferrous shape memory alloys that contain ε-martensite a similar result was observed in the works by both Shin et al. [14] and Huang et al. [15]. They showed that the shape memory effect was degraded above 4 pct. strain due to the pinning of the Shockley partial dislocations from the intersection of two or more ε-martensite bands. This intersection has been related to α-martensite formation in the two-stage TRIP steels and is in agreement with the data that McGrath et al [4] presented.

Table 1.1. Composition, yield strength (YS), ultimate tensile strength (UTS), and total elongation of reported two-stage TRIP steels.

Source	**Composition (wt. pct.)**					**Properties**		
	C	**Si**	**Mn**	**Al**	**N**	**YS (MPa)**	**UTS (MPa)**	**%e_{tot}**
McGrath [4]	0.07	2.85	15.3	2.40	0.017	209	1165	34.4
Van Aken [5]	0.06	1.85	14.2	2.38	0.019	301	1217	28.5
Pisarik [6]	0.08	1.95	15.1	1.40	0.017	195	1058	29.1

These “hot band” properties also include very low yield strengths, on the order of 195 to 300 MPa. It has also been noted that the quantity of alloy in these steels pose a difficulty for conventional steelmaking processes. Manganese at elevated concentrations causes concern due to its high vapor pressure at steel making temperatures of 1600 °C. Aluminum due to its reactivity with oxygen and nitrogen can form inclusions like Al_2O_3 and AlN in the liquid steel leading to clogging of the submerged entry nozzle during casting causing throughput and quality concerns for the steel industry. There has therefore been extensive work [8, 16-18] on understanding the relative stability of the ε-martensite to the parent γ-austenite to guide future two-stage TRIP steel developments.

The utility of this being a means at which Mn content can be reduced and the steel processed to still obtain the two-stage TRIP response and properties defined by the DOE. The purpose of this work was to develop a means of understanding the relationship between chemistry, processing, microstructure and properties of developed two-stage TRIP steels through the combination of modeling and experimentation.

2. LITERATURE REVIEW

2.1. THERMODYNAMICS

2.1.1. ε-martensite, Stage I (γ→ε). Determination of an athermal start temperature of the ε-martensite (Ms^{ε}) has been reported recently by Yang et. al [16] using a neural network on 328 alloys with measured Ms^{ε} values. This formulation, given in eq. (1), however does not explicitly account for thermodynamic solute interactions.

$$M_S^{\varepsilon} = 576 - 489x_C - 9.1x_{Mn} - 17.6x_{Ni} - 9.2x_{Cr} + 21.3x_{Al} + 4.1x_{Si} - 19.4x_{Mo} - 1x_{Co} - 41.2x_{Cu} - 50x_{Nb} - 86x_{Ti} - 34x_V - 13x_W \tag{1}$$

Olson and Cohen [18, 19] presented a thermodynamic formulation for the SFE and is defined according to eq. (2). The temperature at which the SFE = 0 can be considered as a proxy for predicting the martensite start temperature (Ms). At a SFE = 0 a dislocation in γ-austenite can separate into partials forming a stacking fault ribbon.

$$SFE\left(\frac{mJ}{m^2}\right) = n\rho\left(\Delta G_{Chem}^{i\to j} + \Delta G_{Str}^{i\to j}\right) + 2\sigma^{i/j} \tag{2}$$

where n is the critical nucleus size, ρ, is the atomic density for the close packed planes of the $\{111\}_{\gamma}$, $\Delta G_{Chem}^{i\to j}$, is the chemical driving force from parent to product phase, $\Delta G_{Str}^{i\to j}$, is the strain energy associated with the transformation, and $\sigma^{i/j}$ is the interfacial energy between the parent and product phase, and according to the work by Pisarik and Van

Aken a value of 10 mJ/m^2 is best suited for the systems of interest [17]. In the ε-martensite formulation the $\Delta G_{Str}^{i\rightarrow j}$ is typically neglected since as reported by Olson and Cohen the strain energy contributed less than 0.1% to the measured fault energy [18]. Pisarik and Van Aken [17] showed that for the γ→ε martensitic transformation a value of n = 4 best fit the experimental results reported for the 328 alloy that Yang et al. reported for the Ms^{ε} temperature. Interestingly the value of n = 4 is exactly what was predicted in the seminal work by Olson and Cohen [18] for the critical size of an ε-martensite nucleus. Pisarik and Van Aken also reported that Mn has a complex relationship to the ε-martensite start temperature and was shown to be a local maximum of the Ms^{ε}, and this effect is shown in Figure 2.1.

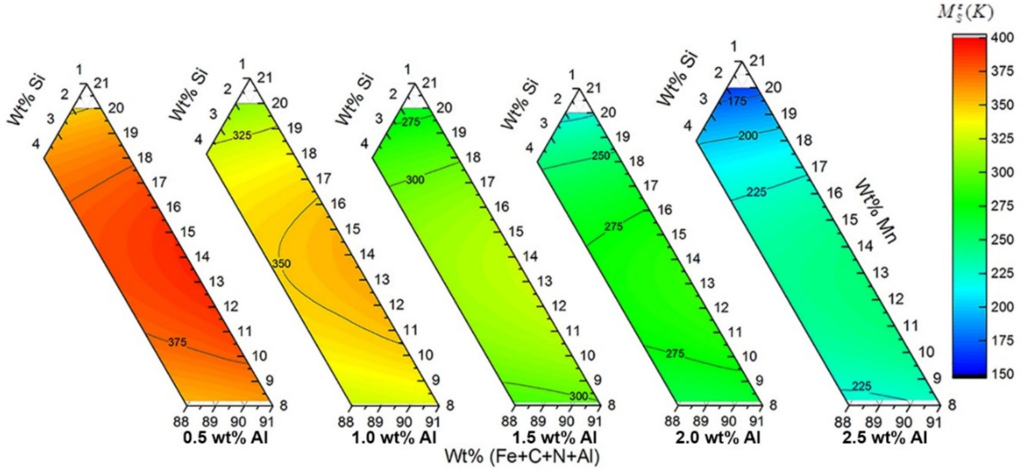

Figure 2.1. Contour map of the effect of Si, Mn, and Al on the calculated Ms^{ε} with C and N fixed at 0.07 and 0.017 wt. pct. respectively.

2.1.2. α-martensite, (γ→α). Understanding the γ-austenite stability relative to α-martensite is equally important to γ-austenite's stability relative to the ε-martensite in order to design future advanced high strength steels (AHSS). Prediction of the Ms for Mn steels containing 10-15 wt. pct presents significant difficulty. Holden et al. [20] showed that for a composition of 8 – 12 wt. pct. manganese both α martensite and ε-martensite are observed. Acet et al. [21] observed that for steels containing 10 – 15 at. pct. α-martensite and ε-martensite are within the microstructure and this can be observed in Figures 2.2(a) and 2.2(b). Holden et al. [20], shows in Figure 2.2(a) the phase transformations for medium-Mn steels with C contents ranging from 0.01 to 0.04 wt. pct. and Si ranging from 0.03 to 0.34 wt. pct. Holden et al. in his figure noted that below 12 wt. pct. Mn the α-martensite was the dominant microstructural component upon cooling, a mixture of ε, and α martensite occurred between 12 and 15 wt. pct. Mn. Acet et al. [21], shows in Figure 2.2(b) that both the γ→α, and γ→ε martensitic reactions occur between 10 to 15 at. pct. (equivalent to wt. pct.). The final microstructure upon cooling would be expected to vary depending upon which martensite formed first; it is therefore required that accurate predictions of the Ms temperatures be determined.

Aluminum has been an important alloying component of TRIP steels despite the lack of fully understanding the chemical dependence on the Ms temperature upon aluminum. Al is reported to increase the Ms temperature for α-martensite. In this regard two empirical models are reported by De Cooman and Speer that contain aluminum [22] it is noted that the magnitude of the effect aluminum has on the Ms temperature varies significantly between these two formulations for the Ms^{α} depending upon the alloying elements considered in the empirical relationship.

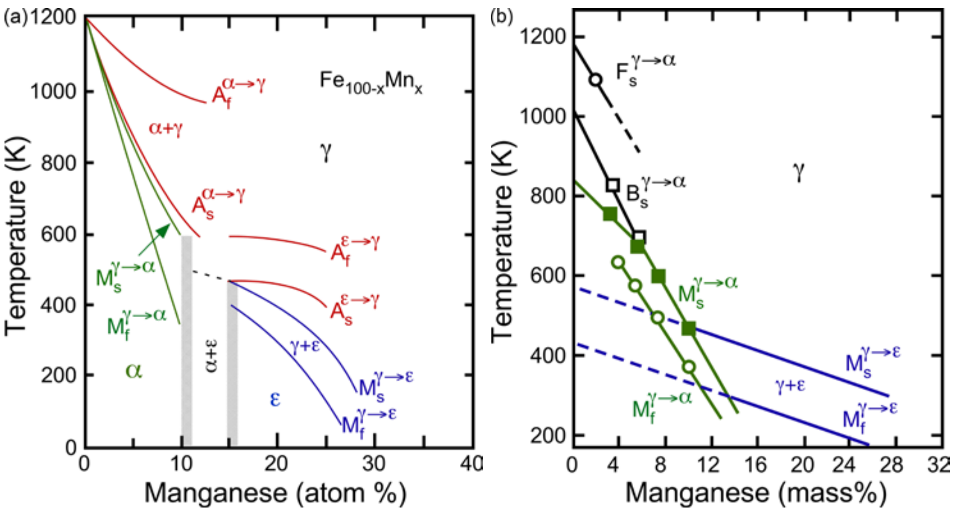

Figure 2.2. Phase transitions for Fe-Mn alloys reported from (a) Holden et al. [20] and (b) Acet et al. [21].

$$Ms(K)= 812-423[wt.\%C]-30.4[wt.\%Mn]-7.5[wt.\%Si]+30[wt.\%Al] \qquad (3)$$

$$Ms(K)= 812-308[wt.\%C]-30.4[wt.\%Mn]-59.9[wt.\%P]-16.6[wt.\%Si]+43.6[wt.\%Al] \qquad (4)$$

Olson and Cohen [19] theorized that the SFE formulation from eq. (2) could be adapted also to determine the Ms for α-martensite formulation. In the α-martensite formulation for the SFE equation the $\Delta G_{Str}^{\gamma\to\alpha}$ is considered of greater importance due to the increased volume strains associated with the γ→α transformation. Olson and Cohen calculated the average critical embryo size as having an n = 13.5 for spontaneous α-martensite formation of an Fe-30Ni alloy (in wt. pct.) at the condition where SFE = 0, and this value is significantly larger than the value reported for the ε-martensite formulation (n = 4). The interfacial energy is reported to be 0.2 mJ/m^2 [19], it can be shown from the large defect size and low interfacial energy that the controlling terms for the α-martensite formulation is the balance of the $\Delta G_{Chem}^{i \to j}$ that drives the reaction to initiation and the $\Delta G_{Str}^{i \to j}$ that resists the reaction.

There have been many thermodynamic works [23-21] to relate $\Delta G_{Str}^{\gamma \to \alpha}$ to the M_S^{α} Raghavan and Anita [24] investigated this relationship for 1152 low alloy steels. A linear relationship between the calculated value for the M_S^{α} (using the formulation based upon the work of Andrews [25]) and the $\Delta G_{Str}^{\gamma \to \alpha}$ was obtained resulting in $\Delta G_{Str}^{\gamma \to \alpha} \left({}^{J}\!/_{mol} \right) = -1.49 M_S + 2065$. Jicheng and Zhanpeng [23] also investigated the thermodynamic relationship between the measured M_S^{α} and $\Delta G_{Str}^{\gamma \to \alpha}$ for binary Fe-C, Fe-Ni, Fe-Cr, and Fe-Cu alloys and found two different relationships that where related to the martensite morphology, i.e. lath or plate. Jicheng and Zhanpeng reported linear relationships for lath martensites, $\Delta G_{Str}^{\gamma \to \alpha} \left({}^{J}\!/_{mol} \right) = -1.23 M_S + 2323$ for Fe-C and $\Delta G_{Str}^{\gamma \to \alpha} \left({}^{J}\!/_{mol} \right) = -2.3 M_S + 3162$ for Fe-Cr are similar to what Raghavan and Anita reported [24]. For plate martensite in the Fe-Cr and Fe-Cu systems, Jicheng and Zhanpeng observed that the $\Delta G_{Str}^{\gamma \to \alpha}$ was significantly different, $\Delta G_{Str}^{\gamma \to \alpha} \left({}^{J}\!/_{mol} \right) = -11.4 M_S + 5780$ [23]. As such a thermodynamic model to determine the M_S^{α} temperature is required to direct the design of future two-stage TRIP steels.

2.2. STRAIN AGING

2.2.1. Static Strain Aging.

Yield point elongation (YPE), associated with with static strain aging is of significant concern to the automotive industry. Steels exhibiting YPE are not desired due to difficulties in forming the complex parts to be utilized in automotive components [26]. Static strain aging is defined as an increase in yield and ultimate strengths, a decrease in the total elongation, and a time dependent return of the YPE or Lüders strain after plastic deformation [27,28]. YPE leads to inhomogeneous deformation and causes inconsistencies in the thickness of formed parts. The developed thickness variation is of significant concern to the press forming operation. Medium-Mn steels developed for automotive application [29-37] exhibit the yield point elongation behavior. The degree of YPE can range significantly (2-10 pct.) depending upon both the composition and processing of the steel prior to testing.

Suh et al. [30] investigated three Fe-0.5Si-5Mn-2Al (wt. pct.) alloys and varying carbon contents (0.06 - 0.11 wt. pct.). Suh et al. observed that the extent of the YPE varied based on heat treatment temperature. An increase in heat treatment temperature from 933K (720 °C) to 1033 K (760 °C) lead to a direct reduction in YPE from 10 pct. to 4 pct. strain independent of carbon content. The significant change in the YPE, was not noted by Suh et al., but can be attributed to the volume faction of α-ferrite/martensite in the starting structure. Alloys exhibiting the greater yield point elongations had more α-ferrite (87 vol. pct.) in the starting structure compared to the specimens that exhibited 4 pct. YPE specimens (72 vol. pct.). A medium-Mn steel reported by Han et al. [35] with 8.5 wt. pct. Mn showed an extensive yield point elongation (~11 pct.) after cold working and intercritical annealing at 893K (620 °C), this steel contained 63 vol. pct. α-ferrite/martensite in the starting structure.

2.2.2. Dynamic Strain Aging. Dynamic strain aging (DSA) typically produces an increase in the work hardening rate, a negative strain rate response, and a serrated stress strain curve. Horvath et al. [18] stated that the negative strain rate dependence on ultimate tensile strength associated with DSA of the medium-Mn steels, is a concern for the crash worthiness of potential future 3rd generation advanced high strength steels. DSA is caused by the dynamic interaction of dislocations and point defects, like interstitials. During DSA dislocations are pinned by interstitials during plastic deformation reducing the mobile dislocation density this results in an increase in flow stress as fewer dislocations must move faster to accommodate the imposed strain rate. Dislocation multiplication or subsequent unpinning at the higher stress will produce a transient drop in the flow stress, since more dislocations are mobile and move at a slower velocity. Rodriguez identified five unique forms of serrated flow observed in steel and are schematically shown in Figure 2.3 [38]. The types of DSA are defined as follows: Type A serrations occur when deformation bands initiate at the same end of the specimen and propagate in the same direction. Type B occurs due to discontinuous band propagation. Type C are yield drops due to dislocation unlocking and typically occurs at higher temperature. Type D are described as Lüders bands with no work hardening. Type E are Type A serrations at higher strains.

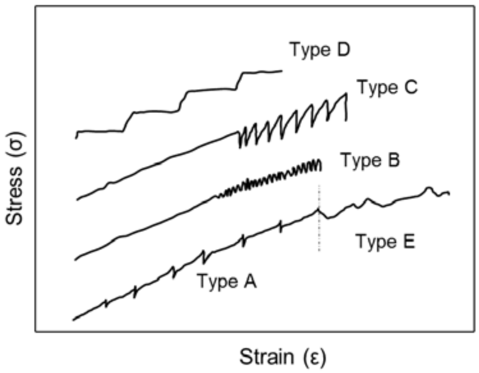

Figure 2.3. Schematic diagram of the five unique types of serrated flow reported in literature.

The most comprehensive work performed on DSA in medium manganese steel has been on Hadfield's manganese steel [39] and steels that exhibit twining induced plasticity (TWIP) [40]. Investigation on the work hardening mechanism for the Hadfield's steel by Dastur and Leslie was performed on a 0.2Si-11.4Mn-0.17Ni-0.16Cr-0.08Mo-1.13C-balFe (in wt. pct) steel. They argued that the work hardening behavior of Hadfield steels was related to the observed dynamic strain aging associated with carbon diffusion and locking of dislocations rather than interaction with twin formation. The activation energy for the onset and termination of DSA was measured to be 104 kJ/mol and 146 kJ/mol [39]. It was also observed that the onset of DSA activation energy was below the activation energy for C diffusion in γ-austenite (~134 kJ/mol [39]).

Work on TWIP steels by Lee et al. investigated the two manganese steels, one containing aluminum, 18Mn-1.5Al-0.6C-BalFe, and the second being an Al-free 18Mn-0.6C-balFe steel. An activation energy for the onset of DSA was determined by internal friction and a value of 100 kJ/mol was reported. From Mössbauer spectroscopy analysis they proposed that the diffusion of carbon, or a point defect complex, to the stacking fault region caused the observed DSA [40].

Many of the medium-Mn steels proposed for future 3rd generation advanced high strength steel implementation exhibit DSA [25, 31, 33, 36, 41, 42]. Gibbs et al. [36] investigated a 7Mn steel annealed at temperatures varying from 848 to 948K (575 to 675 °C) for 7 days. DSA and YPE was observed in the 898K and 873K (625 °C and 600 °C) conditions with ≥ 67 vol. pct. α-ferrite/martensite in the starting structure. Nitrogen has also been reported to cause DSA [38] in steels and many of the developed medium-Mn TRIP alloys contain significant levels (>100 ppm) of nitrogen [33, 36]. Zhang et al. [33]

reports a medium-Mn steel with 120 ppm nitrogen that exhibited significant DSA at room temperature after varying degrees of intercritical warm working (0 – 77.5 pct. reduction in thickness) at 923K (650 °C). All of the specimens reported by Zhang et al. exhibit significant Type A and B serrations. Shi et al. [41] studied four medium Mn alloys annealed at 923K (650 °C), and these steels all exhibit significant Type B serrations in the stress-strain data. Luo et al. [31] reports two manganese steels after varying heat treatment temperatures. From the stress-strain graphs shown by Luo et al. DSA was observed in the alloys heat treated to 943K (670 °C) and these steels contained roughly 88 vol. pct. α-ferrite. However, alloys heat treated at 923K (650 °C) do not exhibit any serrations and it was noted by TEM analysis that cementite was precipitated in these specimens.

2.3. MECHANICAL BEHAVIOR

2.3.1. Deformation Response. Medium manganese (5 – 12 wt. pct.) steels can exhibit three deformation responses: the conventional TRIP (γ→α), TWIP – TRIP behavior, or two-stage TRIP (γ→ε→α) character. Medium manganese in the range of 5 to 12 wt.% Mn steels are used in conjunction with intercritical partitioning treatments. The γ→α TRIP behavior is more complicated in these medium Mn steels by the potential for twin induced plasticity (TWIP) prior to TRIP, and two-stage TRIP where γ-austenite first transforms to ε-martensite and subsequently transforms to α-martensite. Mechanical twins and ε-martensite are both formed by the motion of partial dislocations in the γ-austenite. The distinction between the two is often generalized by calculation of the intrinsic stacking fault energy (ISFE) [43-45]. Typically twins are formed when the partials occur on every close packed $\{111\}_\gamma$, ε-martensite however, is observed when partial dislocations are placed on every other $\{111\}_\gamma$. There have been many works on the ISFE range at which the formation of ε-martensite will transition to mechanical twinning. For intrinsic stacking fault energies ≥ 20 mJ/m^2 alloys will mechanically twin and no ε-martensite is observed. The works by Remy and Pineu [43], Allain et al. [44] and Lee et al. [45] showed that in the range of 12 – 17 mJ/m^2, using the model developed by Pisarik and Van Aken [17], both twins and ε-martensite are observed simultaneously. These investigations also observed that for alloys formulated with calculated ISFE ≤ 12 mJ/m^2 the γ-austenite will transform to ε-martensite without twin formation. Grässel et al. [46] investigated high manganese (> 15 wt. pct) TWIP – TRIP steels with varying levels of silicon and aluminum. It was concluded that when the γ→α TRIP effect was activated the tensile strength increased significantly (180 MPa). The cause for this increase in strength was theorized to be due to delaying necking of the steel. A lightweight duplex steel investigated by Song et al. [47] et al. with composition of 0.32C – 5.8Mn – 5Al (in wt. pct.) was processed by cold rolling followed by intercritical annealing and produced a fine grained γ-austenite and α-ferrite structure between the elongated δ-ferrite grains. The unstrained γ-austenite contained annealing twins, but when plastically strained deformation bands formed with α-martensite forming by TRIP within the deformation bands producing a combined TWIP – TRIP behavior. Lee et al. [48], showed that for a TWIP – TRIP steel the α-martensite that formed during tensile loading occurred at the intersection of the twin bands. In the work by Lee et al. [49] a set of constitutive models were developed using nano-indention to determine the strength of the γ-austenite and the annealed α-ferrite. A Hall-Petch relationship for the yield strength was derived by Lee et al. and is shown in eq (5)

$$\sigma_{yield}\left(MPa\right)=\frac{332\left(MPa\sqrt{\mu m}\right)}{\sqrt{D\left(\mu m\right)}}+223\left(MPa\right) \tag{5}$$

A two-stage TRIP behavior [4-6, 42, 50] is observed in medium-manganese steels (7-15 wt. pct. Mn) when carbon is held below 0.2 wt. pct. Alloying or partitioning of the γ-austenite is formulated to produce an ISFE ≤ 10 mJ/m^2. The strain induced martensitic transformation products have been quantitatively followed using interrupted tensile testing and x-ray diffraction to characterize microstructural evolution during tensile straining [4, 50]. For total strains less than 4% (strains up to 10% if yield point elongation is observed) the γ-austenite first transforms to ε-martensite and segments the γ-austenite into smaller volumes. Pisarik and Van Aken [12] showed using electron backscattered diffraction (EBSD) that the two-stage athermal transformation behavior (γ→ε→α) has an intrinsic grain refinement that is three times greater than the conventional athermal transformation to α-martensite. In addition to this grain refinement aspect the formation of ε-martensite directly lowers the chemical driving force to form α-martensite.

The hcp ε-martensite is a denser close packed structure than γ-austenite. Work on the ferrous shape memory alloys have reported that there is a significant volume expansion when ε-martensite transforms to α-martensite (2.2%) during Stage II TRIP. [52] The microstructural refinement and significant volume expansion associated with the Stage II TRIP response is thought to be responsible for the high work hardening rates, high tensile strengths (>1200 MPa) and elongations to failure in excess of 25 pct [4, 5, 6, 50]. De Cooman et al. [53] reports on a 7Mn steel annealed at 873K and 923K (600 °C and 650 °C) with a dual-phase $\alpha + \gamma$ ultrafine grain structure. After annealing the γ-austenite is reported to have a stacking fault energy of -5 mJ/m^2 and -14 mJ/m^2. The γ-austenite is shown through TEM analysis to contain both ε-martensite and α-martensite and they state that the α-martensite observed is always nucleated within the ε-martensite.

Shape memory Fe-Mn alloys also show a sequential martensitic transformation if strained beyond the elastic limit to produce unrecoverable strain. Both Huang et al. [15] and Shin et al. [14] independently have shown that for strains greater than 4 pct. the recovery response in the shape memory system is significantly deteriorated. At the 4 pct. strain the formation of α-martensite within intersecting ε-martensite bands was observed using transmission electron microscopy. Recent work with the medium-Mn two-stage TRIP steels by Field and Van Aken [50] showed that the Stage II ($\varepsilon \rightarrow \alpha$) martensitic reaction occurred at 4-6 pct. strains. Their results and this is in close agreement with the works on shape memory alloys. Both shape memory alloys [14, 15] and the earlier work of McGrath et al. [5] show that the transformation to ε-martensite occurs at stresses below 300MPa when the austenite grain size is 30 to 100μm. Recent developments with cold working followed by annealing of the two-stage TRIP steels at 873K (600 °C) to produce nanocrystalline grain structures have shown promise in increasing the yield-strength up to 830 MPa [42, 50].

2.3.2. Effect of Chemistry. Automotive steel is typically produced as a hot band product with a gauge thickness between 1.8 and 3.3 mm [54] and recrystallization behavior of the hot band steel is of significant concern for subsequent cold rolling. It has been reported in literature that substitutional alloying elements like silicon and aluminum will influence the recrystallization rate of conventional TRIP steels [55-57]. Suikkanen et al. [55] showed that the kinetics for static recrystallization decreased linearly with increasing Si contents up to a concentration of 1.5 wt. pct Si. Zhu et al. [57] also found that the dynamic recrystallization response is greatly impeded when the silicon content is increased to 1.5 wt. pct. Si. The effect of silicon has also been reported in the work by Somani et al. [58], Medina and Mancilla [59], and Medina and Quispe [60] to slow recrystallization kinetics of steel. Silicon's effect on recrystallization has been rationalized through its solute drag effect on grain boundaries [57-60]. Mn was shown to have little effect on the dynamic and static recrystallization as shown by Li-Juan et al. [56]; however, Li-Juan et al. did observe that silicon was effective in slowing the dynamic recrystallization as well as increased the recrystallization temperature.

Aluminum's complicated effect on TRIP steel microstructures is not confined to only the Ms^{α} but the recrystallization kinetics as well. Somani et al. [55] found that Al had a negligible effect on the static recrystallization. The effects of substitutional alloying elements of silicon and aluminum on recrystallization are of great concern for potential two-stage TRIP steels because they both have been shown to reduce the unstable stacking fault energy [61], which is considered the barrier to ε-martensite formation, making them favorable alloying elements to obtain the two-stage TRIP response.

PAPER

I. ON THE PREDICTION OF α-MARTENSITE TEMPERATURE IN MEDIUM MANGANESE STEELS

Daniel M. Field[a], Daniel S. Baker[b] and D.C. Van Aken[c]

[a] Missouri University of Science and Technology
Department of Materials Science and Engineering, Rolla, MO 65409
Phone: 573-341-4804
e-mail: dfb52@mst.edu

[b] General Motors Global Propulsions Systems, Pontiac Materials Lab
Pontiac, MI 48340
Phone: 248-563-5723
e-mail: dan.baker@gm.com

[c] Missouri University of Science and Technology
Department of Materials Science and Engineering, Rolla, MO 65409
Phone: 573-341-4717
e-mail: dcva@mst.edu

Published in Metallurgical and Materials Transactions A, May 2017 pp.2150-2163

ABSTRACT

A new composition based method for calculating the α-martensite start temperature in medium manganese steel is presented and uses a regular solution model to accurately calculate the chemical driving force for α-martensite formation, $\Delta G_{Chem}^{\gamma\to\alpha}$. In addition, a compositional relationship for the strain energy contribution during martensitic transformation was developed using measured Young’s moduli (E) reported in literature and measured values for steels produced during this investigation. An empirical relationship was developed to calculate Young’s modulus using alloy composition and was used where dilatometry literature did not report Young’s moduli. A comparison of the $\Delta G_{Chem}^{\gamma\to\alpha}$ normalized by dividing by the product of Young’s modulus, unconstrained lattice misfit squared (δ^2), and molar volume (Ω) with respect to the measured α-martensite start temperatures, M_S^α, produced a single linear relationship for 42 alloys exhibiting either lath or plate martensite. A temperature dependent strain energy term was then formulated as $\Delta G_{str}^{\gamma\to\alpha}\left({}^{J}\!/\!_{mol}\right)-E\Omega\delta^2\left(14.8-0.013T\right)$, which opposed the chemical driving force for α-martensite formation. M_S^α was determined at a temperature where $\Delta G_{Chem}^{\gamma\to\alpha}+\Delta G_{Str}^{\gamma\to\alpha}=0$. The proposed M_S^α model shows an extended temperature range of prediction from 170K to 820K (-103 °C to 547 °C). The model is then shown to corroborate alloy chemistries that exhibit two-stage athermal martensitic transformations and two-stage TRIP behavior in three previously reported medium manganese steels. In addition, the model can be used to predict the retained γ-austenite in twelve alloys, containing ε-martensite, using the difference between the calculated M_S^ε and M_S^α

I. INTRODUCTION

Accurate calculation of martensitic start temperatures (Ms) for steel has been an elusive and important goal in the effort to design new advanced high strength steels (AHSS) that utilize transformation induced plasticity (TRIP) behavior to increase ductility and improve crashworthiness of automotive sheet steel. Quench and partitioned steels have shown ultimate tensile strengths in excess of 1500 MPa with elongation to failure of 20% [1] whereas two-stage TRIP steels have shown strengths in excess of 1200 MPa and elongation to failure greater than 30%. [2-4] Thus, the ability to correctly predict the Ms temperature is important when quench and partitioning is used to develop retained γ-austenite in these new AHSS [1,5-7]. Likewise, AHSS developed to show two-stage TRIP behavior [2-4, 8, 9] where γ- austenite first transforms to ε-martensite and then to α-martensite ($\gamma \rightarrow \varepsilon \rightarrow \alpha$) also require better models to formulate compositions that obtain the highest level of transformable microstructure, i.e. γ-austenite or ε-martensite. This difficulty is highlighted by the work of Acet et al. [10] and Holden et al. [11] for medium manganese steels in the range of 10 to 15 at pct. manganese. Figure 1(a) shows that in this compositional range both α-martensite and ε-martensite are observed, and according to Figure 1(b) a mixed α and ε martensitic structure would occur in the range of 8-12 wt. pct. manganese. Microstructural evolution during γ-austenite transformation is expected to vary depending upon which martensite forms first; thus, accurate prediction of these temperatures is very important.

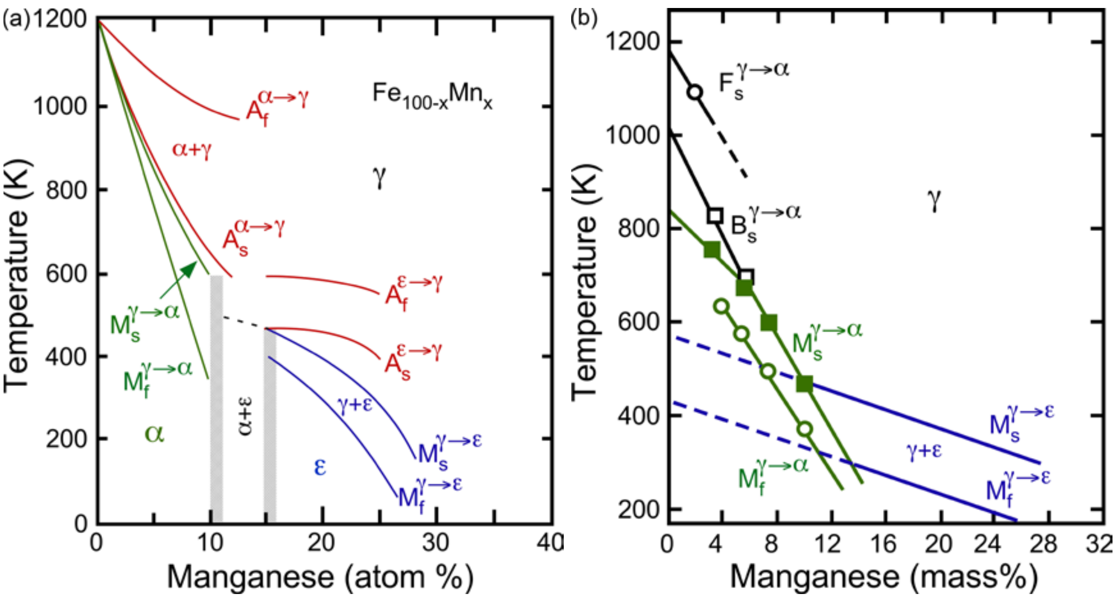

Fig. 1. (a) Phase transitions for binary Fe-Mn alloys as reported in reference [10]. Two martensitic reactions are shown in the range of 10 to 15 at. pct. Mn. Adapted from Fig. 4 from reference [10]. (b) Phase transitions reported by Holden et al. [11] for medium Fe-Mn alloys with C ranging from 0.01 to 0.038wt. pct. and Si ranging from 0.03 to 0.34wt. pct. Below 12wt. pct. Mn, α-martensite was the dominant transformation product and a mixture of ε and α martensite occurred between 12 and 15 wt. pct. Mn. Schematic drawing is based upon Fig. 1 from reference [11].

Manganese, silicon and aluminum have been important alloying components of TRIP steel despite the lack of fully understanding the compositional dependence on the Ms temperature. For ε-martensite, the start temperature is expected to correlate with the intrinsic stacking fault energy, and manganese shows a parabolic relationship with a minimum predicted in the range of the medium manganese steels.[12] Manganese is also known for lowering the elastic moduli of steel [13] and this may affect the strain energy of formation of alpha α-martensite. Most empirical models for the α-martensite start temperature are derived for low alloy steels containing solute contents less than 5 wt. pct. In this regard, two empirical models are reported by DeCooman and Speer [14] which contain aluminum (eq. (1) and (2)), and a third model is provided for non-aluminum containing steels (eq. (3)) that will be used in this study for steels containing Ni and Cr. As these empirical models show for low alloy steels, only cobalt and aluminum additions increase the α-martensite start temperature

$$Ms(K)= 812-423[wt.\%C]-30.4[wt.\%Mn]-7.5[wt.\%Si]+30[wt.\%Al] \quad (1)$$

$$Ms(K)= 812-308[wt.\%C]-30.4[wt.\%Mn]-59.9[wt.\%P]-16.6[wt.\%Si]+43.6[wt.\%Al] \quad (2)$$

$$Ms(K)= 772-308[wt.\%C]-32.4[wt.\%Mn]-27[wt.\%Cr]-16.2[wt.\%Ni]-10.8[Si+Mo+W]+10[wt.\%Co] \quad (3)$$

Literature reports multiple attempts to correlate the Ms to thermodynamic driving forces [15-19]. Pisarik and Van Aken [18] have used a modified regular solution model and the Olson and Cohen [21,22] formulation for stacking fault energy to predict the Ms temperature for ε-martensite. Olson and Cohen presented a general formulation for the stacking fault energy according to Eq. (4).

$$SFE\left(\frac{mJ}{m^2}\right) = n\rho\left(\Delta G_{Chem}^{i\rightarrow j} + \Delta G_{Str}^{i\rightarrow j}\right) + 2\sigma^{i/j} \quad (4)$$

where n is the number of atomic planes in the fault within the parent γ-austenite, ρ is the planar atomic density of the $\{111\}_\gamma$ for the steel composition using Vegard's law, and $\sigma^{i/j}$ is the interfacial energy between the parent and product phases. Literature pertaining to the development of 2nd generation AHSS report an intrinsic stacking fault energy at room temperature using Eq. (4) with n=2 [20, 22]. In the transformation of γ-austenite to ε-martensite, Pisarik and Van Aken [20] determined an ε-martensite start temperature when the stacking fault energy becomes less than or equal to zero and spontaneous separation of the 1/6<112> partials occur to expand the stacking faults. A value of n was found by calculating the chemical driving force using the regular solution model and finding the temperature where the chemical driving force produced a SFE equal to zero. In this formulation, the strain energy of the transformation $\left(\Delta G_{str}^{\gamma\rightarrow\varepsilon}\right)$ was neglected, since as reported by Olson and Cohen, $\Delta G_{str}^{\gamma\rightarrow\varepsilon}$ is less than 0.1 percent of the measured fault energy [22]. It is interesting to point out that a value of n=4 was found by Pisarik and Van Aken [20] to best fit the experimental results of annealed medium manganese steel, in agreement with the prediction from the seminal work by Olson and Cohen [22] for the critical size of ε-martensite nucleus. Also of interest was that Pisarik and Van Aken reported that manganese had a complex relationship to the ε-martensite start temperature with a maximum temperature near 12 wt. pct. manganese, which is supported by the first principles work of Medvedeva et al. showing a minimum in the intrinsic stacking fault energy in the same chemical range. [12]

In the following discussion the α designation is ascribed to the martensitic phase and is assumed to be cubic, and thus, the thermodynamic relations for body centered cubic iron are substituted for α-martensite. For the γ-austenite to α-martensite transformation the interfacial energy, $\sigma^{\gamma/\alpha}$, is reported to be less than 0.2 mJ/m^2 [22]. In contrast to the γ→ε martensitic reaction, the $\Delta G_{str}^{\gamma\rightarrow\alpha}$ is considered to be of greater importance due to the increased volume strains associated with the γ→α transformation. Olson and Cohen [21] calculated the average critical embryo size as having an n=13.5 for the spontaneous α-martensite formation of an Fe-30Ni alloy, which was again the condition where according to equation (4) the SFE of the martensite embryo goes to zero.

Grujicic et al. [23] calculated the interface mobility of the α-martensite utilizing dislocation dynamics and utilized an embryo size of n=18. Due to the low interfacial energy and the large defect size, the controlling terms of the SFE equation for the fcc to bcc transformation are the chemical driving force for transformation, $\Delta G_{Chem}^{\gamma\rightarrow\alpha}$, and the strain energy, which resists transformation, $\Delta G_{str}^{\gamma\rightarrow\alpha}$. In this presentation the calculated $\Delta G_{Chem}^{\gamma\rightarrow\alpha}$ determined at the M_S^{α} temperature will be designated as $\Delta G_M^{\gamma\rightarrow\alpha}$ and represents the energy required to promote the martensitic reaction. The temperature at which $\Delta G_{Chem}^{\gamma\rightarrow\alpha} = 0$ is designated as T_0, as proposed by Kaufman and Cohen [24]. Thus, at the M_S^{α} temperature, it is assumed $\Delta G_M^{\gamma\rightarrow\alpha}$ is the required energy to overcome the strain of transformation, $\Delta G_{str}^{\gamma\rightarrow\alpha}$.

There have been many thermodynamic works [15-19] to relate $\Delta G_M^{\gamma\rightarrow\alpha}$ to the M_S^{α}. Raghavan and Anita [16] investigated this relationship for 1152 low alloy steels. A linear relationship between the calculated value for the M_S^{α} (using the formulation based upon the work of Andrews [17]) and the $\Delta G_M^{\gamma\rightarrow\alpha}$ was obtained resulting in $\Delta G_M^{\gamma\rightarrow\alpha}\left({}^{J}\!/_{mol}\right) = 1.49M_S - 2065$. Jicheng and Zhanpeng [15] also investigated the thermodynamic relationship between the measured M_S^{α} and $\Delta G_M^{\gamma\rightarrow\alpha}$ for binary Fe-C, Fe-Ni, Fe-Cr, and Fe-Cu alloys and found two different relationships that where related to martensite morphology, i.e. lath vs. plate. For lath martensite, Jicheng and Zhanpeng reported a linear relationship, similar to what Raghavan and Anita reported, for the Fe-C and Fe-Cr systems $\Delta G_M^{\gamma\rightarrow\alpha}\left({}^{J}\!/_{mol}\right) = 1.23M_S - 2323$ and $\Delta G_M^{\gamma\rightarrow\alpha}\left({}^{J}\!/_{mol}\right) = 2.3M_S - 3162$, respectively. For twinned martensite in the Fe-Cr and Fe-Cu systems, Jicheng and

Zhanpeng observed that the $\Delta G_M^{\gamma\to\alpha}$ had a much stronger dependence upon the martensite start temperature, $\Delta G_M^{\gamma\to\alpha}\left({}^{J}\!/\!_{mol}\right)=11.4M_S-5780$ [15]. These formulations for the $\Delta G_M^{\gamma\to\alpha}$ can be considered as temperature dependent formulations for $\Delta G_{Chem}^{\gamma\to\alpha}=0$. In systems that produce an internally twinned or plate martensite, the strain energy exhibits a greater dependence upon temperature. It is often observed that the habit planes of plate martensites are of a type {225} [25, 26] and that these plates are internally twinned versus lath martensites where the variants are twin related and have habit planes {557} [26]. Lath martensites form in packets and give the appearance of four different {111} variants due to there only being 16° of separation between {557} and {111}. In contrast, the plate morphology appears more random as individual habit plane variants appear. Therefore, it might be argued that the plate morphology segments the γ-austenite with more crystallographic variants and is internally twinned to accommodate greater strain energy at the lower transformation temperatures observed.

A. Regular Solution Model of γ→α Martensitic Transformation

The purpose of this work was to create a thermodynamic means for formulating M_S^{α} based upon $\Delta G_{Chem}^{\gamma\to\alpha}$ using a regular solution model and the work by Breedis and Kaufman is used here [26]. This approach has been utilized by numerous authors [20, 27-30] for medium manganese steels and is formulated according to eq. (5)

$$\Delta G_{Chem}^{\gamma\to\alpha}(J/mol)=X_{Fe}\Delta G_{Fe}^{\gamma\to\alpha}+\Sigma X_i\Delta G_i^{\gamma\to\alpha}+\Sigma X_{Fe}X_i\Delta\Omega_{Fe(i)}^{\gamma\to\alpha} \quad (5)$$

where X_i is the atomic fraction of the solute element i. The summation accounts for all alloying elements in the system, which for this investigation are C, Mn, Si, Al, Cr, and

Ni. The various alloying elements alter the free energy change for the γ→α transformation by an amount expressed as $\Delta G_i^{\gamma\rightarrow\alpha}$. The interaction parameter in the iron based system for solid solution expressed by $\Delta\Omega_{Fe(i)}^{\gamma\rightarrow\alpha}$. Both $\Delta G_i^{\gamma\rightarrow\alpha}$ and $\Delta\Omega_{Fe(i)}^{\gamma\rightarrow\alpha}$ were obtained from the CALPHAD reviews by Kaufman [31-34]. The Scientific Group Thermodata Europe (SGTE) [35] data was also reviewed and found to be the most relevant to the systems being investigated in this work. Appendix A summarizes the literature data used for both the $\Delta G_i^{\gamma\rightarrow\alpha}$, and $\Delta\Omega_{Fe(i)}^{\gamma\rightarrow\alpha}$. Nitrogen is not accounted for in the proposed model since there is no accepted interaction parameter reported in literature and represents a potential shortcoming of the model being proposed.

B. Experimental Procedure

In addition to alloys selected from the literature, nine medium manganese steels were produced by induction melting of induction iron, ferrosilicon, electrolytic manganese, pure aluminum, and carbon in the form of graphite. An argon cover gas was used to shield the melt. Calcium wire additions were made to modify oxide inclusions and remove sulfur. The molten steel was tapped from the furnace into a ladle modified with a ceramic dam to force liquid from below the surface to form the pouring stream in a manner similar to a teapot. Steels were cast with a 150K (150 C°) superheat into phenolic urethane no-bake sand molds to form a Y-block with dimensions measuring 12.6 x 6 x 1.7 cm^3. A Foseco KALPUR® insulated riser with a diameter of 13.5 cm and height of 15.3 cm was utilized to ensure the soundness of the Y-block castings. The castings were normalized by heating to 1373K (1100 °C), holding at temperature for 2 hours, and air cooled to room temperature, nominally 298K (25 °C). Castings were milled to an orthogonal prism of dimensions 15.5 x 125 x 50 mm^3 and hot rolled by sequentially heating to 1223K (950°C), rolling, and reheating to 1223K (950 °C). The repeated process of rolling and reheating was used to obtain the desired hot band gauge of 2.5 mm and represents a total hot reduction of 87.2 ± 6.8 pct. After the final roll pass the strip was reheated to 1223K (950 °C) for 5 minutes before being water quenched to 298K (25 °C). Reheating was performed to obtain a recrystallized and low defect crystal structure prior to water quenching. Alloys designated as 7Mn1Ni, 7Mn2Ni, and 7Mn3Cr were produced at US Steel Research by vacuum induction melting and ingot casting. The 75-mm-thick ingots were reheated to 1533K (1260 °C), rough hot rolled to 25-mm thickness, and air cooled to room temperature. After sectioning, the materials were reheated to 1533K (1260 °C) and finish hot rolled to 4.6-mm thickness with simulated finishing and coiling temperatures of 1198K (925 °C) and 873K (600 °C), respectively. The reported chemical analysis was obtained by ion coupled plasma spectrometry after sample dissolution in hydrochloric and nitric acid. Carbon and Nitrogen contents were determined using a LECO CS6000 and a LECO TC500, respectively (Table I).

Samples for dilatometry were cut from the hot band strip with dimensions of 2.20 x 2.45 x 9.71 mm^3 with the long axis parallel to the rolling direction. Dilatometry was performed using a Lenseis L78 RITA Quenching Dilatometer at AK Steel Dearborn Works. Samples were heated to 1273 K (1000°C) at a heating rate of 10K/sec and then cooled to room temperature at varying rates of 10, 50 and 100 K/sec.

Table I. Composition of the produced steels investigated

Designation	Composition (wt. pct.)						
	C	Si	Mn	Al	N	Cr	Ni
15.1Mn	0.08	1.95	15.1	1.4	0.017		
14.3Mn	0.16	2.97	14.3	0.89	0.022		
14.2Mn	0.06	1.85	14.2	2.38	0.019		
13.9Mn	0.09	2.07	13.9	2.01	0.012		
13.0Mn	0.10	1.57	13.0	0.45	0.045		
12.5Mn	0.17	2.95	12.5	1.09	0.023		
11.5Mn	0.11	2.46	11.5	0.38	0.029		
8.1Mn	0.25	2.66	8.1	2.38	0.007		
7.9Mn	0.18	3.09	7.9	0.65	0.024		
7Mn1Ni	0.08	2.16	7.82	2.01	0.004	0.039	0.93
7Mn2Ni	0.08	2.16	7.87	2.44	0.003	0.039	1.29
7Mn3Cr	0.20	2.15	7.73	2.27	0.005	3.02	1.23

Tensile bars were milled from the hot band strip according to ASTM E8 [36] using a gage length of 50 mm and width of 12.5 mm. Tensile tests were conducted at room temperature with the tensile axis parallel to the rolling direction. Tests were performed in displacement control at a rate of 0.01 mm/sec using a 245 kN servo-hydraulic test frame. Strain data was measured with a clip-on extensometer and used to determine the yield strength and modulus of elasticity.

X-ray diffraction (XRD) was performed on samples taken from the hot rolled strip after water quenching for phase identification. XRD samples were mechanically polished to 0.1 μm using diamond paste in the Longitudinal-Transverse plane (polished surface parallel to the rolling plane). Diffraction patterns were obtained with a Phillips X-pert diffractometer using a flat graphite monochromator, and a Ni filter for a Cu radiation source. Phase quantifications were calculated utilizing the Rietveld refinement described by Martin et al. [37] and adjusted for the compositions investigated. Specimens for electron back-scattered diffraction (EBSD) were mechanically polished with a 0.02 μm colloidal silica solution using a vibratory polisher and examined in longitudinal-short plane (perpendicular to both the rolling plane normal and the rolling direction). Orientation image mapping via pattern analysis was performed on a Helios NanoLab 600 using a Nordlys detector and the AZTEC software package. The electron beam was operated at an accelerating voltage of 20.0 kV and an emission current of 5.5 nA with a 0.20 μm step size during mapping. Orientation image maps and diffraction patterns were tilt corrected for the system geometry.

II. RESULTS

Martensite start temperature, M_S^{α}, as determined by dilatometry, modulus of elasticity, calculated T_0, SFE for the γ→ε transformation at room temperature using n=2, and $\Delta G_M^{\gamma\rightarrow\alpha}$ for the twelve medium manganese steels produced for this study are shown in Table II.

Formulation of the chemical dependent Young's modulus of elasticity was derived using a combination of data from the work of Speich et al. [13], and experimental data from this investigation utilizing a least squares fit. This is shown in greater detail in the Appendix. Young's modulus was calculated according to Eq. (6) where x_i is in weight percent.

$$E(GPa) = 208.2 - 35.4x_C - 7.3x_{Si} - 1.0x_{Mn} + 3.2x_{Al} + 0.64x_{Cr} - 2.0x_{Ni} - 35.1x_N \tag{6}$$

Table II. Composition and measured modulus, calculated stacking fault energy for n=2, T_0, martensite start, and driving force for transformation at the Ms.

Designation	**Measured Values**				
	Modulus (GPa)	**SFE (mJ/m^2)**	**T_0 (K), {°C}** $\gamma \leftrightarrow \alpha$	**Ms (K) {°C}** $\gamma \rightarrow \alpha, \alpha + \varepsilon$	$\Delta G_M^{\gamma \rightarrow \alpha}$ **(J/mol)**
15.1Mn	153	7.9	624 (351)	414 (141)	-1076
14.3Mn	147	5.0	609 (336)	417 (144)	-943
14.2Mn	144	16.1	667 (394)	390 (117)	-1310
13.9Mn	169	13.3	657 (384)	352 (79)	-1489
13.0Mn	168	-2.2	671 (398)	335 (62)	-1811
12.5Mn	160	6.8	655 (382)	355 (82)	-1606
11.5Mn	181	-1.8	701 (428)	409 (136)	-1575
8.1Mn	182	23.5	762 (489)	429 (156)	-1707
7.9Mn	173	6.2	767 (494)	458 (185)	-1716
7Mn1Ni	186	20.2	818 (545)	505 (232)	-1740
7Mn2Ni	211	25.6	823 (550)	473 (200)	-1549
7Mn3Cr	166	26.9	726 (453)	361 (88)	-1785

Thirty additional alloys from literature [10, 38-43] were also incorporated into the analysis and the reported values for the M_S^{α}, calculated Young's modulus using eq. (6), and the $\Delta G_M^{\gamma \rightarrow \alpha}$ are included in the Appendix. A plot of $-\Delta G_M^{\gamma \rightarrow \alpha}$ versus M_S^{α} is shown in Figure 2 where it was found that separating the data into two populations was required to resolve the data into distinct trend lines. Alloys containing less than 12 wt. pct. Mn produced a behavior similar to what Raghavan and Anita reported [16], and what Jicheng and Zhanpeng [15] proposed for microstructures containing lath martensite. Greater temperature dependence is observed for alloys containing greater than 12 wt. pct. Mn and is similar to what Jicheng and Zhanpeng [15] proposed for plate martensite structures.

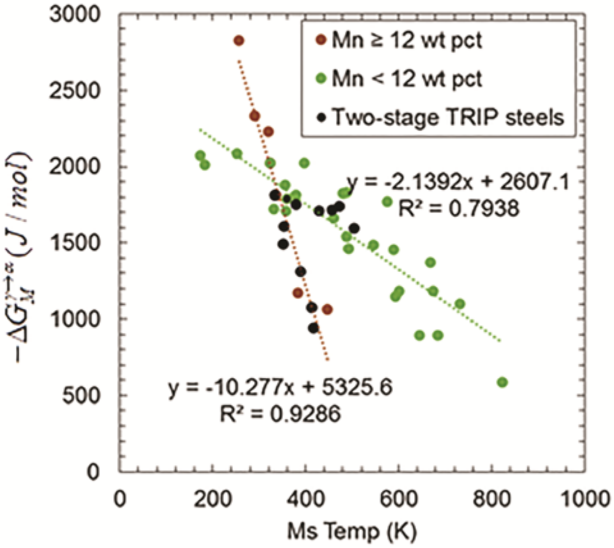

Fig. 2. Plot of the $-\Delta G_M^{\gamma\rightarrow\alpha}$ as a function of M_S^α temperature. Two distinct relationships can be found between the martensite start and the driving force for transformation at the martensite start temperature based on the Mn content in the steels. The two-stage TRIP steels are shown in black.

A. Incorporation of Young's Modulus and Application of SFE Model to Calculate M_S^α

The strain energy of transformation is expected to be a function of the moduli of both parent and product phases. For steel the difference in modulus between γ-austenite and α-martensite is expected to be small as reported by Ghosh and Olson [44] and both γ-austenite and α-martensite would have similar dependence upon composition. The strain energy would also be dependent upon the transformation temperature and increase as the M_S^α temperature decreased. A plot of $-\frac{\Delta G_M^{\gamma\rightarrow\alpha}}{E\Omega\delta^2}$ vs the M_S^α is shown in Figure 3, where E is the modulus calculated according to eq. (6), using units of Pa, Ω is the molar volume calculated for iron $7.15*10^{-6}$ (m^3/mol), δ is the lattice misfit between the γ-austenite and α-martensite with an approximate strain value of $1.11*10^{-2}$ (m/m), and T is the temperature in Kelvin. A single trend line was used to represent both data sets with the compositional limits for the data shown in Table III.

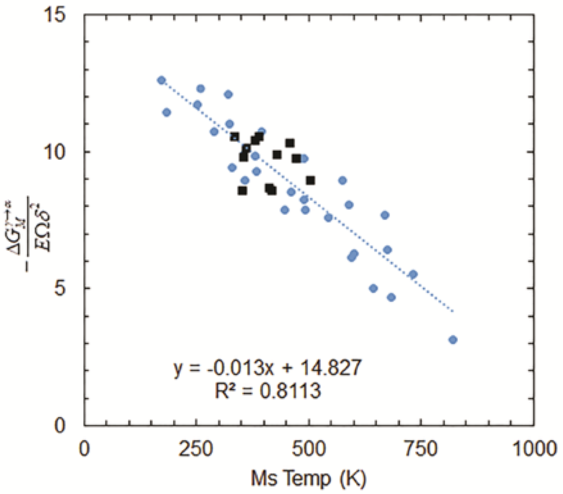

Fig. 3. The relationship between the $-\Delta G_M^{\gamma\to\alpha}$ normalized to the modulus of elasticity (E), molar volume (Ω), and lattice misfit (δ) as a function of the M_S^α with two-stage TRIP steels are shown as black squares.

Table III. Compositional limits in weight Percent for the 39 alloys found in literature and produced used for the model development with 173K (-100 °C) < M_S^α <822K (549 °C) (450K, (177 °C) average)

	C	**Si**	**Mn**	**Al**	**N**	**Cr**	**Ni**
Min	0	0	0	0	0	0	0
Max	0.3	3.09	15.7	2.44	0.614	17	15.1
Ave	0.08	1.8	8.2	1.3	0.126	8.9	5.8

A temperature and composition dependent strain energy relationship was derived from Figure 3 that must be overcome to form the α-martensite within the parent γ-austenite and this relationship is given in Eq. (7)

$$\Delta G_{Str}^{\gamma\to\alpha}(J/mol) = E\Omega\delta^{2}(14.8-0.013T) \tag{7}$$

The temperature at which the sum of $\Delta G_{Chem}^{\gamma\to\alpha}$ and $\Delta G_{Str}^{\gamma\to\alpha}$ is zero is the point at which the stacking fault energy of the martensitic embryo is zero and there is no restrictive force acting on the $\frac{a}{2}<1\bar{1}0>_{\gamma}$ dislocation to separate as partials. A comparison of the calculated vs. measured M_S^{α} for the 42 investigated alloys is shown in Figure 4(a), and a scatter band of ± 100K (100 C°) is shown for reference. For comparison, two different empirical models, Eq. (1) and Eq. (3) are shown in Figure 4(b) for the same alloys.

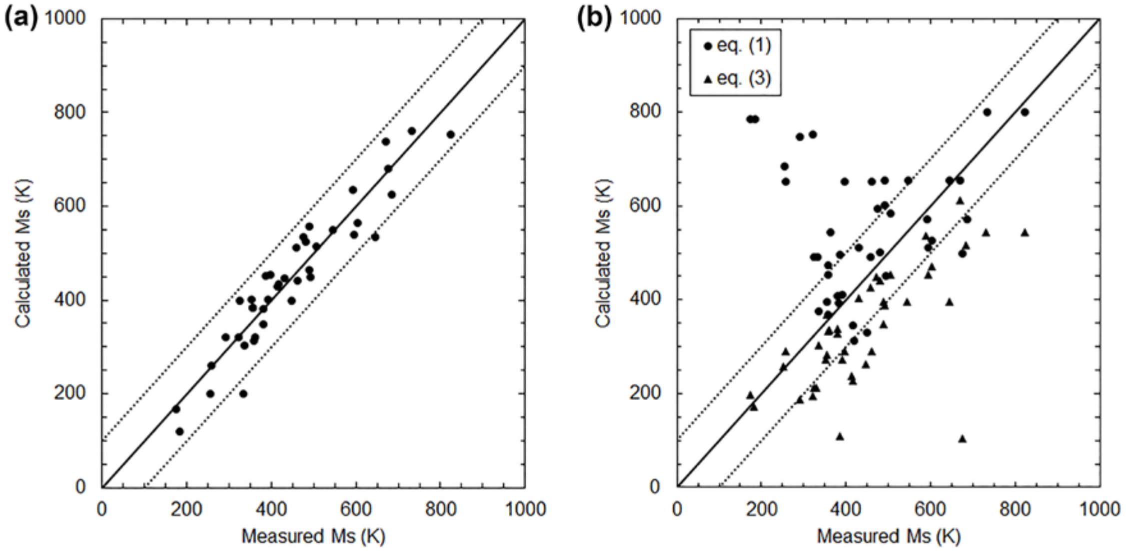

Fig. 4. (a) Correlation between the measured Ms^{α} and calculated for the proposed strain model compared to (b) two empirical models from DeCooman and Speer [14] for the same alloys shown in (a). Equation 1 shows a poor fit to the data since many of the alloys used in the plot contain Ni and Cr. In a similar fashion, alloys containing aluminum fall below the identity line since the temperature increase associated with aluminum is not included in Equation 3.

III. DISCUSSION

This study shows that the inclusion of a compositionally dependent Young's modulus, as included in the strain energy of transformation, has the ability to predict a martensite start temperature independent of martensite morphology. As done in previous studies, a regular thermodynamic solution model was used to determine the driving force for transformation at the measured martensite start temperature and was related to the strain energy that must be overcome during transformation. While this approach of showing $\Delta G_M^{\gamma\rightarrow\alpha}$ as a function of temperature has been used by other authors in previous works [23, 45-46], the work presented here has shown that a single relationship for both lath and plate martensite can be produced by considering a compositional dependent Young's modulus. Highly alloyed steels in the present study, have a low Young's modulus, and according to the proposed model, a lower strain energy. Thus the required chemical driving force to overcome the strain energy of transformation is lower and this translates into a smaller undercooling below T_0 and a higher Ms temperature.

For manganese contents greater than 12 wt. pct., the temperature dependent term shown in Figure 2 is within 2 pct. of what Jicheng and Zhanpeng [15] showed for plate martensites that are internally twinned. Athermal α-martensite reported by Pisarik and Van Aken [47] for the 14.3Mn alloy is shown to be plate-like when nucleated within the ε-martensite and the plate variants are twin related. Further work to classify the internal structure of the martensites will be a topic of a future study. However, Holden et al. reported that α-martensite plates were not internally twinned when nucleated within the ε-martensite and the internal structure was the result of slip [11].

The model proposed here covers a wide range of compositions and can be applicable to even low alloy steels reported by Atkins [48]. However, due to the broad range of alloys and temperatures, the scatter found in Figure 4(a) of ±100K (100 C°) is larger than desired. Inclusion of a compositional dependence for the molar volume and a temperature dependence for the unconstrained misfit is expected to decrease the uncertainty, but adds considerable complexity to the model.

Ghosh and Olson [46] attempted a similar thermodynamic approach to the martensite start of 41 alloys incorporating a chemical and temperature dependent term, which investigated both dilute and solute rich binary alloys but ignored magnetic interactions. They proposed a compositional dependent term based on the interfacial frictional work of the martensitic interface according to Eq. (8).

$$W_{\mu} = \sqrt{\sum_i (K_{\mu}^{i} X_i^{0.5})^2} + \sqrt{\sum_j (K_{\mu}^{j} X_i^{0.5})^2} + \sqrt{\sum_k (K_{\mu}^{k} X_i^{0.5})^2} + K_{\mu}^{Co} X_{Co}^{0.5} \tag{8}$$

where K_{μ} is the athermal strength of different solutes and i = C, N; j = Cr, Mn, Mo, Nb, Si, Ti, V; and k = Al, Cu, Ni, W, which where experimentally determined according to the flow stress for slip deformation of single crystals as a function of composition. Ghosh and Olson theorized that each solute atom acted as obstacles for slip deformation, similarly to what Grujicic et al. [23] assumed with respect to point defects. Ghosh and Olson concluded that the solute atoms acted as barriers to the mobility of the martensitic interface with little differentiation between solute types [46]. However, both studies assumed that chemical and electronic interactions and the modulus were incorporated in the measured athermal strength. Ghosh and Olson noted that their work was based only on binary systems ranging from the dilute to highly concentrated, but felt their results might not be globally applicable to multicomponent systems [46]. In contrast to prior work, the work presented here was an attempt to look at a multicomponent approach using the Young's modulus.

Surprisingly, Al is found to have a positive effect on the modulus in Eq. (6) and this appears to relate to an increase in the M_S^{α}. Work by Takeuchi [45] found that aluminum had a negative effect on the shear modulus; however, the works by both Tackeuchi [45] and Speich et al. [43] investigated binary systems solely. The works of both Tackeuchi and Speich stated that these effects are potentially not additive to the modulus in multicomponent systems. Interstitial carbon and nitrogen have the strongest negative impact on the Young's modulus as shown in Eq. (6). It should be noted that addition of aluminum is expected to increase the AlN solvus temperature and reduce the amount of nitrogen in solid solution by the precipitation of AlN. Thus, the positive increase in modulus resulting from aluminum addition may be interpreted as nitrogen mitigation and as a result, aluminum is observed as a positive contributor to the Young's modulus in the work presented here.

Utilizing the results of Pisarik and Van Aken [20] and the results presented here M_S^{α} and M_S^{ε} can be calculated and compared to the microstructural constituents of the seven two-stage TRIP alloys (reported in Table IV) containing ε-martensite in the starting microstructure. Each alloy was in a reheated to a fully austenitic state and water quenched. In addition, a two-stage TRIP steel reported by Yang et al. [49] and four alloys from Kim et al. [50] were also considered. A comparison of the reported phase fractions from these studies show that the volume percent retained γ-austenite is related to the difference between the M_S^ε and M_S^α as shown in Figure 5, which hopefully demonstrates the utility of the proposed methodology for predicting start temperatures. These results also suggest that an initial transformation to ε-martensite $\left(M_S^\varepsilon > M_S^\varepsilon\right)$ should be nearly complete with room temperature retained γ-austenite less than 10 vol. pct. Formation of ε-martensite would then reduce the chemical driving force and lower the α-martensite start temperature. It should be noted that the start temperature for ε-martensite was determined using n=4 in equation (4). Larger values of n would cause the ε-martensite to form at even higher temperatures. This may suggest that retention of γ-austenite is dependent upon nucleating α-martensite and removing the chemical driving force for potential ε-martensite embryos.

Table IV. Volume pct. phases of seven two-stage TRIP steels presented in the current work and the five alloys from literature.

Designation	**Volume pct. Phase from XRD**		
	γ	**ϵ**	**α**
15.1Mn	26.1	32.4	41.2
14.3Mn	27.6	46.5	25.9
14.2Mn	68.3	3.7	28
13.9Mn	41.1	27.2	31.8
13.0Mn	1.0	60.2	38.8
12.5Mn	12	83	5
11.5Mn	5.7	24.8	69.5
[48]	93	7	0
[49]	72.6	27.4	0
[49]	69.1	30.9	0
[49]	48.8	51.2	0
[49]	91.8	8.2	0

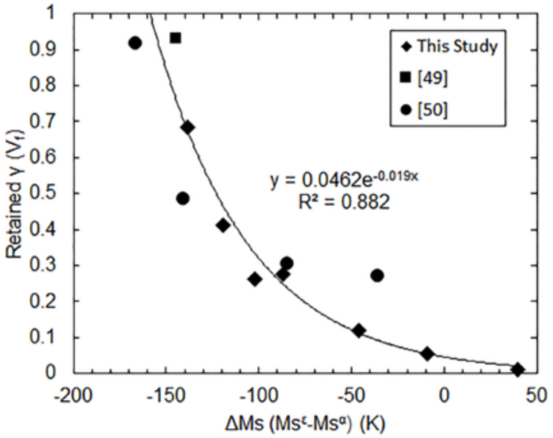

Fig. 5. Relationship between the retained γ-austenite and the difference between the start temperatures of the ε- and α-martensites. The relationship shows similarity to a Koistinen-Marburger type relationship.

It is now possible using the work of Pisarik and Van Aken [20] and the work presented here to predict the effect of alloying elements in the medium-Mn steel. Plots of $\Delta G_{Chem}^{\gamma\rightarrow\varepsilon}$ at room temperature, the M_S^{ε} temperature, the M_S^{α} temperature, and the difference between the M_S^{ε} and M_S^{α} are shown in Figure 6 with respect to Mn, Si, and Al content with C and N fixed at 0.07 and 0.017 wt. pct. as previously done in reference [20]. Upon review of Figure 6(a) it is observed that the ε-martensite becomes more stable relative to α-martensite by increasing Mn. Increases in either Si or Al decrease the stability of ε-martensite and these results appear to be in good agreement with the reported first principles work of Limmer et al. [51] showing that Al and Si increase the intrinsic stacking fault energy. This is corroborated by Yang et al. [49], for an alloy that contained 0.24C-0.15Si-21.5Mn-balFe (wt. pct.) and shows a duplex γ-austenite and ε-martensite microstructure. From Figure 6(b), a maximum in the M_S^{ε} temperature occurs at roughly 12.5-13 wt. pct. manganese and M_S^{ε} decreases as aluminum content increases. In Figure 6(c) the effect of manganese content on the M_S^{α} is shown to produce a minimum at 12.5 wt. pct. Mn leading to an M_S^{α} of about 320K (47 °C) and the M_S^{α} increases in temperature as aluminum is increase from 0.5 to 2.5wt. pct. The minima in M_S^{α} narrows in manganese composition and shifts slightly to a lower manganese content of 12.25 wt. pct. as aluminum content increased. Medvedeva et al. [18] calculated a minimum in the intrinsic stacking fault energy at a manganese concentration of 12 at. pct., equivalent to 12.2 wt. pct. Mn, and this minima appears to be expressed in the thermodynamic model proposed by Pisarik and Van Aken [20] for a maximum in M_S^{ε}, and the current model for a minimum in the M_S^{α} at 12.5 wt. pct. Mn. Aluminum appears to increase the M_S^{α} as reported by most empirical models, as observed in Figure 6(c) where a narrowing of the minimum of the contour map occurs as aluminum is increased. This is assumed to be an effect of increasing the intrinsic stacking fault energy and a reduced N content in solution as nitrogen is known to depress the M_S^{α}. Removal of nitrogen from solid solution would also increase the intrinsic stacking fault energy in the steel, since nitrogen has been shown by first principle calculations to decrease the intrinsic stacking fault energy. [52-54]

At manganese concentrations greater than 15 at. pct., Acet et al. noted that α-martensite was no longer observed upon quenching as shown in Fig. 1(a). This observation may be explained by the decreasing chemical driving force $\Delta G_{Chem}^{\gamma\rightarrow\varepsilon}$ as manganese is increased as shown in Fig. 6(a). However, this assumes ε-martensite forms first. It is observed that in Figure 6(c) the M_S^{α} is increasing up to a temperature of 525K (252 °C) at a manganese content of 19 wt. pct.; and clearly, this result is not observed in reported literature nor in the results of this study. From this and the observed compositional range of Table III it should be understood that the proposed model is not applicable for manganese contents greater than 15 wt. pct. The extended range of manganese compositions shown in Fig. 6 are presented to demonstrate the limits of the model calculations.

Figure 6(d) combines the data of both Figures 6(b) and 6(c) to produce a phase map prediction where M_S^{ε} is greater than M_S^{α}. It can be observed that to produce an alloy that will first transform to ε-martensite and then transform to α-martensite would require a composition of 13 wt. pct. Mn and less than 0.5 wt. pct. Al. However, Pisarik and Van Aken [47] reported that a 15.1Mn alloy in the as-cast condition exhibited both athermal martensitic reactions. This can be explained by considering segregation during solidification. A Scheil-Gulliver segregation model in FactSage™ was used to calculate the composition of the last 15% by weight liquid and represents the alloy segregated region defined as “Rich” in Table V. The “Lean” values reported in Table V were calculated by mass balance to yield the “Bulk” composition. It is observed that the first 85% (solute lean) to solidify has an average composition of 0.05C–1.660Si–13.9Mn–1.1Al–0.007N-balFe (wt. pct.) which leads to an $M_S^{\varepsilon} = 387K\left(114^{o}C\right)$ and an $M_S^{\alpha} = 396K\left(96^{o}C\right)$ which should lead to a two-stage athermal martensite transformation as previously shown by Pisarik and Van Aken[47].

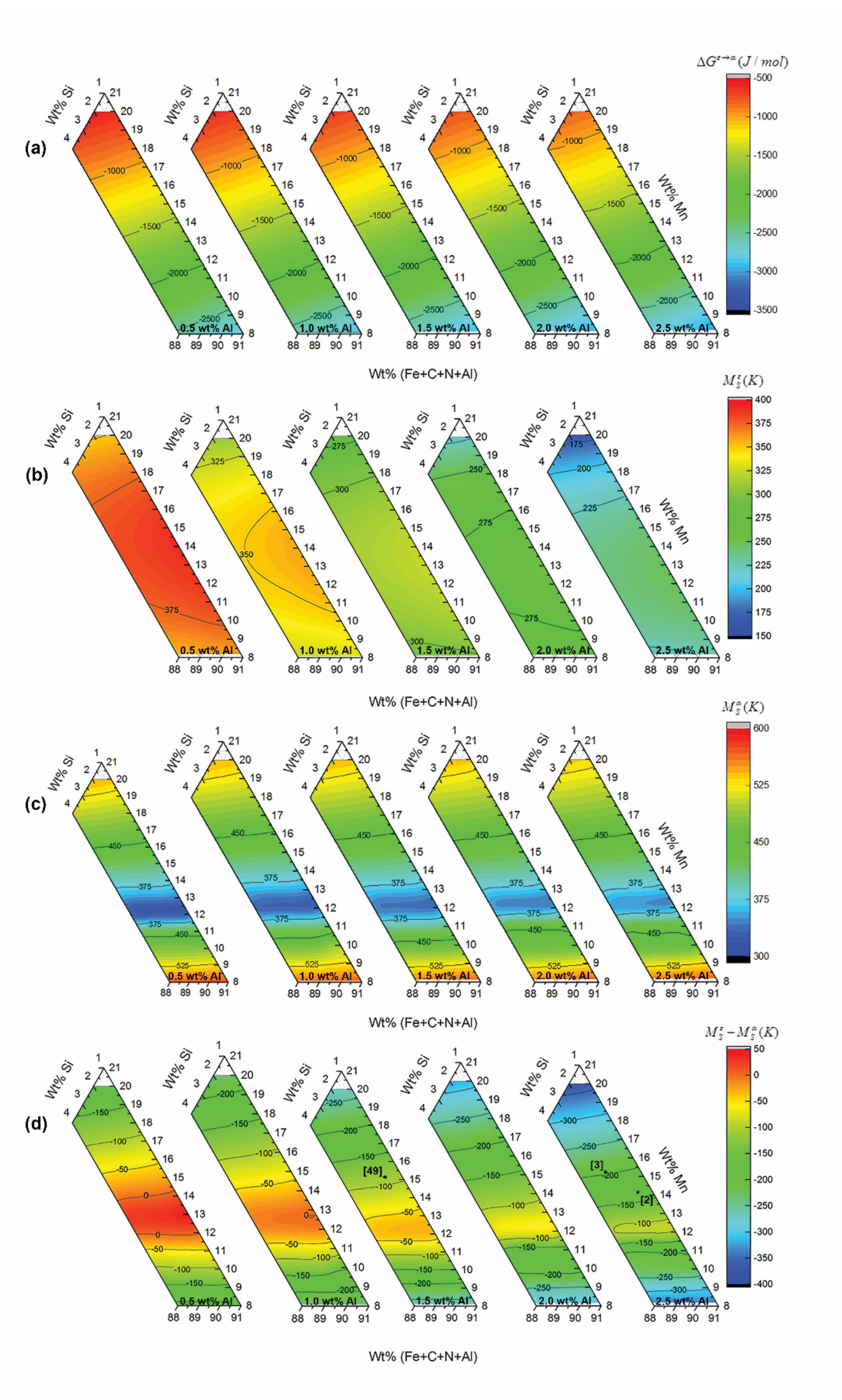

Fig 6. Effect of composition on (a) the $\Delta G^{\gamma\to\varepsilon}_{Chem}$ (b) M_S^{ε}, (c) M_S^{α} and (d) the difference of the start temperatures $\left(M_S^{\varepsilon}-M_S^{\alpha}\right)$ in the Fe, Mn Al Si system. Value of 0.07 wt. pct. C and 0.017 wt. pct. N were held constant.

Table V. Calculated compositions of the chemically segregated regions and martensite start temperatures of the 15.1Mn, 14.3Mn, and 11.5Mn alloys.

Alloy		**C**	**Si**	**Mn**	**Al**	**N**	**Ms^{ε} n=4 (K) {°C}**	**Ms^{ε} n=8 (K) {°C}**	**Ms^{α} (K) {°C}**
15.1Mn	Bulk	0.08	1.95	15.1	1.4	0.017	315 (42)	361 (88)	424 (151)
	Lean*	0.05	1.66	13.9	1.1	0.007	387 (114)	390 (117)	369 (96)
	Rich*	0.16	3.59	21.6	3.0	0.047	112 (-161)	140 (-133)	522 (249)
14.3 Mn	Bulk	0.16	2.97	14.3	0.89	0.022	336 (63)	380 (107)	427 (154)
	Lean	0.11	2	12.3	0.92	0.015	355 (82)	388 (115)	344 (71)
	Rich	0.17	3.2	18.0	0.63	0.067	331 (58)	379 (106)	536 (263)
11.5 Mn	Bulk	0.11	2.46	11.5	0.38	0.029	378 (105)	421 (148)	410 (137)
	Lean	0.09	1.90	11.3	0.39	0.017	383 (110)	427 (154)	427 (154)
	Rich	0.14	2.60	12.7	0.32	0.053	379 (106)	412 (139)	323 (50)

A similar result can be shown for the 14.3Mn alloy presented here and a combined EBSD-OIM/EDS map is shown in Figure 7. The EDS mapping of Mn and Si show bands of high and low concentration parallel to the rolling direction. Solute rich regions are marked with arrows, and these bands are denoted by letters on both the EDS and EBSD-OIM maps. The solute rich regions are primarily comprised of γ-austenite and ε-martensite, which is in agreement with the expected phases in the works by both Acet et al. [10] and Yang et al. [49]. Solute lean regions are comprised of α-martensite, which nucleated within the ε-martensite and γ-austenite. As shown in Table V, the solute lean areas are found to have a composition of 0.11 C – 2.00Si – 12.3Mn – 0.92Al – 0.015N-balFe (wt. pct.). This composition according to the proposed model would have an $M_S^{\alpha} = 344K\left(71^oC\right)$ and an $M_S^{\varepsilon} = 355K\left(82^oC\right)$ using an n = 4, for a well-annealed γ-austenite. The Mn and Si rich regions are dominated by ε-martensite as might be predicted in Figure 1. The proposed model incorrectly predicts α-martensite for these segregated regions as shown in Table V for the as-solidified microstructure. Again, this demonstrates the limitation of the proposed model to manganese compositions less than 15 wt. pct. It has been shown by De Cock et al. [55] that rolling direction can affect the A_c1 and A_c3, which would imply a dependence of the Ms temperature upon the rolling direction. However, no discernable texture was observed in the EBSD-OIM studies reported here.

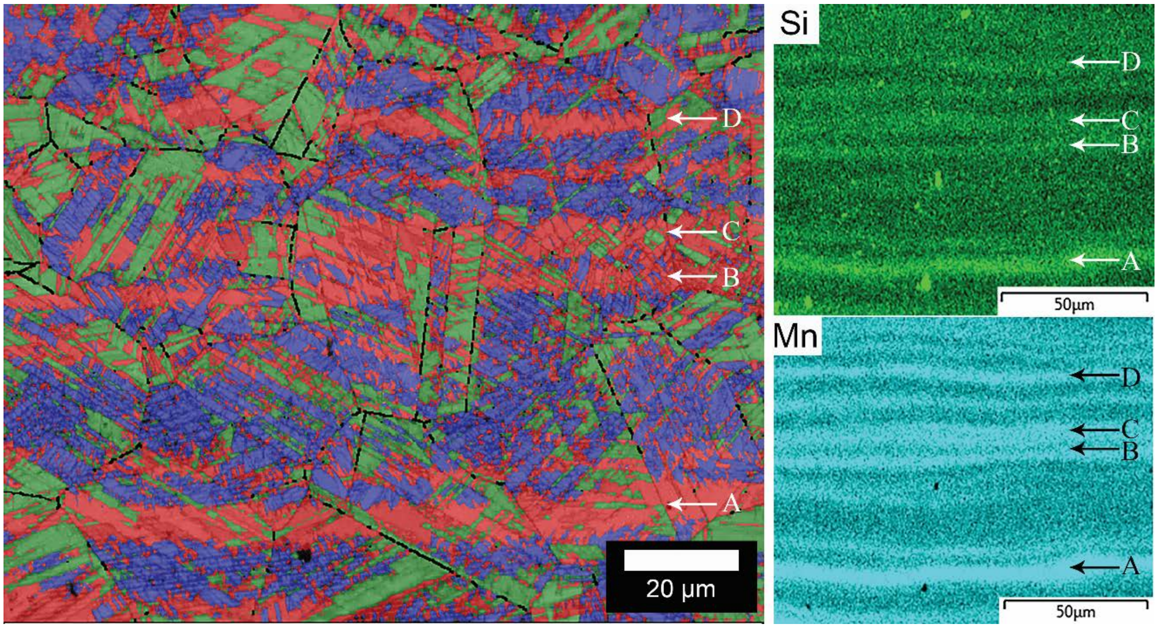

Fig. 7. An EBSD-OIM image (left) of the 14.3Mn alloy where γ-austenite is green, ε-martensite is red and α-martensite is blue. An EDS map of the Si (upper right) and Mn (lower right) of the same area is shown on the right, with areas of high concentration showing greater intensity in color.

At this point it is instructive to look at the 11.5Mn alloy and a similar mapping of EBSD-OIM/EDS is shown in Figure 8. The segregation analysis is shown in Table V. Here the solute-rich region is predicted to have an M_S^{ε} (for an n=4) which is 379K (106°C) and a M_S^{α} of 323K (50°C). The phase mapping shows a combination of ε-martensite, α-martensite and γ-austenite, which is in reasonable agreement with the model. A predominately α-martensite microstructure is observed in the solute lean regions, which is expected when M_S^{α} (427K or 154°C) is greater than M_S^{ε} (383K or 110°C). A consideration of $M_S^{\varepsilon} - M_S^{\alpha}$ would suggest that the solute lean regions would contain greater γ-austenite and the opposite is observed in Figure 8. It should be noted, however, that the values predicted from Figure 5 are calculated according to the bulk chemistry. Furthermore, the microstructures examined in Figure 7 and Figure 8 have some degree of homogenization from thermomechanical processing and the uncertainty in the calculated M_S^{α} as shown in Figure 4(a) is ±100K (100 C°). Thus, the prediction of the microstructure appears quite reasonable if one works within the limitation of the proposed model.

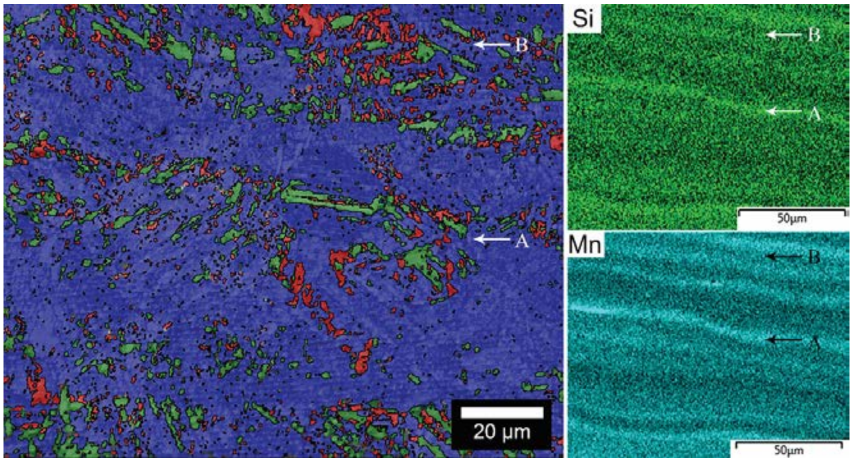

Fig 8. An EBSD-OIM image (left) of the 11.5Mn alloy in the reheated and water quenched condition where γ-austenite is green, ε-martensite is red and α-martensite is blue. An EDS map of the Si (upper right) and Mn (lower right) of the same area is shown on the right, with areas of high concentration showing greater intensity in color. Sensitivity to processing can be demonstrated using the 11.5Mn alloy.

Figure 9 shows the EBSD-OIM phase mapping after the alloy had been air cooled directly after the final hot rolling pass. The exit temperature from the rolling mill was measured to be 1048K (775°C). The γ-austenite volume fraction was measured to be 24.3 pct. versus 5.7 pct. in the annealed and water quenched condition as shown in Figure 8. The difference in retained γ-austenite for the reheated and water quenched sample (Figure 8) as compared to a specimen that was air cooled directly after final rolling could be due to stresses caused during quenching. Stresses developed during rapid temperature and volume change may lead to stress induced martensite as opposed to athermal martensite. It is interesting to note that in both the air cooled and water quenched sample the volume percent of ε-martensite is the same 24 pct. It has been well documented [50, 56] that the transformations from γ→ε results in a volume contractions compared to the γ→α transformation, which is a volume expansion. Thus, the ε-martensite acts as an internal stress relief for thermal contraction and may be promoted during quenching. M_S^ε is very sensitive to nucleating defect size (n) in the SFE equation [20,21] as well as grain size [57-59]. The nucleating defect size of n = 4 assumes a well annealed state and this might not be appropriate for the processing performed here or in previous studies [2, 3, 9]. Yang et al. [56] produced the well-annealed state after 2 days of homogenization at 1473K (1200 °C). The effect of changing the defect size for a fixed 0.11C-0.38Al-0.029N-balFe alloy with varying amounts of Mn and Si is also shown in Figure 9. If a defect size of n=8 is considered for the ε-martensite, the region of $M_S^\varepsilon - M_S^\alpha > 0$ expands to a composition range of 11.4-15.3 wt. pct. Mn and a Si content greater than 1 wt. pct. as shown in Figure 9. Table V shows that an n=8 value produces a martensite start temperature 44K (44 °C) higher than the n=4 case for ε-martensite of the lean composition. The difference in martensite start temperatures becomes zero and both martensite types would be expected in the microstructure for the bulk and lean composition. If α-martensite had formed first there would be no chemical driving force to form ε-martensite. Clearly more work is required to understand these alloys, but the proposed model does provide explanatory power when investigating microstructure and processing relationship in these mid-manganese steels.

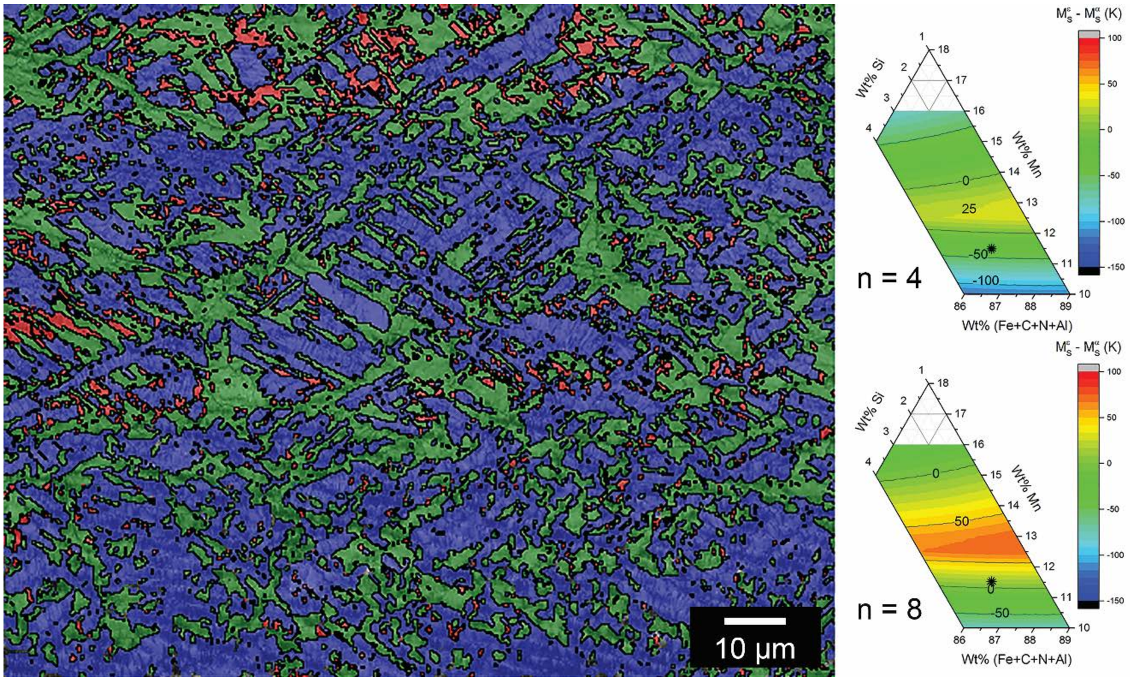

Fig. 9. EBSD-OIM image (left) of the 11.5Mn alloy in the air cooled condition where γ-austenite is green, ε-martensite is red and α-martensite is blue. The Ms^ε-Ms^α (right) is shown for a fixed 0.11 wt. pct. C, 0.38 wt. pct. Al, and 0.029 wt. pct. N corresponding to the 11.5Mn alloy. A nucleating defect of n = 4 (upper right) is used to calculate the Ms^ε, and a value of n = 8 (lower right) to calculate the Ms^ε.

IV CONCLUSION

A new composition based method for calculating the chemical driving force of the γ→α transformation, $\Delta G_{Chem}^{\gamma\rightarrow\alpha}$, using a regular solution model has been used to predict the strain energy necessary to overcome for the formation of α-martensite. A composition and temperature dependent strain energy $\Delta G_{Str}^{\gamma\rightarrow\alpha}$ has been proposed for the formation of α-martensite, and by setting $\Delta G_{Chem}^{\gamma\rightarrow\alpha} + \Delta G_{Str}^{\gamma\rightarrow\alpha} = 0$, an M_S^{α} can be determined. The role of the chemical dependent Young's modulus, lattice misfit, and molar volume is important in providing a unified expression between $\Delta G_{Chem}^{\gamma\rightarrow\alpha}$ and M_S^{α} for both lath and plate martensites. This model has shown good correlation between the measured start temperature for 42 different alloys with large variations in composition and start temperatures. A microstructural relation was also shown for the volume fraction retained γ-austenite and the difference between the calculated M_S^{α} and M_S^{ε} of twelve different ε-martensite containing alloys. The model has an uncertainty of ± 100K (100 C°), but within this uncertainty the model has explanatory power for the microstructures observed in mid-manganese steels. The model is limited in its ability to predict α-martensite to compositions less than 15wt. pct. Mn. Processing history was also shown to play a role in the prediction of ε-martensite and that using a larger n=8 value for the ε-martensite embryo size can provide better correlation to the observed microstructure. It might be concluded from the work presented here that if sufficient fitting parameters are used any phenomenon can be modeled. The ability to model both lath and plate martensite, however, shows that the methodology has utility and justifies further study.

ACKNOWLEGEMENTS

This work was supported by the Peaslee Steel Manufacturing Research Center (PSMRC). Companies directly involved in this work include AK Steel, Areclormittal, Nucor Steel, and U. S. Steel. The FEI Helios NanoLab dual beam FIB was obtained with a Major Research Instrumentation grant from the National Science Foundation under contract DMR-0723128. The authors also acknowledge the support of the Materials Research Center and in particular Dr. Clarissa Wisner, Dr. Jessica TerBush and Dr. Eric Bohannan for guidance and training in using the FIB and performing the XRD work. The assistance from Dr. Daniel Baker while employed at AK Steel on performing the dilatometry of the alloys shown in Table II is kindly acknowledged. Finally, the support from US Steel and Todd Link for casting and hot rolling the 7Mn1Ni, 7Mn2Ni, and 7Mn3Cr alloys was greatly appreciated.

APPENDIX

Alloying elements alter the Gibb's free energy change for the γ→α transformation by $\Delta G_i^{\gamma\rightarrow\alpha}$, which is determined using eq. (A1). The interaction parameter in the iron-based system for a solid solution is represented as $\Delta\Omega_{Fe(i)}^{\gamma\rightarrow\alpha}$, which is calculated using eq. (A2). The values for the $\Delta G_i^{\gamma\rightarrow\alpha}$ and $\Delta\Omega_{Fe(i)}^{\gamma\rightarrow\alpha}$ for the alloying element, i are shown in Appendix Table AI.

$$\Delta G_i^{\gamma\rightarrow\alpha} = G_i^{o\,\alpha} - G_i^{o\,\gamma} \tag{A1}$$

$$\Delta\Omega_{Fe(i)}^{\gamma\rightarrow\alpha} = \Omega_{Fe(i)}^{\alpha} - \Omega_{Fe(i)}^{\gamma} \tag{A2}$$

To calculate the modulus, data from Speich et al [13] was used for C, Mn, Cr, and Ni from the data in Figure A1. To determine the effect of Si, Al, and N the modulus is calculated for the known alloys in Appendix Table AII with elements Ni, Cr, Mn and C. The difference between the calculated modulus and the measured modulus is fit with a least squares fit for the elements Si, Al, and N.

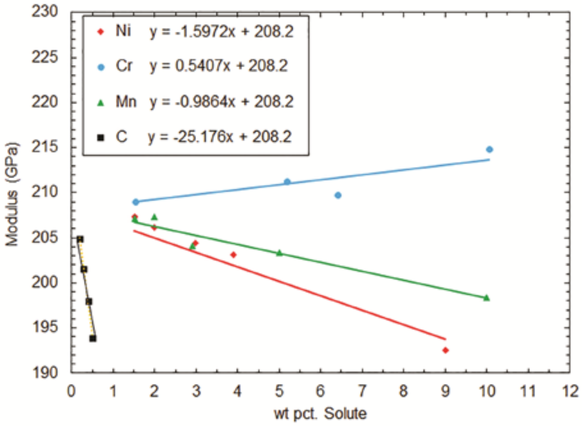

Figure A1. Data for the effect of alloying element on the modulus of steel. Adapted from Ref. [13].

Appendix Table AI: Equations for Free Energy and Interaction Parameter Difference Used

Free Energy Difference (J/mol) (T in K)		Interaction Parameter Difference (J/mol) (X_i in atomic fraction)	
Fe	$\Delta G^{\gamma\rightarrow\alpha} = 1{,}462.4 - 8.282T + 0.64*10^{-3}T^2 + 1.15T*\ln(T)$	Fe(Fe)	---
Mn	$\Delta G^{\gamma\rightarrow\alpha} = -1{,}477 + 0.514T - 2.74*10^{-3}T^2 + 1.65*10^{-6}T^3$	Fe(Mn)	$X_{Fe}(4{,}100+4.69T)+X_{Mn}(5{,}188+1.51T)-(16.99T-18{,}870)$
Si	$\Delta G^{\gamma\rightarrow\alpha} = 4{,}000 - 0.7T$	Fe(Si)	$7{,}113*(X_{Fe} - X_{si})$
Al	$\Delta G^{\gamma\rightarrow\alpha} = 10{,}083 - 4.813T$	Fe(Al)	$-7{,}280X_{Fe} - 62{,}760X_{Al}$
C	$\Delta G^{\gamma\rightarrow\alpha} = 8{,}368$	Fe(C)	$(59{,}412-34.9T) * (X_{Fe} + X_C)$
Cr	$\Delta G^{\gamma\rightarrow\alpha} = -7{,}284 - 0.163T$	Fe(Cr)	$17{,}699 - 4.18T$
Ni	$\Delta G^{\gamma\rightarrow\alpha} = 8{,}715.1 - 3.556T$	Fe(Ni)	$5230 - 8.37T$

Appendix Table AII. Composition of the 42 alloys and the reported measured Ms^{α}, driving force for transformation at the Ms^{α} and the modulus.

Source	**C**	**Si**	**Mn**	**Al**	**Cr**	**Ni**	**N**	**Ms^{α} (K)**	**$\Delta G^{\gamma\rightarrow\alpha}$ (J/mol)**	**E (GPa)**
Present Work	0.086	2.07	13.9	2.01	-	-	0.0116	352 (79)	-1489	168
	0.16	2.97	14.3	0.89	-	-	0.0224	417 (144)	-943	147
	0.06	1.85	14.2	2.38	-	-	0.019	390 (117)	-1310	144
	0.0767	1.95	15.1	1.4	-	-	0.0173	413 (140)	-1076	153
	0.17	2.95	12.5	1.09	-	-	0.0228	354 (81)	-1606	160
	0.1	1.57	13.0	0.45	-	-	0.045	335 (62)	-1811	168
	0.08	2.16	7.82	2.01	0.039	0.93	0.004	505 (232)	-1594	187
	0.078	2.16	7.87	2.44	0.039	1.29	0.003	473 (200)	-1740	211
	0.2	2.15	7.73	2.27	3.02	1.23	0.005	361 (88)	-1785	186
	0.18	3.09	7.9	0.65	-	-	0.024	457 (184)	-1716	175
	0.25	2.66	8.1	2.38	-	-	0.007	428 (155)	-1707	182
	0.11	2.46	11.5	0.38	-	-	0.029	409 (136)	-1575	181
[40]	0.006	0.01	15.7	-	-	-	-	447 (174)	-1063	176
	0.0023	0.0005	9.28	-	-	-	-	602 (329)	-1185	189
[42]	0.022	-	10.24	-	8.19	-	0.206	323 (50)	-1763	184
	0.012	-	5.03	-	11.7	-	0.614	257 (-16)	-2829	210
	0.10	2.7	-	-	17	4	-	290 (17)	-2330	201
	0.1	2	-	-	17	4	-	320 (47)	-2230	194
	0.014	-	10.13	-	12.23	-	0.018	384 (111)	-1115	143
	0.06	-	-	-	13	14.2	0.15	183 (-90)	-2011	185
	0.06	-	-	-	11.5	15.1	0.15	173 (-100)	-2075	183
	0.3	-	-	-	9	11	-	253 (-20)	-2085	187
	0.14	-	4.95	-	8.19	-	0.206	489 (216)	-1540	196
[10]	-	-	14.8	-	-	-	-	457 (184)	-1063	179
	-	-	11.83	-	-	-	-	492 (219)	-1460	184
	-	-	9.85	-	-	-	-	594 (321)	-1149	188
	-	-	7.88	-	-	-	-	684 (411)	-892	197
[41]	-	-	13.7	-	-	-	-	380 (107)	-1815	194
	-	-	10.2	-	-	-	-	480 (207)	-1822	198
[39]	0.2	1.5	2	-	0.6	-	-	668 (395)	-1371	189
[38]	0.017	-	0.12	-	8.1	-	0.017	822 (549)	-589	211
	0.017	-	0.12	-	8.1	-	0.206	731 (458)	-1103	204
	0.014	-	4.95	-	7.8	-	0.011	644 (371)	-898	201
	0.014	-	4.95	-	7.8	-	0.258	545 (272)	-1487	193
	0.014	-	4.95	-	7.8	-	0.387	489 (216)	-1829	188
	0.022	-	10.24	-	8.19	-	0.206	331 (58)	-1720	184
	0.008	-	0.094	-	12.5	-	0.257	674 (401)	-1183	185
	0.012	-	5.03	-	11.7	-	0.29	460 (187)	-1662	194
	0.012	-	5.03	-	11.7	-	0.466	396 (123)	-2026	187
[43]	0.30	2.0	10.0	3.0	-	-	-	357 (84)	-1711	173
	0.40	2.0	8.00	3.0	-	-	-	355 (82)	-1877	173

REFRENCES

[1] Q. Li, Xu. Huang, and W.Huang, *Met. Sci. & Eng.*, 2016 vol. 662, pp. 129-135

[2] D.C. Van Aken, S.T. Pisarik, and M.C. McGrath, *Proceedings of the Intl. Symp. on New Developments in Advanced High-Strength Steels*, Vail, Colorado, 2013, pp. 119-129.

[3] M.C. McGrath, D.C. Van Aken, N.I. Medvedeva, and J.E. Medvedeva, *Metall. Mater. Trans. A*, 2013, vol. 44A, pp. 4634-4643.

[4] S.T. Pisarik, D.C. Van Aken, K.Limmer, and J.E. Medvedeva, *AIST2014 Proceedings*, pp. 3013-23

[5] A.J. Clark, J.G. Speer, M.K. Miller, R.E. Hackenberg, D.V. Edmonds, D.K. Matlock, F.C. Rizzo, K.D. Clarke, and E. De Moor, *Acta Materialia*, 2008, vol. 56, pp. 16-22

[6] M.J. Santofimia, L. Zhao, and J. Sietsma, *Met Trans A*, 2011, vol. 42A, pp.3620-3626

[7] E. De Moor, S. Lacroix, A.J. Clark, J. Penning, and J.G. Speer, *Met Trans A.*, 2008, Vol.39A, pp.2586-2595

[8] O. Grassel, G. Frommeyer, C. Derder, and H. Hofmann: J. Phys.IV France, 1997, vol. 7, pp. C5-383–88.

[9] D. M. Field, D.C. Van Aken, *Met Trans A.*, 2016 vol. 47A pp.1912-1917

[10] M. Acet, T. Schneider, B. Gehrmann, and E.F. Wasserman, *Journal De Physique*., 1995, Vol 5, pp. 379-384

[11] A. Holden, J.D. Bolton, and E.R. Petty, *Journal of Iron and Steel Inst.*, 1971, vol. 209, pp.721-728

[12] N.I Medvedeva, M.S Park, D.C. Van Aken, and J.E. Medvedeva, *J. Alloys Compd.*, 2014, vol. 582, pp. 475-482

[13] G.R. Speich, A.J. Schwoeble, and W.C. Leslie, *Met. Trans.*, 1972 vol. 3 pp. 2031-2037

[14] B.C. De Cooman and J.G. Speer, “Austenite Decomposition in Fe-C-X Alloy Systems,” *Fundamentals of Steel Product Physical Metallurgy*, 1st Edition, ASM International, Materials Park, OH, 2011, p. 173

[15] Z. Jicheng, and J. Zhanpeng, *Acta Metall. Mater.*, 1990, vol. 38, pp. 425-431

[16] V. Raghavan and D. Anita, *Metall. Mater. Trans A*, 1996, vol. 27A, pp. 1127-1132

[17] K.W. Andrews, *J. Iron Steel Inst.*, 1965, vol 203, pp. 721-727

[18] A. Stromvinter, A. Borgenstam, and J. Ågren, *Met. Trans. A*, 2012, vol. 43A pp. 3870-3879

[19] M. Palumbo, *Computer Coupling of Phase Diagram and Thermochemistry*, 2008, pp.693-708.

[20] S.T. Pisarik and D.C. Van Aken, *Met Trans A.*, 2016, vol. 47A pp1009-1018

[21] G.B. Olson and M. Cohen *Met Trans A*, 1976, vol. 7 pp. 1905-1914

[22] G.B. Olsen and M. Cohen *Met Trans A*, 1976, vol. 7 pp. 1897-1904

[23] M. Grujicic, G. B. Olson and W. S. Owen, *Metall. Trans A.*, 1985, vol. 16A, 1713

[24] L. Kaufman, and M. Cohen, *Progr. Metal. Phy*. 1958, vol. 7, pp. 165

[25] J.S. Bowles and A.J. Morton, *Acta Metall*., 1964, vol. 12, p.629

[26] J.F. Breedis and L. Kaufman, *Metall. Trans*., 1971, vol. 2, pp. 2359-2371

[27] Y.K.Lee and C.S.Choi, *Metall. Mater. Trans A*, 2000, vol. 31A, pp. 355-360

[28] S. Allain, J.P. Chateau, O. Bouaziz, S. Migot, and N. Guelton, *Mater. Sci. Eng. A*, 2004, vols. 387-389, pp. 158-162

[29] W.S. Yang, and C.M. Wan, *J. Mater. Sci.*, 1990, vol. 25, pp. 1821-1823

[30] S.T. Pisarik, MS thesis, Missouri University of Science and Technology 2014.

[31] L. Kaufman: *CALPHAD*, 1978, vol. 2, pp. 295-318.

[32] L. Kaufman: *CALPAHD*, 1979, vol. 3, pp. 45-76.

[33] L. Kaufman: *CALPHAD*, 1978, vol. 2, pp. 325-48.

[34] L. Kaufman: *CALPHAD*, 1978, vol. 2, pp. 117-46.

[35] A. T.Disndale SGTE Data for pure elements, *CALPHAD*, 1991, vol. 15, pp. 317-425.

[36] ASTM E 8/E 8M-08, Standard Test Methods for Tension Testing of Metallic Materials

[37] S. Martin, C. Ullrich, D. Simek, U. Martin, and D. Rafaja, *J. Appl. Crystallogr.*, 2011, vol. 44, pp. 779-787

[38] U.R. Lenel and B.R. Knott, *Met Trans A.*, 1987, vol. 18A, pp. 767-775

[39] M.C. Somani, D.A. Porter, L.P. Karjalainen, and R.D.K. Misra, *Met Trans A.*, 2014, vol. 45A, pp. 1247-1257

[40] K. Tsuzaki, S. Fukasaku, Y. Tomota, and T. Maki. *Mater Transaction*. 1991, vol. 32, pp. 222-228

[41] S. Cotes, M. Sade, and A. F. Guillermet, *Met Trans A.*, 1995, vol. 26A, pp. 1957-1969

[42] Q.X. Dai, X.N. Cheng, Y.T. Zhao, X.M. Lou, and Z.Z. Yuan *Mater. Characterization*, 2004, vol. 52, pp. 349-354

[43] S. Lee, and B.C. De Cooman, *Met Trans A.*, 2016, vol. 47A, pp. 3263-3270

[44] G.Ghosh and G.B. Olson, *Acta Materialia*, 2002, Vol. 50, pp. 2655-2675

[45] Takeuchi S. *J. Phys. Soc. Jpn.* 1969, Vol 27, 929

[46] G. Ghosh and G.B. Olson, *Acta Materialia*, 1993,Vol. 42, pp.3361-3370

[47] S. T. Pisarik, and D. C. Van Aken, *Met Trans A.*, 2014, vol. 45, pp. 3173-3178

[48] M. Atkins, “Atlas of continuous cooling transformation diagrams for engineering steels” ASM, (1980)

[49] E. Yang, H. Zurob, and J. McDermid, *Proc. of MS&T’10*, 2010 pp. 438-446

[50] J-C. Kim, D-W. Han, S-H. Baik, and Y-K Lee, *Mater. Sci. & Eng.*, 2004, vol. 378 pp. 323-327

[51] K.R. Limmer, J.E. Medvedeva, D.C. Van Aken, and N.I. Medvedeva *Computational Materials Science*, 2015, vol. 99, pp. 253-255

[52] P.R. Swann: *Corrosion*, 1963, vol. 19, p. 102.

[53] R.E. Schramm and R.P. Reed: Metall. Trans. A, 1975, vol. 6, p. 1345

[54] L.M. Kaputkina, V.G. Prokoshkina, and N.A. Krysina: Metals, 2001, vol. 6, p. 80.

[55] T. De Cock, C. Capdevila, F.G. Caballero, and C. Garcia de Andres, *Scripta Materiallia*, 2006, vol. 54 pp.949-954

[56] H.S. Yang, J.H. Jang, H.K.D.H. Bhadeshia, and D.W. Suh, *CALPHAD*, 2012, vol. 36, pp. 16-22

[57] J.H. Jun and C.S. Choi, *Mater. Sci. Eng. A* 1998, vol. 257, pp. 535-556

[58] S Takaki, H Nakatsu, and T Tokunaga: *Mater. Trans. JIM*, 1993, vol. 34, pp. 489–95.

[59] P.Y. Volosevich, V.N. Gridnev, and Y.N. Petrov: *Phys. Met. Metallogr.*, 1975, vol. 40, pp. 554–59.

II. DYNAMIC STRAIN AGING PHENOMENA AND TENSILE RESPONSE OF MEDIUM-MN TWO-STAGE TRIP STEEL

Daniel M. Field[a], D.C. Van Aken[b]

[a] Missouri University of Science and Technology
Department of Materials Science and Engineering, Rolla, MO 65409
Phone: 573-341-4804
e-mail: dfb52@mst.edu

[b] Missouri University of Science and Technology
Department of Materials Science and Engineering, Rolla, MO 65409
Phone: 573-341-4717
e-mail: dcva@mst.edu

Accepted to Metallurgical and Materials Transactions A, September 2017

ABSTRACT

Dynamic strain aging (DSA) and rapid work hardening are typical behaviors observed in two-stage TRIP steel. Three alloys with manganese ranging from 10.2 to 13.8 wt. pct. and calculated room temperature stacking fault energies varying from -2.1 to 0.7 mJ/m^2 were investigated. Significant serrations were observed in two of the steels and the addition of 4.6 wt. pct. chromium was effective in significantly reducing the occurrence of DSA in the third. Addition of chromium to the third alloy reduced DSA by precipitation of $M_{23}(C,N)_6$ during batch annealing at 873K (600 °C) for 20 hours. Three distinct DSA mechanisms were identified: one related to manganese ordering in stacking faults, with activation energies for the onset and termination of DSA being 145 kJ/mol and 277 kJ/mol. A second mechanism was associated with carbon diffusion in γ-austenite where Mn-C bonding added to the total binding energy, and a measured activation energies of 88 kJ/mol and 155 kJ/mol were measured for the onset and termination of DSA. A third mechanism was attributed to dislocation pinning and unpinning by nitrogen in α-ferrite with activation energies of 64 kJ/mol and 123 kJ/mol being identified. Tensile behaviors of the three medium manganese steels were studied in both the hot band and batch annealed after cold working conditions. Ultimate tensile strengths ranged from 1310 to 1404 MPa with total elongation of 24.1 to 34.1 pct. X-ray diffraction (XRD) was used to determine the transformation response of the steels using interrupted tensile tests at room temperature. All three of the processed steels showed evidence of two-stage transformation induced plasticity (TRIP) where γ-austenite first transformed to ε-martensite, and subsequently transformed to α-martensite.

I. INTRODUCTION

Medium manganese steels are of interest for automotive sheet steel, since they can be processed by cold working and intercritical or batch annealing. The resulting grain structures can be submicron with yield strengths in excess of 800 MPa as will be shown in this study. These medium manganese alloys are considered 3rd generation advanced high strength steel and the strengths ductility combination meet or exceed goals set by Department of Energy, defined as strengths of 1200-1500 MPa and associated total elongations of 30-25 pct. However, many of these steels exhibit static strain aging that is manifested by yield point behavior and yield point elongations that contribute to the overall total elongations [1-13]. Medium manganese steels can also be formulated to produce rapid work hardening as a result of two-stage TRIP, but many of these alloys exhibit dynamic strain aging and a reduced total elongation to failure, with failure occurring prior to necking.

A. Static Strain Aging

Yield point elongation (YPE), associated with static strain aging and the formation of Lüders bands is undesirable when forming complex automotive parts [14]. Inhomogeneous deformation associated with YPE are deleterious to press forming and leads to inconsistencies in the thickness of the final parts. Static strain aging is defined as an increase in yield and ultimate strengths, a decrease in the total elongation, and a time dependent return of the YPE or Lüders strain after plastic deformation [15,16]. Baird and Jamieson showed that the addition of N will have a strong effect on the occurrence of static strain aging in ferritic steels [17]. Many of the proposed 3rd generation advanced high strength steels that are medium manganese (5-10 wt. pct.) [2,3, 5-12] exhibit YPE, and it is noted that the degree of YPE can range from 2-10 pct. depending upon chemistry and processing prior to mechanical testing. Work by Suh et al. [3] on three Fe-0.5Si-5Mn-2Al (wt. pct.) alloys and varying carbon contents (0.06 - 0.11 wt. pct.) exhibited varying degrees of YPE based on heat treatment. They observed that an increase in heat treatment temperature from 933K (720 °C) to 1033 K (760 °C) lead to a change in YPE from 10 pct. to 4 pct. strain for all three alloys independent of carbon content. This significant change in the YPE was not noted by Suh et al., but is potentially attributed to the volume faction of α-ferrite/martensite in the starting structure. Specimens with 10 pct. YPE had more α-ferrite (87 vol. pct.) as compared to the 4 pct. YPE specimens (72 vol. pct.). Work by Han et al. [9] on a medium-Mn steel (8.5 wt. pct. Mn) showed an extensive yield point elongation (11 pct.) after cold working and intercritical annealing at 893K (620 °C), and this steel contained 63 vol. pct. α-ferrite/martensite in the starting structure.

B. Dynamic Strain Aging

An increased work hardening rate, negative strain rate dependence, and a serrated stress strain curve are often associated with DSA. It was noted by Horvath et al. [14] that the negative strain-rate dependence on ultimate tensile strength of the medium-Mn steels are a concern for the crash worthiness of potential future 3rd generation advanced high strength steels. For ferritic steels that show DSA Baird and Jamieson [17] attribute a reduction in the uniform elongation to exhaustion of interstitial solute that leads to a localized site of plastic flow and initiation of local necking. The dynamic interaction of dislocations and point defects during DSA occurs when dislocations are pinned by interstitials during plastic deformation causing a reduction in mobile dislocation density that results in an increase in flow stress as fewer dislocations must move faster to accommodate the imposed strain rate. Dislocation multiplication or subsequent unpinning at the higher stress will produce a transient drop in the flow stress, since more dislocations are mobile and move at a slower velocity to accommodate the imposed strain rate. Work by Rodriguez on DSA identified five unique forms of serrated flow observed in steel and are schematically shown in Figure 1 [18].

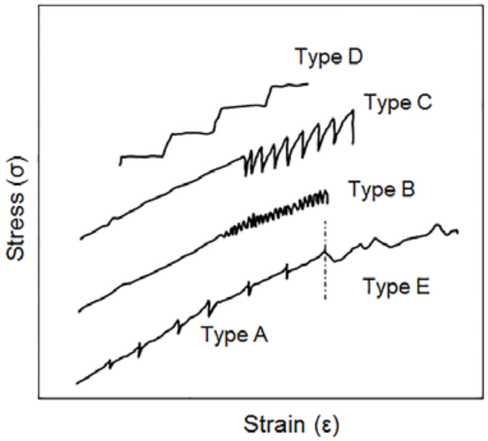

Fig. 1. The five types of serrated flow reported in literature. Type A where deformation bands initiate at the same end of the specimen and propagate in the same direction. Type B occurs due to discontinuous band propagation. Type C are yield drops due to dislocation unlocking and typically occurs at higher temperature. Type D are described as Lüders bands with no work hardening. Type E are Type A serrations at higher strains.

The most comprehensive work performed on DSA in medium manganese steel has been on Hadfield's manganese steel [19] and steels that exhibit twining induced plasticity (TWIP) [20]. Dastur and Leslie investigated the work hardening mechanism of a 0.2Si-11.4Mn-0.17Ni-0.16Cr-0.08Mo-1.13C-balFe (in wt. pct.) Hadfield's steel and argued that the work hardening behavior of Hadfield steels was related to dynamic strain aging and not twin formation. They determined the activation energy for the onset and termination of DSA to be 104 kJ/mol and 146 kJ/mol [19], and showed for the onset of DSA that the activation energy was below the activation energy for C diffusion in γ-austenite (~134 kJ/mol [19]). Lee et al. investigated the dynamic strain aging of two TWIP steels, one containing aluminum, 18Mn-1.5Al-0.6C-BalFe (wt. pct.), and the second being an Al-free 18Mn-0.6C-balFe (wt. pct.) steel. Both steels exhibited varying levels of DSA and an activation energy of 100 kJ/mol was determined by internal friction. Mössbauer spectroscopy was used to identify the defect complex responsible for pinning. From these results, they proposed that the mechanism was related to the diffusion of carbon, or a point defect complex, to the stacking fault region [20]. It is interesting to note that both investigations measured very similar activation energies; however, the measured energy value is well below the activation energy for diffusion of C (134 kJ/mol) in γ-Fe. The work by Balluffi [21] concluded that for diffusion within a dislocation core the required energy was 0.4 to 0.7 of bulk diffusion, and both sets [19, 20] of data are 0.75-0.77 of pure lattice diffusion of C in γ-austenite. Furthermore, Mn is expected to partition to the stacking fault lowering the fault energy and has been shown experimentally by the work of Kuzmina et al. [22] where Mn is segregated to the fault plane. Conversely C will increase the fault energy if at the fault plane. Work by Medvedeva et al. [23] showed by first principle calculations that Mn and C form a dipole along <100> in both bcc and fcc iron. According to Medvedeva et al. the presence of Mn forms a Mn-C pair that reduces the expected increase in the fault energy that is caused by C alone [24].

Dynamic strain aging is observed in many processed medium-Mn steels [4, 5, 7, 10, 12, 25]. Gibbs et al. [10] investigated a 7Mn steel annealed at temperatures varying from 848 to 948K (575 to 675 °C) for 168 hours. The investigated steel contained greater than 60 vol. pct. α-ferrite/martensite and the specimens examined exhibited either static, dynamic or both strain aging tensile responses. The 898K and 873K (625 °C and 600 °C) conditions exhibited both a DSA and YPE behavior, and both contained ≥ 67 vol. pct. α-ferrite/martensite in the starting structure. It is interesting to note in the 898K (625 °C) annealed condition there is a high work hardening rate ($n \approx 0.5$) as well as a Type B DSA tensile response. Gibbs et al. showed in XRD analysis that there was ε-martensite formation in the partially strained 898K annealed alloy's microstructure after 3.7 pct. strain. The 873K (600 °C) condition exhibits a reduced DSA response and a lower work hardening rate ($n \approx 0.4$); there is also an associated increase of the YPE by 2 pct. strain. The cause for the change in the DSA and YPE was not addressed by the authors; however, an increase in α-ferrite/martensite content in the starting structure is again a potential explanation. An alloy previously investigated by the authors [12] is a medium-Mn two-stage TRIP steel (11.5Mn-0.38Al-0.11C-2.46Si-0.029N-balFe.) that had significant serrations associated with DSA, a high work hardening rate ($n \approx 0.6$) and exhibited ε-martensite in the initial structure with 40 vol. pct. α-ferrite/martensite.

Many medium-Mn TRIP alloys contain significant levels (>100 ppm) of nitrogen [7, 12], which can also contribute to DSA. Zhang et al. [7] reports a medium-Mn steel with 120 ppm nitrogen that exhibited significant DSA at room temperature after varying degrees of intercritical warm working (0 – 77.5 pct. reduction in thickness) at 923K (650 °C). All of the reported specimens exhibit significant Type A and B serrations, and the authors note that the average strain hardening exponent is unchanged for all conditions (n ≈ 0.36). Zhang et al. stated that the steel in the warm worked condition all contain ~70 vol. pct. α-ferrite/martensite. The work by Shi et al. [4] studied four medium Mn alloys annealed at 923K (650 °C). All four of the alloys contain > 0.2 wt. pct. carbon and exhibit significant Type B serrations in the stress-strain data. Zhang et al. reports that the starting structure of the investigated steels are primarily α-ferrite (67 vol. pct.) with the remainder of the microstructure being γ-austenite. Work by Luo et al. [5] investigated two alloys at varying heat treatment temperatures, DSA was observed in the alloys heat treated to 943K (670 °C) and these steels contained roughly 88 vol. pct. α-ferrite. However, alloys heat treated at 923K (650 °C) do not exhibit any serrations and it was noted by TEM analysis that cementite was precipitated in these specimens.

II. MICROSTRUCTURAL FEATURES TO CONTROL DSA

Additions of carbides, nitrides or complex carbo-nitrides can be utilized to alter the DSA response of alloys. For ferritic grades of steel, the formation of a carbide can act as a sink for C and subsequently reduces the appearance of DSA [26-29]. Vankadesan et al. [30] observed that increasing the Ti: (C, N) ratio from 3.6 to 5.3 lead to an increase in the activation energy for the onset of DSA from 85 kJ/mol to 121 kJ/mol. The work of Cuddy and Leslie [31] showed that for ferritic steels containing 0.005 wt. pct. C the addition of 0.44 wt. pct. Ti lead to a higher temperature range at which DSA was observed. Cuddy and Leslie noted that the temperature range for DSA in Ti containing Fe-Ni alloys was 673K to 773K (400 to 500 °C). In the non-Ti bearing Fe-Ni steel, DSA was observed at a temperature range of 473 to 523K (200 to 250 °C) [31]. Baird and Jamieson [17] used wet hydrogen to remove nitrogen from non-Ti containing steel and the denitriding eliminated the DSA. Aluminum additions have also been shown to remove DSA in TWIP steels [31, 32] The effect of aluminum in TWIP steel is reported to be due to its effect on the intrinsic stacking fault (ISF) energy. Aluminum has been shown to increase the ISF by 11.3 mJ/m^2 with a 1.5 wt. pct. increase in aluminum [33] from transmission electron microscopy (TEM) measurements. The observed narrowing of the fault ribbon by Kim et al. [33] is assumed to reduce the interaction with the point defect complex leading to a loss of the dynamic pinning effect. A relationship of the activation energy for serrated yielding has been derived by McCormick [34] and Sleeswyk [35] from a static strain aging model as shown in eq. (1).

$$\varepsilon_C^{m+\beta} = \frac{\left[\frac{C_1}{\alpha C_0}\dot{\varepsilon} kTb \exp\left(\frac{Qm}{kT}\right)\right]}{3LN_d K_v U_m D_0} \tag{1}$$

where C_1 is the solute concentration at the dislocation needed to lock it, C_0 is the original solute concentration in the alloy, α is a constant, Q_m is the activation energy for solute migration, L is the obstacle spacing, U_m is the binding energy between solute and dislocation, D_0 is the diffusion coefficient, k is Boltzmann constant, T is temperature and b is the burgers vector. Parameters K_v, m, N_d and β are related to the strain dependency of vacancy concentration, $\dot{\varepsilon}$ is the strain rate, and ε_C is the critical strain where serrations occur. A reduction in C_0, where C_0 describes the solute in solution, such as nitrogen in ferrite, will lead to greater activation energy.

In the study presented here, the activation energy for onset and termination of DSA is studied in two Mn alloys; one predominately ferritic and one predominately austenitic. A third alloy being formulated to reduce the contribution of nitrogen to DSA by the precipitation of a carbo-nitride. Chromium was chosen, since it readily forms a carbo-nitride such as $Cr_{23}(C,N)_6$ and first principle calculations by Limmer et al. [36] show promising results with respect to the effect of Cr on the stacking fault energy; Cr lowers the unstable stacking fault (USF) energy 39 mJ/m^2 per 4 at. pct. Cr addition, and increases (less than most other alloy additions) the ISF. According to the first principles calculations, chromium increases the ISF by 14 mJ/m^2 per 4 at. pct. Chromium should therefore behave in a similar fashion to aluminum which adds 18 mJ/m^2 per 4 at. pct. Field et al. [37] showed that Cr has a similar effect on both the Ms^{ε} and Ms^{α} as compared to aluminum.

Formulation of the chromium bearing steel in this investigation was performed using the thermodynamic optimization software FactSage7.0^{TM} with the FSstel database. Figure 2 shows the phase stability for the Fe-0.15C-12Mn-1Si-4.5Cr-0.025N (wt. pct.) steel as a function of temperature. Precipitation of 2.8 wt. pct. $M_{23}(C,N)_6$ at equilibrium is predicted for a subcritical temperature (batch annealing) at 873 (600 °C).

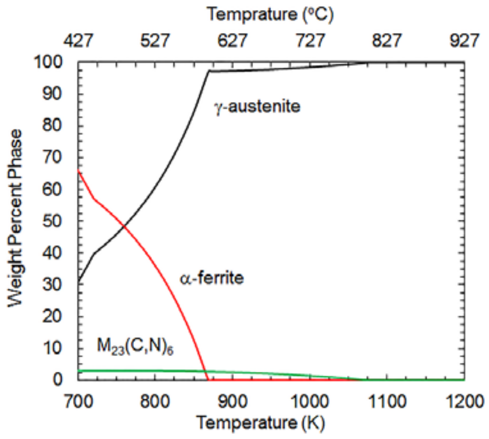

Fig. 2. Phase fraction as a function of temperature for a Fe-0.15C-12Mn-1Si-4.5Cr-0.025N steel.

III. EXPERIMENTAL PROCEDURE

Three alloys were used in this investigation and were produced by coreless induction melting of induction iron, ferrosilicon, electrolytic manganese, pure aluminum, ferrochrome, and carbon in the form of graphite. An argon cover gas was used to shield the melt and calcium wire additions were made to modify oxide inclusions and remove sulfur. Castings were poured into a ladle modified with a ceramic dam to force liquid from below the surface to form the pouring stream in a manner similar to a teapot. All alloys were cast with 150K (150 C°) superheat into phenolic no-bake sand molds to form a Y-block with dimensions measuring 12.6 x 6 x 1.7 cm^3. A Foseco KALPUR insulated riser with a diameter of 13.5 cm and height of 15.3 cm was attached to the upper Y-portion of the casting to act as a riser and ensure the soundness of the Y-block casting. Chemical analyses were obtained by inductively coupled plasma spectrometry after sample dissolution in hydrochloric and nitric acid. Carbon and nitrogen contents were determined by combustion using a LECO CS6000 and a LECO TC500, respectively. Alloy composition, stacking fault energy, and martensite start temperatures are listed in Table I for a fully austenitic and homogeneous alloy. Alloys are designated by the nominal Mn content of the steel. The martensite start temperatures were calculated according to the work of Pisarik and Van Aken [38] for ε-martensite, and Field et al. [37] for α-martensite. Stacking fault energy (ISF) was calculated according to the original work by Olson and Cohen [39] using eq. (2) with a value of n=2 for the planar fault thickness.

$$SFE(mJ/m^2) = n\rho(\Delta G^{\gamma\rightarrow\varepsilon}) + 2\sigma^{\gamma/\varepsilon} \qquad (2)$$

A regular solution model [38] was used to calculate the driving force for transformation, $\Delta G^{\gamma\rightarrow\varepsilon}$, Vegard's law was used to calculate the planar atomic density, ρ, of $\{111\}_\gamma$ and the interfacial energy between the γ-austenite and ε-martensite, $\sigma^{\gamma/\varepsilon}$, was held constant at 10 mJ/m^2. The start temperature for the ε-martensite was calculated by determining the temperature at which SFE = 0 mJ/m^2 for the case where n = 4 [38]. The M_S^α was calculated according to the work by Field et al. [37], where the strain energy of transformation, $\left(\Delta G_{Str}^{\gamma\rightarrow\alpha}\right)$ was balanced against the chemical driving force $\left(\Delta G_{Chem}^{\gamma\rightarrow\alpha}\right)$ according to eq. (3) and eq. (4)**.**

$$\Delta G_{str} + \Delta G_{chem}^{\gamma\rightarrow\alpha} = 0 \tag{3}$$

$$\Delta G_{str}(J/mol) = E\Omega\delta^2(14.8 - 0.13T) \tag{4}$$

where $\Delta G_{Str}^{\gamma\rightarrow\alpha}$ is calculated according to a modified regular solution model described by Field et al. [37]. Ω is the molar volume for iron of $7.15*10^{-6}$ (m^3/mol), δ is the lattice misfit between the γ-austenite and α-martensite with an approximate strain of $1.11*10^{-2}$ (m/m), T is the temperature in Kelvin and E is the modulus in units of Pa. The start temperature for the α-martensite was calculated by determining the temperature where eq. (3) is true. Negative stacking fault energies reported in Table I indicate that hexagonal iron is more stable than austenite at room temperature.

Steel castings were normalized at 1373K (1100 °C), held at temperature for 2 hours, and air-cooled to ambient 298K (25 °C). Castings were milled to an orthogonal prism of dimensions 15.5 x 125 x 50 mm^3 and hot rolled sequentially by heating to 1223K (950 °C), rolling, and reheating to 1223K (950 °C). This was repeated to obtain the desired hot band gauge of 2.5 mm, which accomplished a total hot reduction of 87.2 ± 6.8%. Samples exited the rolling mill at 1048 ± 15K (775 ± 15 °C) after the final roll pass and were air-cooled to room temperature. Hot band tensile properties were used to estimate the maximum cold work reductions possible prior to batch annealing. Steels were cold rolled using a Stanat TA 315 in a 4-high roll configuration to a reduction that equated to 2-3 times the elongation to failure of the hot-band materials. After cold rolling, the samples were placed in stainless steel bags containing gray iron machining chips and heated to 873K (600 °C) at an average rate of 15 °C/min, allowed to equilibrate, held for 20 hours, and cooled to 298K (25 °C) at an average rate of 4 K/min, and approximates a heating and cooling cycle for a commercial batch anneal.

Table I. Composition, calculated stacking fault energy and calculated start temperatures for ε and α martensites

Alloy	Composition (wt. pct.)						Calculated Parameters*		
	Mn	**Si**	**Al**	**Cr**	**C**	**N**	**SFE (mJ/m^2)**	**Ms$^{\varepsilon}$ K (°C)**	**Ms$^{\alpha}$ K (°C)**
14Mn	13.8	2.01	0.40	-	0.10	0.028	-2.1	405 (132)	381 (108)
12Mn	11.9	1.2	-	4.6	0.17	0.042	0.7	365 (92)	475 (202)
10Mn	10.2	2.38	0.30	-	0.17	0.024	-0.2	387 (114)	417 (144)

**Calculated values assumed a homogeneous, single-phase austenite*

Tensile tests were performed in accordance with ASTM E8 using standard tensile bars having a gage length of 50 mm and gage width of 12.5 mm. All test specimens were mill-cut parallel to the rolling direction from both the hot-band and batch-annealed material [40]. Interrupted tensile tests were conducted at room temperature in displacement control at a rate of 0.01 mm/sec using a 245 kN servo-hydraulic test frame. Strain was continuously measured to failure using a noncontact laser extensometer. A non-standard tensile bar was used for the DSA studies as shown in Figure 3 with dimensions in mm and tensile axis parallel to the rolling direction. Test samples were cut by electro-discharge machining from the batch-annealed material. Activation energies for dynamic strain aging were determined by performing tensile tests at different strain rates, $(\dot{\varepsilon})$, ranging from 10^{-4} to 10^{-2} sec^{-1} using a 95 kN servo-hydraulic test frame equipped with a temperature controlled environmental chamber with test temperatures ranging from 248 to 673K (-25 to 400 °C). Specimen strain was measured visually through a glass window in the environmental cell using the non-contact laser extensometer. Heating and cooling of the samples was performed at a constant 20 K/sec to the target temperature and the sample was held at temperature for 10 minutes to equilibrate prior to testing. Tests were performed in displacement control to obtain the desired strain rate and the actual strain rate was calculated from the laser extensometer displacement data.

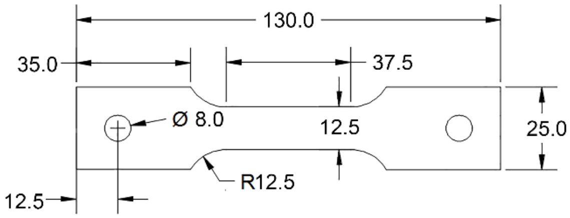

Fig. 3. Sample geometry of the DSA tensile bars with dimensions shown in millimeters.

X-ray diffraction (XRD) specimens were obtained from interrupted tensile tests for both hot-band and batch-annealed conditions at varying degrees of strain to investigate the TRIP character of the material. XRD specimens were mechanically polished to 0.1 μm using diamond paste in the Longitudinal-Transverse plane, (polished surface parallel to the rolling plane). Diffraction patterns were obtained using a Phillips X-pert diffractometer using a Ni filtered Cu Kα radiation source and equipped with a flat graphite monochromator. Phase quantifications, including ε-martensite, were calculated utilizing the Rietveld refinement method described by Martin et al. [41] for an Fe-16Cr-6.8Mn-6.1Ni steel, but modified accordingly for the steel chemistries investigated in this study. Polished samples (1.0 mm in thickness) were mounted on to a platinum heating strip and elevated temperature XRD scans were performed by heating at a rate of 20 K/sec to the target test temperature. Once the target temperature was obtained samples were held at temperature for 10 minutes to equilibrate and scanned from 30-90°. Argon cover gas was used to prevent oxidation of the samples.

Final polishing of EBSD samples was performed with a 0.02 μm colloidal silica solution using a vibratory polisher and examined in the Longitudinal-Short plane (perpendicular to both the rolling plane normal and the rolling direction). Orientation image mapping via pattern analysis was performed using a Helios NanoLab 600 equipped with a Nordlys detector and the AZTEC software package. The electron beam was operated at an accelerating voltage of 20.0 kV and emission currents of 5.5 to 11 nA. Electron dispersive spectrometry (EDS) mapping was conducted simultaneously to the EBSD mapping using a lithium drifted silicon detector with the same working parameters for the EBSD mapping. Orientation image maps and diffraction patterns were tilt corrected.

IV. RESULTS

A. Microstructure

EBSD-OIM and EDS mapping were used to determine qualitatively the microstructural features of the as-processed and partially strained alloys. Hot band EBSD images are shown in Figure 4. All three hot band microstructures were comprised of γ-austenite, ε-martensite, and α-martensite. The microstructure of the 10Mn steel after batch annealing is shown in Figure 5. An average grain size of 0.34 ± 0.01 (95% CL) μm was measured using the band contrast map shown in Figure 5(a). Phase identification is shown in Figure 5(b) and a primarily α-ferrite microstructure was produced by batch annealing with a minor fraction of γ-austenite containing some ε-martensite.

Less α-ferrite was produced during batch-annealing of the 14-Mn alloy as shown in Figure 6. The grain size was also bimodal with alloy rich regions being austenitic (average grain diameter of 3.0 ± 0.3 μm) and alloy lean regions being a mixture of α-ferrite and γ-austenite with an average grain diameter of 1.1 ± 0.4 μm. Both athermal ε-martensite and α-martensite are observed in the γ-austenite of the 14Mn alloy see Figure 6(a). Athermal α-martensite was differentiated from α-ferrite by noting that α-ferrite formed during batch annealing was equiaxed and depleted in Mn as revealed by the complimentary elemental mapping of Mn shown in Figure 6(b). When present, the athermal martensite was contained in bands of ε-martensite.

The grain structure of the chromium modified 12Mn alloy is similar to the 10Mn alloy and an average grain size of 0.67 ± 0.02 μm was measured from the band contrast map shown in Figure 7(a); phase identification by EBSD of α-ferrite, γ-austenite and athermal ε-martensite is shown in Figure 7(b). Phase fractions as determined using XRD of the hot band and the batch annealed steels are shown in Table II. From the phase fractions of the α-ferrite measured using XRD and the measured Mn content according to the EDS analysis a composition of the γ-austenite and α-ferrite are shown in Table III, concentrations of C and N are determined according to complete partitioning and equilibrium may not have been reached. As a result, the extensive partitioning to γ-austenite of carbon and nitrogen may not be fully attained since non-equilibrium distribution of the substitutional alloys will affect the activity of both carbon and nitrogen distributions. The Ms temperatures of the γ-austenite are recalculated according to the measured EDS data; however the manganese content of the 14Mn alloy γ-austenite is outside of the range for the Ms^{α} model derived by Field et al. [37]. For the Cr-modified 12Mn alloy an equilibrium amount of 2.8 wt. pct. $M_{23}(C,N)_6$ is assumed to be present in the microstructure and its effect on denuding the γ-austenite of C is shown. FactSage was also utilized to compare the software prediction to the measured composition of the phases. It should be noted that the measured Mn content of the α-ferrite is higher for all alloys compared to FactSage's predicted composition of ~4 wt. pct. Mn; and this leads to the lower measured Mn content in the γ-austenite grains compared to the calculated amount of Mn in the calculated γ-austenite composition.

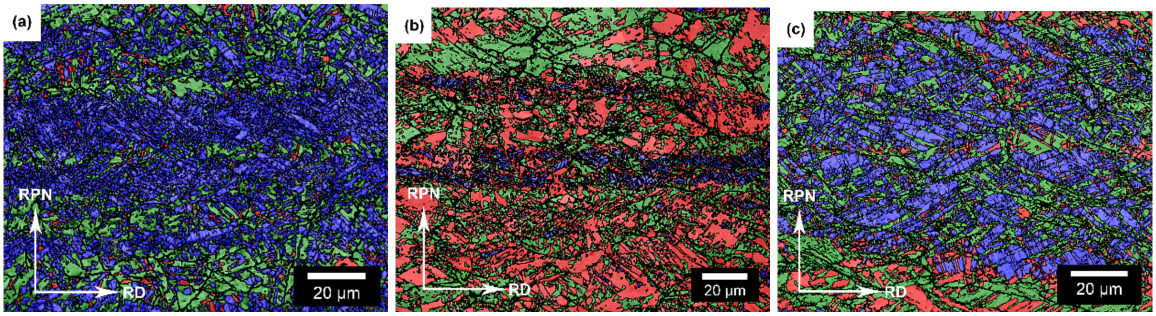

Fig. 4. EBSD-OIM images of the unstrained hot band (a) 10Mn, (b) 12Mn, and (c) 14Mn alloys. Where γ-austenite is shown as green, ε-martensite is red, and α-ferrite is blue.

Table II. Volume fraction of phases for the three alloys investigated in the hot band, and cold worked and annealed conditions values obtained according to XRD

Alloy	**Hot Band**			**Cold Worked and Annealed**		
	γ	**ε**	**α**	**γ**	**ε**	**α**
14Mn	14	45	41	67	14	19
12Mn	23	51	26	37	33	30
10Mn	20	26	54	32	10	58

Table III. Composition of the phases of interest in wt. pct. using EDS and a 95% CL standard deviation. FactSage calculated values are also shown for comparison.

		γ–austenite					α–ferrite				
		C	N	Mn	Ms^{ε} K (°C)	Ms^{α} K (°C)	C	Mn	Cr	Al	N
10Mn	EDS	0.36*	0.081*	12.3±3	340 (67)	421 (148)	0.02*	9.0±3.3	-	0.3±0.2	0.1*
	FactSage	0.38	0.058	18.6			<0.001	3.82	-	0.51	<0.01
12Mn	EDS	0.006*	0.004*	14.6±2	404 (131)	439 (166)	0.02*	11.5±3.0	3.8±0.8	-	0.1*
	FactSage	0.007	0.001	15.1			<0.001	3.92	2.16	-	<0.01
14Mn	EDS	0.11*	0.011*	15.9±3	376 (103)	-	0.02*	10.9±3.8	-	0.4±0.1	0.1*
	FactSage	0.12	0.054	17.3			<0.001	4.1	-	0.52	<0.01

** Values of carbon and nitrogen reported were calculated assuming full partitioning*

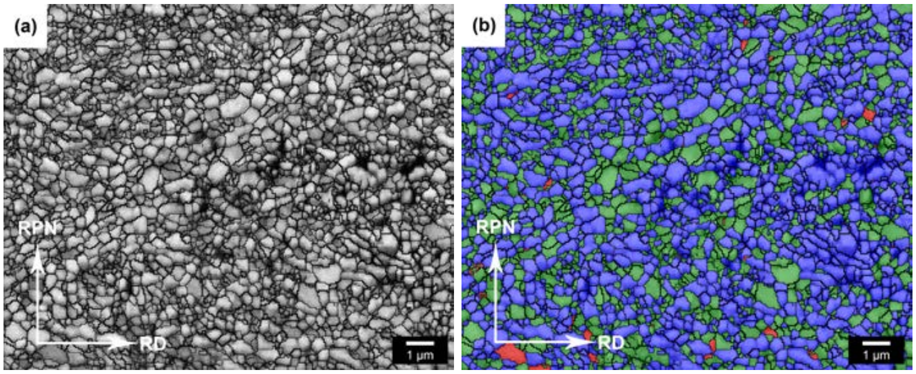

Fig. 5. (a) Band contrast map of the batch annealed 10Mn steel, and (b) Phase map of the unstrained 10Mn alloy after batch annealing where γ-austenite (green) ε-martensite (red) and α-ferrite (blue)

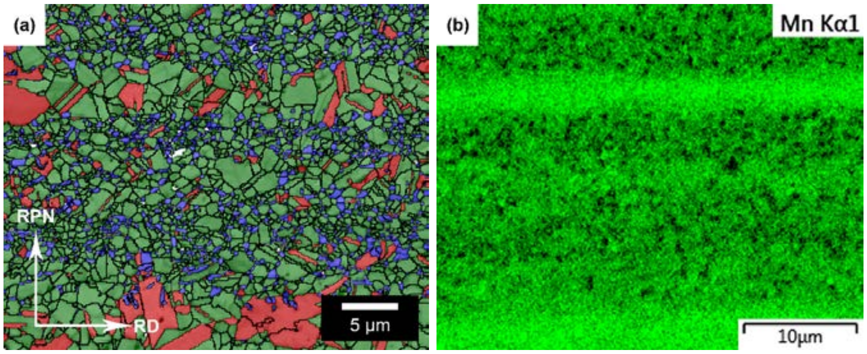

Fig. 6. (a)EBSD-OIM map of the cold worked and annealed 14Mn alloy which depicts the equiaxed γ-austenite (green) ε-martensite (red) and α-ferrite/martensite (blue), and (b) compositional map of manganese concentration.

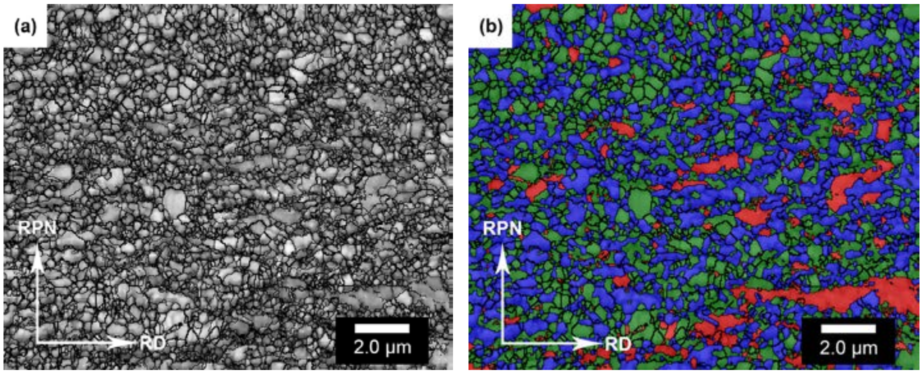

Fig. 7. (a) Band contrast map of the batch annealed 12Mn steel, and (b) Phase map of the unstrained 12Mn alloy after batch annealing where γ-austenite (green) ε-martensite (red) and α-ferrite (blue)

B. Tensile Behavior

Stress-strain plots of hot-band and batch-annealed steels are shown in Figure 8(a) and 8(b), with a summary of the tensile properties given in Table IV. All three alloys in the hot-band condition show a continuous work hardening behavior with no evidence of yield point elongation. Post necking plastic strain was observed in the 10Mn and 14Mn alloys whereas the 12Mn alloy failed prior to the onset of necking. Serrated flow indicating dynamic strain aging was observed in the hot-band stress-strain data of the12Mn and 14Mn alloys. Yield point and yield point elongation were observed after cold working and batch annealing; both the 10Mn and 14Mn alloys exhibit Type B serrations whereas the Cr bearing 12Mn alloy has a reduced occurrence of DSA and appears to exhibit Type A/E serrations that occur at higher strain levels. If the yield point elongation is subtracted from the 10Mn alloy, the failure strain for all three alloys is approximately 25% in the batch-annealed condition.

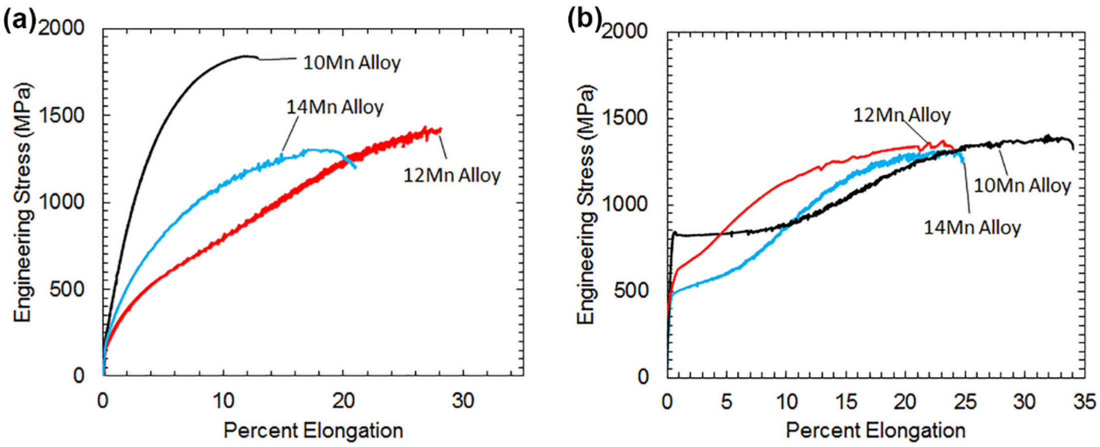

Fig. 8. Stress-strain graph of the (a) hot band and (b) batch annealed steels

Table IV. Mechanical properties of the hot band and processed steel, tested at room temperature (298K, 25 °C)

Alloy	**Hot Band**					**Cold Work (%)**	**Cold Worked and Annealed**				
	YS (MPa)	**UTS (MPa)**	**e_f (%)**	**K (MPa)**	**n**		**YS (MPa)**	**UTS (MPa)**	**e_f (%)**	**K (MPa)**	**n**
14Mn	240	1304	21.0	4220	0.51	53.6	500	1316	24.8	6810	0.81
12Mn	190	1436	28.1	5700	0.78	55.1	650	1310	25.0	3370	0.33
10Mn	260	1841	12.9	8750	0.59	35.6	837	1404	34.1	4920	0.70

Interrupted tensile tests followed by quantitative XRD were performed on both the hot band and the batch annealed steels to determine the TRIP behavior of the steels. Volume fraction of the three crystal structures (γ-austenite, ε-martensite, and α-martensite/ferrite) as a function of total strain is shown in Figure 9(a-f) for the three alloys in both hot-band and batch-annealed conditions. The only hot-band alloy that exhibits the two-stage TRIP behavior is the 14Mn steel and the behavior is similar to that reported by McGrath et al. [13] where γ-austenite first transforms to ε-martensite until saturation and subsequently to α-martensite. In contrast, an initial ε→α transformation is observed in the hot band 10Mn alloy, see Figure 9(a), and once the athermal ε-martensite is consumed the γ-austenite transforms to ε-martensite. This phenomenon in transformation response is considered to be a material property and not a sample variation artifact. This is demonstrated by overlaying the stress-strain curve of each specimen tested to varying total strains as shown in Figure 10, where each unloading curve is a separate specimen that was used to quantify the strained microstructure using XRD.

After cold working and annealing all three steels exhibit a similar two-stage TRIP response with γ-austenite first transforming to ε-martensite and ε-martensite transforming subsequently to α-martensite. It is shown in Figure 11(a) of the 12% strained 14Mn alloy that the α-martensite which forms is confined to prior ε-martensite bands. The Stage I→II transition strain was consistent for all three alloys up to approximately 5 pct. strain.

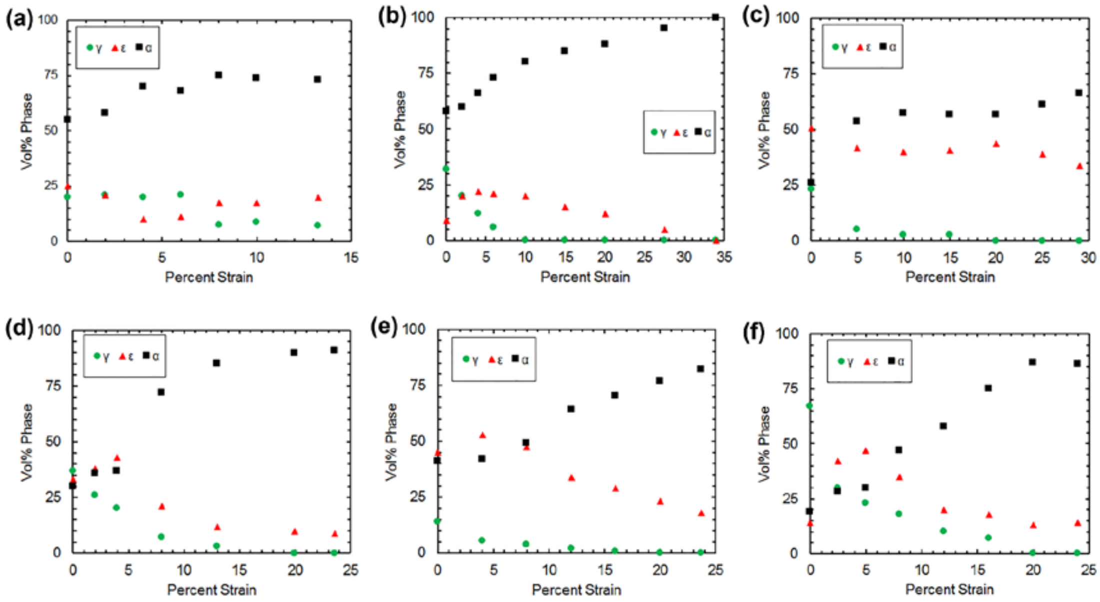

Fig. 9. Volume faction of the phases as a function of strain. For the 10Mn alloy in the (a) hot band and (b) annealed conditions. The chromium modified 12Mn alloy in the (c) hot band and (d) annealed condition, and the 14Mn alloy in the (e) hot band and (f) annealed condition.

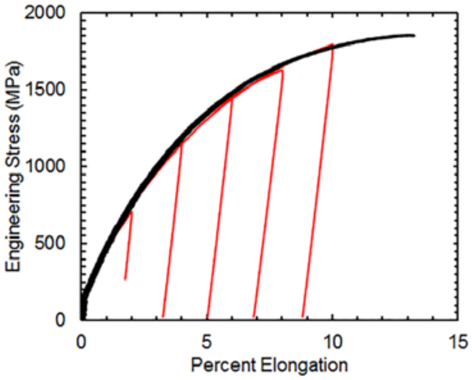

Fig. 10. Stress-strain curves of the 10Mn hot band alloy for the six samples tested to varying total strains used to determine the transformation response as a function of strain.

Figure 11(b) shows orientation image map of the α-phase, and the adjacent α-martensite plates that formed during Stage II transformation and the α-martensite plates appear to be twin related according to their orientation (highlighted with arrows in Fig. 11(b)) as has been shown by Pisarik and Van Aken for athermal transformations [42] as well as Kinney et al [43] for the athermal reaction.

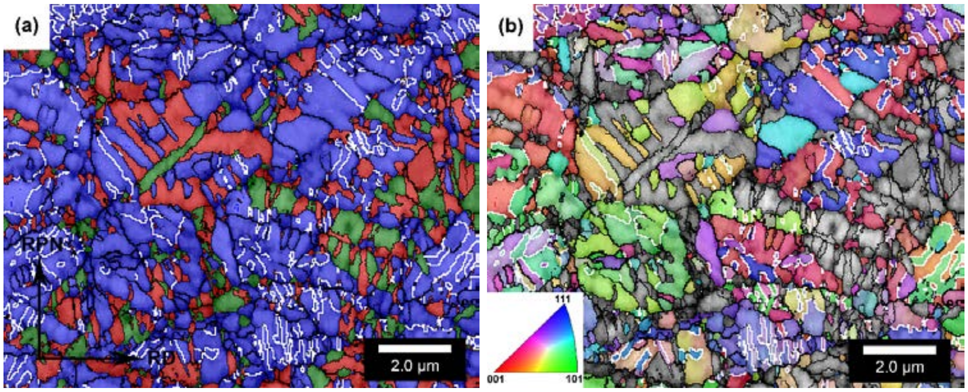

Fig. 11. (a) Phase map of the 12% strained 14Mn alloy γ-austenite (green) ε-martensite (red) and α-ferrite/martensite (blue) and (b) the orientation image map of the bcc structure with the orientation relative to the rolling direction (x-axis). White arrows are used to highligh twin related α-martensite variants.

C. Dynamic Strain Aging and Activation Energy

Activation energies for the onset and termination of DSA were determined using tensile tests performed at varying strain rates $(\dot{\varepsilon})$ and temperatures (T). Dynamic strain aging was characterized for the serrations that occurred during the Stage II (ε→α) tensile response. This is best exemplified in Figure 12 comparing two samples of 10Mn tested at strain rates of 10^{-2} and 10^{-4} s^{-1}, at 573K (300 °C). Two work hardening rates are observed for the specimens tested at a 10^{-4} s^{-1}, with the initial portion of the stress-strain curve exhibiting Lüders-like strain; however, unlike Lüders strain or yield point elongation observed in plain carbon steels the results in Figure 12 show strain hardening. Once these Lüders-type serrations are exhausted a secondary work hardening rate with no DSA occurs with a strain rate of 10^{-4} s^{-1} at 573K (300 °C) and this test result is classified as a non-DSA sample for this analysis. Figure 12(b) shows a magnified portion of the Stage II work hardening with and without DSA. Noise in the non-DSA work hardening curve (10^{-4} s^{-1} at 573K) is typical baseline for the laser extensometer. This classification methodology was carried out for all test temperatures and strain rates. Activation energies were determined from graphs of the $\ln(\dot{\varepsilon})$ vs. 1000/T (with temperature in Kelvin) noting when DSA occurred. A dynamic strain aging map is shown for the 10Mn steel in Figure 13(a) with an activation energy for DSA initiation measured to be 64 ± 6 kJ/mol, and the activation energy for DSA termination was 123 ± 12 kJ/mol. From the DSA map of the Cr modified 12Mn alloy in Figure 13(b) the onset of DSA is measured as 145 ± 15 kJ/mol, and termination energy is 277 ± 8 kJ/mol. From Figure 13(c) the 14Mn steel; activation energy for DSA initiation is 88 ± 15 kJ/mol and the termination energy for the 14Mn alloy is measured to be 155 ± 5 kJ/mol.

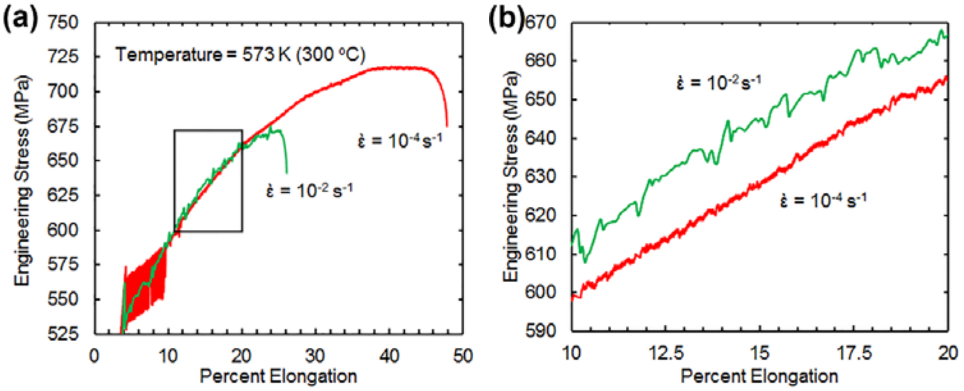

Fig. 12. (a) Comparison of the engineering stress-strain curve of the 10Mn alloy at 573K (300 °C) (b) detailed view in the range of 12 to 20 pct. strain illustrating the similarity in the work hardening rate within and outside the DSA region. The $\dot{\epsilon} = 10^{-2}\ s^{-1}$ exhibits DSA with a work hardening rate 1540 MPa and strain hardening exponent of n = 0.35. The $\dot{\epsilon} = 10^{-4}\ s^{-1}$sample does not exhibit DSA and has a work hardening rate of 1505 MPa and a strain hardening exponent of n = 0.33.

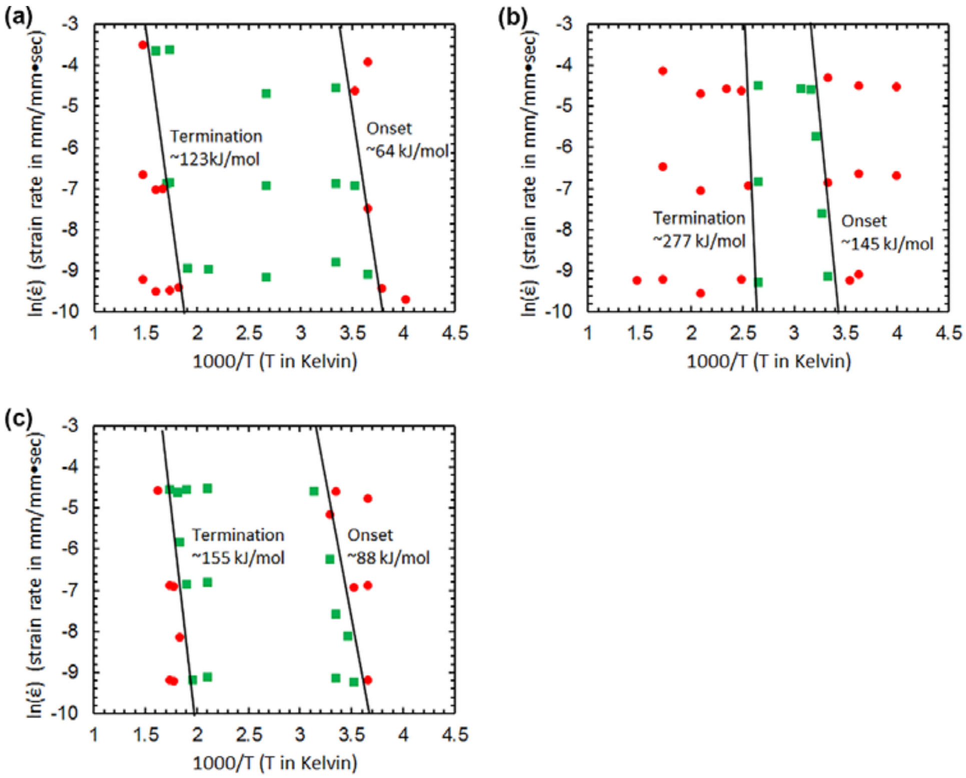

Fig. 13. DSA map of the (a) 10Mn alloy, (b) 12Mn alloy, and (c) 14Mn alloy. Circles denote samples which did not exhibit DSA during tensile testing and squares denote samples that did exhibit the typical serrated flow associated with DSA.

XRD phase fractions at elevated temperatures of the processed steels are shown in Figure 14(a-c). The authors however wish to stress that the transformation response upon straining is only known for room temperature samples. DSA transition regions are highlighted with gray bands for both the low temperature initiation and elevated temperature termination. Phase quantifications for tensile tests above ambient temperature (> 298 K) were performed using a heating stage equipped diffractometer. A cooling stage was not available for phase identification at lower temperatures. It is noted that for the 10Mn alloy the termination zone of DSA is observed to occur when the γ-austenite and α-ferrite becomes an even distribution of phases. The Cr-modified 12Mn steel contains the greatest volume fraction of ε-martensite in the starting structure and is observed that there is little change to the microstructural constituents for both the initiation and termination region of the DSA response. The 14Mn alloy contains the greatest volume fraction of γ-austenite and the termination of serrations does not occur until ε-martensite reversion occurs.

To confirm the efficacy of the annealing cycle and the precipitation of the carbo-nitride, a 12Mn sample was re-austenitized at 1123K (850 °C) within a single-phase field according to the results presented in Figure 2. The specimen was held at temperature for 1 hour to fully dissolve the carbo-nitrides and quenched to room temperature. Room temperature tensile tests at a strain rate of 10^{-4} sec^{-1} produces DSA. A comparison of the XRD scans for both the batch annealed and austenitized and water quenched samples are shown in Figure 16. A carbide peak is observed for the (020), labeled as $\underline{C}$ in the XRD spectrum, only in the annealed sample. After austenitization and water quenching the carbide peak is no longer observed.

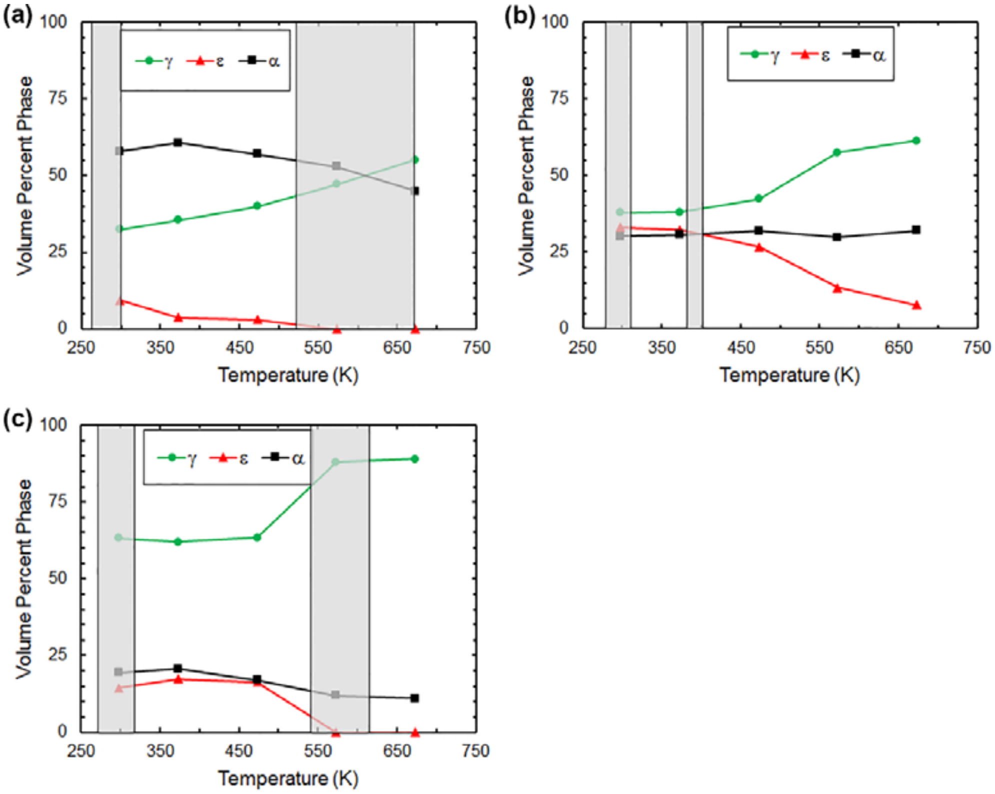

Fig. 14. Volume fraction phase as a function of temperature for the (a) 10Mn, (b) 12Mn, and (c) 14Mn alloys. The DSA transition regions are highlighted within the gray bands.

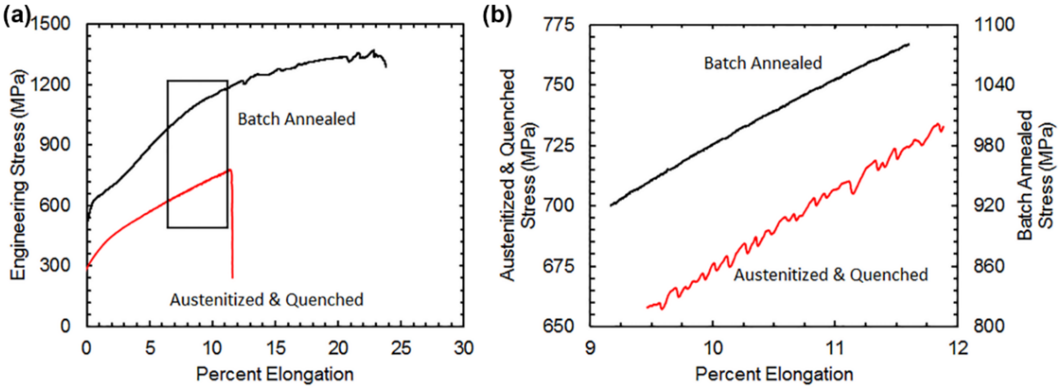

Fig. 15. (a) Stress-strain of the austenitized and quenched and the batch annealed 12Mn alloy, and (b) detailed view of both tensile curved at strains of 9 to 12 pct., it should be noted the stress-axis are adjusted to magnify both tensile responses

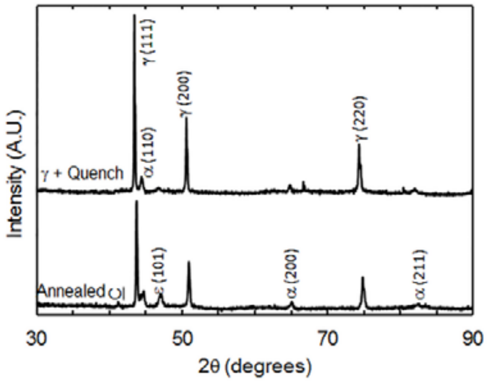

Fig. 16. XRD scans of the batch annealed and the austenitized and quenched samples. Peak locations are identified to the crystal structure and the carbide peak is labeled as C

V. DISCUSSION

Multiple dynamic strain aging mechanisms are possible as evidenced by the results obtained in this study where onset and termination activation energies for the three alloys studied vary 64 to 145 kJ/mole and 123 to 277 kJ/mole, respectively. Analysis of the onset and termination energies are also complicated by the fact that in two of the alloys (10Mn and 14Mn) the relative portions of the various phases change in the DSA active test range of temperature and strain rate. There is also the possibility that two or more DSA mechanisms may overlap during either the onset or the termination. However, in two of the alloys (12Mn and 14Mn) a clear case can be made to propose a single mechanism.

For the Cr modified 12Mn alloy it is observed that the onset of DSA occurs at higher temperatures for all strain rates compared to the 10Mn and 14Mn alloy. An activation energy for DSA of 145 ± 14 kJ/mol is reported in Figure 13(b). This value is greater than the activation energy of 134 kJ/mol reported for carbon diffusion in γ-austenite [44]. It might also be possible to discount any mechanism associated with either nitrogen or carbon interstitials based upon the calculated concentration of those elements in equilibrium with $M_{23}(C,N)_6$ as shown in Table III. Solubility of nitrogen and carbon in γ-austenite at the batch annealing temperature was 10 and 70 ppm, respectively. The effectiveness of the $M_{23}(C,N)_6$ in reducing the interstitial contribution was also demonstrated by heating the alloy above the solvus temperature of the carbo-nitride, quenching, and testing in the fully austenitic condition as shown in Figure 15.

The onset activation energy is also well above that measured for DSA by Venkadesan et al. [30] in titanium treated austenititic stainless steels where a 42 pct. increase in the activation energy for the onset of DSA was measured for the steel containing a higher titanium content. The low titanium (0.21 wt. pct.) stainless steel had an activation energy of 85 kJ/mol while the higher Ti steel (0.32 wt. pct.) had a measured activation energy of 121 kJ/mol. Both values are less than the activation energy for carbon diffusion in γ-austenite. In addition, Venkadesan et al. reports no measured difference in the termination energy (180 ± 8 kJ/mol) for DSA despite an increase in titanium content. This would imply that the cause of the DSA was still related to interstitials in solution, and the change in initiation energy is indicative of the reduced concentration of C, and N resulting from Ti(C,N) precipitation and shown mathematically in eq (1). In a similar fashion Choudhary et al. [29] reports the efficacy of an annealing treatment to a 9Cr-1Mo ferritic steel to precipitate and coarsen Cr-carbides and nitrides. Choudhary et al. found that by coarsening the carbides and nitrides the magnitude of serrations was reduced and the critical strain for DSA was increased.

The termination energy of 277 ± 8 kJ/mol measured for the 12Mn alloy is well above that reported for DSA mechanisms associated with interstitials in austenite.

However, this activation energy is very close to the reported activation energy for lattice diffusion of Mn in austenite 276 kJ/mol. [45] As proposed by Balluffi [21] the activation energy can range from 0.4 to 0.7 of bulk diffusion for pipe diffusion within a dislocation core and the onset activation energy of 145 kJ/mol represents 0.52 of the lattice diffusion of Mn in γ-austenite [21]. It should also be noted that ε-martensite is stable throughout the region of DSA and at temperatures above where the termination energy of DSA was measured. The ε-martensite phase can be thought of as a series of intrinsic stacking faults bounded by partial dislocations. Thus, one possible mechanism might include a defect complex with Mn associated with the austenite and the ε-martensite interface. Interestingly, Medvedeva et al. [24] have shown that the ISF energy is lowered when Mn is situated at the fault plane. Work by Oi et al. [46] showed that the binding energy for the Mn interphase boundary pair is 8 kJ/mol. This would imply that the theoretical termination energy for DSA in the Cr modified 12Mn alloy should be 284 kJ/mol and for Mn being the controlling diffusing element for DSA, this is a 2.5 pct. difference from what was measured. Thus it may be concluded that the DSA observed in the 12Mn alloy is related to the interaction of Mn with the ε-martensite.

A mostly austenitic microstructure was obtained during the batch anneal of the 14Mn alloy as shown in Figure 6. The termination energy for DSA was measured in a temperature range greater than that observed for termination of DSA in the 12Mn alloy and at a temperature where ε-martensite had completely reverted to γ-austenite or nearly so as shown in Figure 14(c). Thus, no overlap in mechanism during termination is expected for a mechanism involving ε-martensite. Lower onset and termination energies of 88 ± 15 and 155 ± 5 kJ/mol also differentiate the DSA mechanism from the 12Mn alloy. Dastur and Leslie measured onset and termination energies for DSA observed in Hadfield manganese steel and reported energies of 104 and 146 kJ/mol with an uncertainty of 15 kJ/mol. The mechanism proposed was a complex defect with Mn and C paring close to the core of a dislocation. Using an activation energy for carbon diffusion in austenite (134 kJ/mol) and a binding energy of 8.2 kJ/mol for the Mn-C bond pair as reported by Medvedeva et al. [24] an activation energy for termination of 142 kJ/mol is predicted. This value is a close match for that reported by Dastur and Leslie and is 9 pct. lower than that measured for the 14Mn alloy. The onset activation energy is also reasonable and falls between that reported by Venkadesan et al. [30] for the low titanium modified stainless steel and that reported by Dastur and Leslie [19]. The measured onset energy of 88 ± 15 kJ/mol is 0.66 that of the activation energy for carbon diffusion in γ-iron (134 kJ/mol) suggesting that pipe diffusion of carbon along dislocations in austenite contributes to the lower activation energy for DSA than that observed in the 12Mn alloy. A second mechanism is proposed consistent with forming a dislocation-Mn-C complex defect in γ-austenite.

Yield point behavior and yield point elongation were observed in room temperature tensile tests of the 10Mn alloy. These observations would be typical of strain aging of ferritic steels associated with nitrogen. From Table II and Figure 14(a) the starting structure of the 10Mn alloy in the DSA initiation temperature range is 53–58 vol. pct. α-ferrite, with the remainder being ε-martensite and γ-austenite. At strains greater than 7 pct. where the onset activation energy was measured for DSA the microstructure is a combination of α-martensite, and ε-martensite as shown in Figure 9(b). An activation energy of 64 ± 6 kJ/mol was determined for the onset of DSA in the 10Mn alloy as shown in Figure 13(a). The observed activation energy is below that reported for carbon diffusion in pure α-iron (82 kJ/mol [44]); however, it is within 6 pct. of the activation energy for nitrogen diffusion in pure α-iron (68 kJ/mol) as reported by Wert and Zener [44]. The work by Baird and Jamieson [17] stated that DSA associated with nitrogen in α-ferrite was typically measured to be 63-84 kJ/mol for initiation and 146-209 kJ/mol for termination. The values reported in this work are a 1.5 pct. relative difference from what is shown for the measured initiation energy. However, if N diffusion in α-ferrite is the cause of DSA the dominant defects are therefore dislocations and a significant contribution to work-hardening from DSA might be expected; as shown in Figure 12 this is not the case and there is only a small increase (~2 pct.) in work hardening rate, and a 5 pct. increase in the work hardening exponent with DSA. The small difference in work hardening rate may be attributed to the low nitrogen content expected when α-ferrite is in equilibrium with γ-austenite as shown in Table III; as was noted earlier the concentrations reported in Table III may under estimate the N content of the α-ferrite.

A termination activation energy of 123 ± 12 kJ/mol was measured for DSA in the 10Mn alloy, and the termination energy is 16 pct. lower than what is reported from the work of Baird and Jamieson. [17] Within the temperature range of termination for the 10Mn alloy, the microstructure is an equal proportion of γ-austenite and α-ferrite as shown in Figure 14 (a). However, the results from the 14Mn alloy appear fairly conclusive that C in γ-austenite as a DSA mechanism for the 10Mn alloy must be excluded, since the termination energy is well below that of carbon diffusion in austenite. Furthermore, any solute-defect mechanism for DSA that might be suggested should also carry over into the results observed at higher strains. It might be argued that the very fine serrations observed in Figure 12 (b) are related to the C-Mn-defect mechanism proposed for the 14Mn alloy, since there is considerable overlap in the temperature range of termination. A smaller volume fraction of γ-austenite and a finer austenite grain size may indeed reduce the magnitude of the striations that might be observed. In comparing the DSA results of 12Mn to 10Mn the absence of ε-martensite, the low termination temperature range, and low termination energy for the 10Mn alloy lends credence to the proposed mechanism of Mn solute interacting with the defect structure of ε-martensite. It should also be noted at temperatures greater than 523K (250°C) there would be little driving force for Stage I (γ→ε) TRIP or standard TRIP (γ→α) in the 10Mn alloy and as shown in Table III where the athermal Ms temperatures for transforming the austenite to martensite are 482 K (128 °C) for the γ→α transformation and 340 K (67 °C) for the γ→ε transformation. At the test temperatures associated with termination all of the athermal ε-martensite has reverted to γ-austenite and this would suggest that the M_D for Stage I (γ→ε) TRIP or standard TRIP (γ→α) is at lower temperature. This latter point is rationalized by viewing the γ-austenite component only and noting that the γ-austenite finish temperature is above 573 K (300°C). However, this does not address the rather strong DSA observed at strains less than 10% as shown in Figure 12 (a). As noted above, these striations are not associated with any stress induced TRIP behavior and if they were, the DSA might be expected to extend to higher strains.

Two features of the DSA observed in the low strain regime of the 10Mn alloy must be addressed: a work hardening rate of approximately 160 MPa and a large oscillation amplitude that is greater than 30MPa. Both observations might be explained by the formation of mechanical twins in the austenite. A calculation of the ISF energy at

573 K (300°C) for the austenite chemistry yields 42.0 mJ/m^2 and this value is within a range that might be expected to produce twin induced plasticity or TWIP. It is generally accepted that Mn steels with an ISF energy ≥ 20 mJ/m^2 preferentially exhibits twin formation instead of martensitic transformation. A portion of the stress-strain response showing the detail of the serrations is shown in Figure 17. Initiation of the twining process occurs in a favorably oriented austenite grain and this would occur at a threshold stress for twin nucleation. Mechanical twins are capable of producing large strains and as a result of conducting the test in displacement or strain control the required load would drop precipitously until the twin extends across the austenite grain. The reader is again reminded that the γ-austenite grains are submicron and dispersed with ferrite grains. Thus, the TWIP may be restricted to a single twin within the grain and deformation of one γ-austenite grain may not sympathetically nucleate mechanical twins in local γ-austenite grains. A stress rise occurs as the first twin reaches a terminal length and the imposed displacement rate must be accommodated by dislocation plasticity until the next most favorably oriented austenite grain undergoes twin deformation. This process is repeated to ~10 pct. strain which appears to be the saturation point for twinning in this microstructure. The authors wish to reiterate that the systems investigated are extremely complex and there is much more investigation required to fully understand these medium-Mn steels. It may now be concluded that the DSA observed in the 10Mn alloy is associated with N in α-ferrite and that the higher termination energy measured by Baird and Jamieson [17] may be a combined mechanism of both carbon and nitrogen DSA occurring in a fully α-ferrite microstructure.

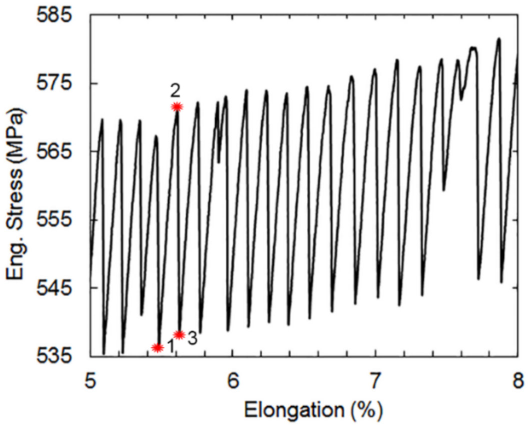

Fig. 17. The Lüders serrations from Figure 12(a) are shown in greater detail.

Also reported in this study are tensile properties for hot band and intercritically annealed materials having first been cold worked. The 14Mn alloy is the only hot-band steel investigated that exhibits a strain induced transformation sequence within the criteria of a typical two-stage TRIP response as reported in literature [13]. There is an initial increase in ε-martensite associated with the γ→ε Stage I transformation occurring at low strains (≤ 4 pct.) and once the system is saturated with ε-martensite and all of the γ-austenite is consumed, Stage II ε→α, transformation occurs to failure as shown in Figure 9. The strain levels associated with the transition of Stage I to Stage II are consistent with the works described by both Shin et al [47] and Huang et al. [48] from their works on ferrous shape memory alloys that contain ε-martensite. It was shown that beyond 4 pct. strain the deformation was unrecoverable due to the formation of α-martensite from the intersection of ε-martensite bands. From Figures 8 and 9 it can be seen that the initial low work hardening region is associated with the first martensitic transformation of γ-austenite to ε-martensite. The elevated work hardening portion of the stress-strain graph is shown from the XRD results to be the second martensitic transformation of ε-martensite to α-martensite and exhibits an average work hardening rates > 3300 MPa.

VI. CONCLUSION

The Cr modified 12Mn alloy was found to be a two-stage TRIP steel with a significantly reduced DSA response during tensile testing. The reduction in DSA was attributed to the formation of $M_{23}(C,N)_6$. The Cr modified 12Mn alloy had a significantly higher activation energy for the onset of DSA which was measured to be 145 ±14 kJ/mol; and DSA in the 12Mn alloy was related to Mn positioning within the defect structure of ε-martensite based upon the termination energy, 277 ± 8 kJ/mol. The DSA mechanism in the 14Mn is differentiated from the 12Mn steel and is attributed to C diffusion in γ-austenite with the added binding energy for the dislocation-Mn-C bond pairing. The activation energy and termination energies for DSA in the 10Mn steel was found to be interstitial nitrogen trapping at dislocations within the α-ferrite. However, no significant increase in work hardening rate was observed when DSA was activated. The 14Mn steel, was the only alloy in the hot band condition that exhibited the two-stage TRIP phenomenon. After batch annealing at 873 K (600 °C) for 20 hours all three investigated steels demonstrate a two-stage TRIP behavior. This is observed by an initial saturation of the system with ε-martensite by consuming some of the retained γ-austenite, and concludes with the formation of α-martensite from the transformation of $\varepsilon \rightarrow \alpha$.

ACKNOWLEDGEMENTS

This work was supported by the Peaslee Steel Manufacturing Research Center (PSMRC). Companies directly involved in this work include AK Steel, ArcelorMittal, Nucor Steel, and U. S. Steel. The FEI Helios NanoLab dual beam FIB was obtained with a Major Research Instrumentation grant from the National Science Foundation under contract DMR-0723128. The authors also acknowledge the support of the Materials Research Center and in particular Dr. Clarissa Wisner and Dr. Jingjing Qing for guidance and training on the SEM as well as Dr. Eric Bohannan for performing the XRD work. Special thanks are also extended to Dr. Narayan Pottore and Dr. Shrikant Bhat at ArcelorMittal for their discussions on DSA mechanisms.

REFERENCES

[1] T. Tschiyama, T. Inoe, J. Tobata, D. Akami, and S. Takaki, *Scripta Mat.* 2016, vol. 122, pp. 36-39

[2] D-W. Suh, S-J Park, T-H. Lee, C-S. Oh, and S-J. Kim, *Met Trans A*, 2010, vol. 41A, pp. 397-408

[3] D-W. Suh, J-H Ryu, M-S. Joo, H-S Yang, H.K.D.H. Bhadeshia, *Met Trans A*, 2013, vol. 44A, pp. 286-293

[4] J. Shi, X. Sun, M. Wang, W. Hui, H. Dong, and W. Cao, *Scripta Mat*, 2010, vol. 63, pp. 815-818

[5] H. Luo, H. Dong, and M. Huang, *Mater. & Design*, 2015, vol. 83, pp.42-48

[6] S. Lee, S-J. Lee, S. Santhosh Kumar, K. Lee, and B.C. De Cooman, *Met Trans A*, 2011, vol. 42A, pp. 3638-3651

[7] Y. Zhang, L. Wang, K. O. Findley, and J. Speer, *Met Trans. A*, 2017, vol. 48A, pp. 2140-2149

[8] J. Han, S-H. Kang, S-J. Lee, and Y-K Lee, *Jour. Alloy & Compound.* 2016, vol. 681, pp. 580-588

[9] J. Han, S-J. Lee, J-G. Jung, and Y-K. Lee, *Acta Materialia*, 2014, vol. 78, pp. 369-377

[10] P.J. Gibbs, E. De Moor, M.J. Merwin, B. Clausen, J.G. Speer, and D.K. Matlock, *Met Trans A*, 2011, vol. 42A, pp. 3691-3701

[11] A. Arlazarov, M. Goune, O. Bouaziz, A. Hazotte, G. Petigand, and P. Barges, *Mater Sci and Eng. A.* 2012, vol. 545, pp. 31-39

[12] D. M. Field, D.C. Van Aken, *Met Trans A.*, 2016 vol. 47A pp.1912-1917

[13] M.C. McGrath, D.C. Van Aken, N.I. Medvedeva, and J.E. Medvedeva, *Metall. Mater. Trans. A*, 2013, vol. 44A, pp. 4634-4643.

[14] C. D. Horvath, C. M. Enloe, J. P. Singh, and J. J.Coryell, *Intl. Symp. On New Developments in AHSS*, "Persistent Challenges to Advanced High-Strength Steel Implementation" Keystone, CO. 2017.

[15] J.F. Enrietto, *Jour. Of the Iron and Steel Inst.* 1966, pp. 252-258

[16] W. Wepner, *Arch. Eisenh.,* 1955, vol. 22, pp. 71-81

[17] J.D. Baird and A. Jamieson, *J. Iron and Steel Inst.,* 1966, vol. 204, pp.793-801

[18] P. Rodriguez, *Bull. Mater. Sci* 1984, vol. 6. Pp.653-663

[19] Y.N. Dastur and W.C. Leslie *Met. Trans. A* 1981, vol. 12A, pp. 749-759

[20] S-J. Lee, J. Kim, S.N. Kane, and B.C. De Cooman, *Acta Materialia*, 2011, vol. 59, pp.6809-6819

[21] R.W. Balluffi, *Phys Status Solidi*, 1970, vol.41 pp.11-21

[22] M. Kuzmina, M, Herbig, D. Ponge, S. Sandlöbes, and D. Raabe, *Science*, 2015, vol. 349, pp. 1080-1083

[23] N.I. Medvedeva, D. C. Van Aken, and J.E. Medvedeva "Magnetism in bcc and fcc Fe with carbon and manganese," *J. Phys. Cond. Matter* vol. 22, 2010, 316002

[24] Medvedeva, N.I, M.S Park, D.C. Van Aken, and J.E. Medvedeva, *J. Alloys Compd.*, 2014 Vol. 582, pp. 475-482

[25] J.B. Seol, J.E. Jung, Y.W. Jang, and C.G. Park, *Acta Materiallia*, 2013 vol. 61. pp.558-578

[26] B.K. Choudhary, K.B.S. Rao, S.L. Mannan, and B.P. Kashyap, *Mater. Sci. & Tech*, 1999, vol. 15, pp.791-797

[27] B.K. Choudhary, *Mater. Sci. & Tech*, 2013, vol. 29, pp.278-284

[28] B.K. Choudhary, *Mater. Sci. & Tech*, 2013, vol. 29, pp.303-309

[29] B.K. Choudhary, E.I. Samuel, G. Sainath, J. Christopher, and M.D. Mathew, *Met Trans A*, 2013, vol.44A, 4979-4992

[30] S. Venkadesan, C. Phaniraj, P.V. Sivaprasad, and P. Rodriguez, *Acta Metall. Mater.* 1992, vol. 40, pp. 569-580

[31] L.J. Cuddy, and W.C. Leslie, *Acta Met*. 1972, vol. 20, pp. 1157-1167

[32] K.T. Park, K.G. Jin, S.H. Han, S. W. Hwang, K. Choi, and C.S. Lee, *Mater. Sci. and Eng. A*, 2010, vol. 527, pp.3651-3661

[33] J. Kim, S.J. Lee, and B.C. De Cooman, *Scripta Materialia*, vol. 65, 2011, pp. 363-366

[34] P.G. McCormick, *Acta Metall.* 1972, vol. 20, pp.351-354

[35] A.W. Sleeswyk, *Acta Metall.* 1958, vol. 6. Pp.598-603

[36] K.R. Limmer J.E. Medvedeva, D.C. Van Aken, N.I. Medvedeva *Computational Materials Science*, vol. 99, 2015, pp.253-255

[37] D.M. Field, D.S. Baker, and D.C. Van Aken, *Met Trans A*, 2017, DOI. 10.100/s 11661-017-4020-2

[38] S.T. Pisarik and D.C. Van Aken, *Met Trans A.*, Vol. 47A 2016 pp1009-1018

[39] G.B. Olson, M. Cohen *Met Trans A* Vol 7 1976 pp. 1897-1904

[40] ASTM E 8/E 8M-08, Standard Test Methods for Tension Testing of Metallic Materials

[41] S. Martin, C. Ullrich, D. Simek, U. Martin, and D. Rafaja, *J. Appl. Crystallogr.*, 2011, vol. 44, pp. 779-787

[42] S. T. Pisarik, and D. C. Van Aken, *Met Trans A.*, 2014, vol. 45, pp. 3173-3178

[43] C.C. Kinney, I.Yi, K.R. Pytlewski, A.G. Khachaturyan, N.J. Kim, J.W. Morris Jr., *Acta Materialia*, 2017, vol. 125, pp.442-454

[44] C. Wert and C. Zener, *Phys. Rev.*, vol. 76, 1949, pp. 1169-1175

[45] C. Wells and R.F. Mehl, *Met Technol.* 1941 pp. 1282

[46] K. Oi, C. Lux, and G.R. Purdy, *Acta Mater.* 2000, vol. 48, pp. 2147-2155

[47] S. Shin, M. Kwon, W. Cho, I. S. Suh, and B.C. De Cooman, *Mater. Sci. & Eng.* 2017, vol. 683, pp. 187-194

[48] S.K. Huang, Y.H. Wen, N. Li, J. Teng, S. Ding, Y.G. Xu, *Materials Characterization*, 2008, vol. 59, pp. 681-687

III. CHEMISTRY AND PROPERTIES OF MEDIUM-MN TWO-STAGE TRIP STEELS

Daniel M. Field[a], Jingjing Qing[b], D.C. Van Aken[c]

[a] Missouri University of Science and Technology
Department of Materials Science and Engineering, Rolla, MO 65409
Phone: 573-341-4804
e-mail: dfb52@mst.edu

[b] Missouri University of Science and Technology
Department of Materials Science and Engineering, Rolla, MO 65409
Phone: 573-341-6467
e-mail: jq4g5@mst.edu

[c] Missouri University of Science and Technology
Department of Materials Science and Engineering, Rolla, MO 65409
Phone: 573-341-4717
e-mail: dcva@mst.edu

To be submitted to Materials & Design

ABSTRACT

Eight medium manganese steels ranging from 10wt. pct. to 15wt. pct. Mn have been produced with varying levels of aluminum, silicon and carbon to create steels with two-stage TRIP (transformation induced plasticity) character. Alloy chemistries were formulated to produce a range of intrinsic stacking fault energies (ISFE) from -2.2 to 13.3 mJ/m^2 when calculated at room temperature for the bulk composition. Two-stage TRIP behavior was documented when the ISFE of the austenite phase was 10.5 mJ/m^2 or less whereas an ISFE of 11.9 mJ/m^2 or greater exhibited TWIP (twin induced plasticity) and single stage TRIP forming α-martensite in the γ-austenite phase. Properties were measured in both hot band (hot rolled) and subsequently batch annealed (cold-rolled and annealed) conditions. Hot band properties were influenced by the Si/Al ratio and this dependence was related to incomplete recovery of high Si alloys. Batch annealing was conducted at 873K (600 °C) for 20 hours to produce an ultra-fine grained microstructure of less than 1 μm. Yield strength of batch annealed materials were found to exhibit a traditional Hall-Petch dependence upon grain diameter and ultimate tensile strengths ranges from 1451 MPa to 1064 MPa with total elongations of 27.2 pct. to 42.6 pct. Tensile ductility was shown to be proportional to the product of the volume transformed and the volume change associated with martensitic transformation. An empirical relationship based on the chemistry was derived for the ultimate tensile strength and elongation to failure of the batch annealed steels. From the developed understanding of the two-stage TRIP steels two new alloys were produced and obtained strengths of 1150 MPa with 58 pct. total elongation and a tensile strength of 1400 MPa and 32 pct. ductility.

1. INTRODUCTION

1.1 Deformation Mechanisms

Microstructural engineering is central to the development of 3rd generation advanced high strength steel for automotive application. Quench and partitioning is a common approach to obtain the desired combination of α-martensite and γ-austenite with partitioning of carbon to stabilize the γ-austenite. Ferrite and γ-austenite microstructures can also be obtained by cold working and partitioning of substitutional alloying elements (e.g. Al, Mn) in addition to carbon during intercritical anneals. In each case the γ-austenite created is metastable at room temperature and will transform to induce increased plasticity, i.e. greater formability and improved crashworthiness. Transformation induced plasticity (TRIP) in quench and partitioning steels is simply the transformation of γ-austenite to α-martensite. Medium manganese (5 to 12 wt.% Mn) steels are used for intercritical temperature partitioning and the TRIP behavior is more complicated by the possibility of twin induced plasticity (TWIP) prior to TRIP or two-stage TRIP where γ-austenite first transforms to ε-martensite and subsequently transforms to α-martensite. Dynamic strain aging also plays an important role in the mechanical properties of these medium manganese steels and this aspect has been reported elsewhere [1]. Mechanical twins and ε-martensite are both formed by the motion of partial dislocations in the γ-austenite. The distinction between the two is often generalized by calculation of the intrinsic stacking fault energy (ISFE) [2-5]. There have been many works on the ISFE range at which the formation of ε-martensite will transition to mechanical twinning. For intrinsic stacking fault energies ≥ 20 mJ/m^2 alloys will mechanically twin and no ε-martensite is observed. The works by Remy and Pineu [3], Allain et al. [4] and Lee et al. [5] showed that in the range of 12 – 17 mJ/m^2 both twins and ε-martensite are observed simultaneously. These works also show that for alloys formulated with calculated ISFE ≤ 12 mJ/m^2 the γ-austenite will transform to ε-martensite without twin formation.

Quench and Partitioning steels (Q&P) exhibit properties of ultimate tensile strengths in excess of 1500 - 1700 MPa and elongations to failure of 20 - 10 pct. [6-8]; likewise, medium-Mn steels in the range of 5 to 12 wt. pct. Mn demonstrate ultimate tensile strengths ranging from 1550 – 700 MPa and total elongations of 10 – 65 pct. [9-14]. Processing of medium manganese steels includes hot rolling to form a hot band of thickness 1.8 to 3.3 mm, cold rolling the hot band, and intercritical annealing within a temperature range of 873 – 1023K (600 – 750 °C) to obtain a metastable γ-austenite that TRIP's to α-martensite. Stability and volume fraction of retained γ-austenite is controlled by the time and temperature at which annealing is performed. Zhang et al. [15] investigated a 7 wt. pct. Mn steel annealed at 893K (620 °C) for times ranging from 3 minutes to 96 hours and found that the increased time at temperature coarsened the formed γ-austenite from 300nm to 940nm, but noted that the volume fraction of γ-austenite was relatively constant at ~40 vol. pct. During tensile testing the γ-austenite transformed to α-martensite. Luo et al. reported [16] on two 5wt. pct. Mn steels where the intercritical annealing temperature was varied to manipulate the Mn and C content of the γ-austenite. A maximum in the measured retained γ-austenite at ambient temperature was obtained by intercritical annealing at 943K (670 °C). Zhang et al. [17] investigated a 0.2C – 5Mn (in wt. pct.) steel hot worked, at an unspecified temperature, and annealed at 923K (650 °C) to fully recrystallize the microstructure. From hot working and annealing a tempered lath martensite was observed with γ-austenite formed between the laths. The steels were subsequently warm rolled at a subcritical temperature 923K (650 °C) with increasing reduction ratios from 0 pct. to 77 pct. They showed that finer lath spacing was obtained with increasing rolling strains, and the lath thickness was decreased from 0.6 μm to 0.2 μm with respective yield strengths of 490 to 980 MPa.

The TWIP combined with subsequent TRIP behavior has been observed in alloys formulated such that the room temperature intrinsic stacking fault energy of the γ-austenite is < 15 mJ/m^2 [14, 18,19]. Grässel et al. [19] investigated high manganese (> 15 wt. pct) steels with varying levels of silicon and aluminum. They concluded that when the TRIP effect was activated, the tensile strength was increased by as much as 180 MPa as a result of delayed necking to greater uniform strains. Song et al. [18] examined a lightweight duplex steel with composition of 0.32C – 5.8Mn – 5Al with bands of δ-ferrite; after processing the γ-austenite decomposed to a combination of α-ferrite, α-martensite, and γ-austenite. The unstrained γ-austenite contained annealing twins, but when plastically strained deformation bands formed with α-martensite forming by TRIP within deformation twins producing a combined TWIP – TRIP behavior. Lee et al. [17], showed that for a TWIP – TRIP steel the α-martensite that formed during tensile loading occurred at the intersection of TWIP deformation bands. In the work by Lee et al. [17] a set of constitutive models were developed using nano-indention to determine the strength of the γ-austenite and the annealed α-ferrite. A Hall-Petch relationship for the yield strength was also derived and is shown in eq (1)

$$\sigma_{yield}\left(MPa\right)=\frac{332\left(MPa\sqrt{\mu m}\right)}{\sqrt{D\left(\mu m\right)}}+223\left(MPa\right) \tag{1}$$

A two-stage transformation induced plasticity (TRIP) behavior [1, 20-23] may also be observed in manganese steels with 7 to 15 wt. pct. Mn provided the carbon content is held below 0.2 wt. pct. and alloying or partitioning of the γ-austenite produces an intrinsic stacking fault energy below 12 mJ/m^2 [2-5]. This two-stage TRIP behavior has been quantitatively followed using interrupted tensile testing and x-ray diffraction to characterize the strain dependent behavior and microstructural evolution. [1, 20] At strains less than 4% (strains up to 10% if yield point elongation is observed) the γ-austenite first transforms to ε-martensite and segments the γ-austenite into smaller volumes. As suggested by Lee et al. [24] γ-austenite grain refinement to the nano-meter scale can lower the α-martensite start temperature by as much as 100 K (100 C°) when the grain size is 200nm. In addition to this grain refinement, the formation of ε-martensite directly lowers the chemical driving force to form α-martensite. It should be noted that the ε-martensite is a more densely close packed structure than γ-austenite and the transformation strain during initial ε-martensite formation may help induce α-martensite upon further straining. A significant volume expansion on the order of 2.2% occurs when ε-martensite transforms to α-martensite during Stage II TRIP. [25] Microstructural refinement observed in these two-stage TRIP alloys is thought to be responsible for the high work hardening rates, high tensile strengths (>1200 MPa) and elongations to failure in excess of 25 pct. De Cooman et al. [26] studied a 7Mn steel that was intercritical annealed at 873K and 923K (600 °C and 650 °C) to produce a dual-phase α + γ ultrafine grain structure with the γ-austenite having an intrinsic stacking fault energy reported to be -5 mJ/m^2 and -14 mJ/m^2. The resultant γ-austenite was shown through TEM analyses to contain both ε-martensite and α-martensite. De Cooman states that the α-martensite in the steel studied is always nucleated within the ε-martensite. Shape memory Fe-Mn alloys also show a sequential martensitic transformation if strained beyond the elastic limit to produce unrecoverable strain. Both Huang et al. [27] and Shin et al. [28] have reported that strains greater than 4 pct. will inhibit the shape memory recovery response and it was found that the 4 pct. strain correlated closely to the formation of α-martensite within intersecting ε-martensite bands as observed using transmission electron microscopy [27, 28]. Recent work in the medium-Mn two-stage TRIP systems by Field and Van Aken [1] showed that the Stage II (ε→α) reaction occurred at 4 - 6 pct. strains. Both the shape memory alloys [20, 27, 28] and the earlier work of McGrath et al. proposed that the transformation to ε-martensite may occur at stresses below 300MPa when the γ-austenite grain size is 30 to 100μm. Recent developments with cold working followed by annealing of the two-stage TRIP steels at 873K (600 °C) to produce nanocrystalline grain structures have shown promise in increasing the yield-strength up to 830 MPa [1, 22].

1.2 Stacking Fault Energy

The importance of Mn as a major component in these two-stage TRIP steels can be demonstrated by first principle calculations of both the unstable stacking fault and intrinsic stacking fault energies as discussed by Medvedeva et al. [29], and Limmer et al. [30]. A generalized stacking fault energy curve is shown in Figure 1. A stacking fault is produced by shearing the fcc crystal on $\{111\}_\gamma$ in the direction of <112>. An unstable stacking fault is produced by $\frac{a}{12}$<112> or half the displacement of a Shockley partial dislocation. The resultant deformed crystal is typically at a higher energy and represents an unstable configuration. The unstable stacking fault energy represents the barrier to the nucleation of a Shockley partial dislocation. Displacing the crystal by a full partial dislocation leads to the formation of an intrinsic stacking fault. Stacking in the $\{111\}_\gamma$ changes the ABCABC stacking to an AB[CA|CA]BC where the stacking fault is seen as the break line, |, and the portion within the brackets represents four layers of $\{0001\}_\epsilon$ hcp crystal. Quite often the resultant intrinsic stacking fault energy (ISFE) at room temperature is negative (more stable than the fcc crystal structure), but is still unstable with respect to either the bcc crystal structure or α-martensite Medvedeva et al. [29] demonstrated a parabolic minimum at 12 atomic percent manganese for the ISFE provided the manganese resides at the stacking fault, whereas there is a continuous decrease in the USFE with manganese addition. Limmer et al. [30] showed that Mn is the only element to both lower the USFE and the ISFE making the ε-martensite both easier to form and more stable. Aluminum and silicon both lower the USFE making ε-martensite, and dislocation nucleation easier however they increase the ISFE [30A]. Medvedeva et al. [29] also calculated that carbon increases the ISFE when placed at the fault plane; however, Mn can help mitigate this effect by segregating to the fault plane to form a Mn-C dipole.

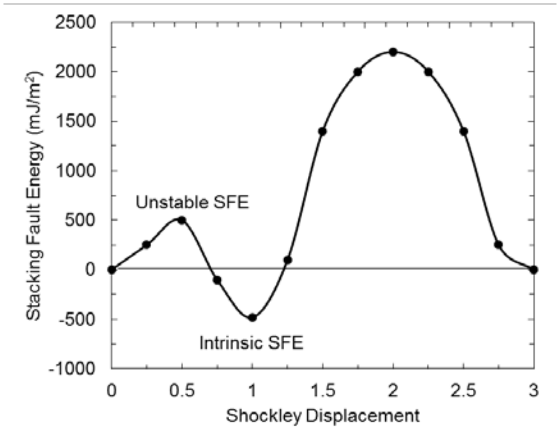

Fig. 1. Generalized stacking fault energy curve for pure Fe calculated by first-principles simulation. Unstable stacking fault energy (USFE) and intrinsic stacking fault energy (ISFE) are shown in the plot at 0.5 and 1.0. Graph redrawn from Medvedeva et al. [29].

1.3. Effect of Chemistry

The complex effect of Mn has also been presented in the works of Pisarik and Van Aken [31] and Field et al. [32]. Thermodynamic calculations by Pisarik and Van Aken [31] determined that the ε-martensite start temperature is related to Mn in a parabolic fashion, with a minimum occurring at roughly 12-13 wt. pct. Mn. Similar work by Field et al. on the start temperature for α-martensite [32] yielded two distinct behaviors in the thermodynamic driving force for α-martensite formation. Alloys that contained greater than 12 wt. pct. manganese exhibited a greater temperature dependence for the driving force of transformation and alloys having less than 12 wt. pct. manganese exhibited a thermodynamic relation similar to what had been reported for lath martensitic steels. However, the proposed model was limited Mn contents less than 16 wt. pct. for the prediction of α-martensite start temperatures.

Automotive steels are typically produced as a hot band product with a gauge thickness between 1.8 and 3.3 mm [33] and recrystallization behavior of the hot band steel is of significant concern for subsequent cold rolling. Hot band properties reported by Field and Van Aken [1] for a two-stage TRIP steel with 2.4 wt. pct. Si exhibited a high ultimate tensile strength of 1840 MPa and elongations of 13 pct. whereas the same steel after cold working and batch annealing produced a ultimate tensile strength of 1400 MPa and an elongation to failure of 34 pct. It has been reported in literature that substitutional alloying elements like silicon and aluminum will influence the dynamic and static recrystallization of TRIP steels [34-36]. Suikkanen et al. [34] found that the rate of static recrystallization linearly decreased with increasing Si up to 1.5 wt. pct. This effect has also been observed in the works by Somani et al. [37], Medina and Mancilla [38], and Medina and Quispe [39]. Silicon’s effect on recrystallization has been rationalized assuming a solute drag effect on grain boundaries. Li-Juan et al. [35] investigated the effect of Si and Mn on the dynamic recrystallization of conventional TRIP steel and showed that Mn had little effect on the dynamic recrystallization; however, they observed that silicon was effective in slowing the dynamic recrystallization and increased the static recrystallization temperature. It was also shown by Zhu et al. [36] that the dynamic recrystallization response is greatly impeded when the silicon content is increased to 1.5 wt. pct. silicon.

Little has been reported on the influence of Al on the recrystallization of TRIP steel. Somani et al. [34] found that Al had a negligible effect on static recrystallization. Aluminum’s effect on the properties of first generation advanced high strength TRIP steels is considered to be very complicated. Aluminum has been shown to affect the work hardening behavior and the dynamic strain aging (DSA) response of TWIP and TRIP steels [1, 19, 40]. It has been shown in the high-Mn TWIP steels that Al additions will reduce the work hardening rate by reducing the deformation twin density [40]. Lee et al. [40] investigated the dynamic strain aging of two TWIP steels, one containing aluminum, 0.6C-18Mn-1.5Al-BalFe (wt. pct.), and the second being an Al-free 0.6C-18Mn-balFe (wt. pct.) steel, and it was observed that the work hardening rate and ultimate tensile strength were reduced with the addition of aluminum. Lee et al. showed that Al was effective in suppressing the dynamic strain aging of the TWIP steel. Work by Grässel et al. [19] shows that the ultimate tensile strength of 15Mn-xSi-yAl (in wt. pct.) exhibited a decrease in ultimate tensile strength with increasing aluminum content and that the ductility increased with increasing aluminum content. The effects silicon and aluminum on recrystallization are of great concern for potential two-stage TRIP steels because both Al and Si reduce the USFE [30] and are considered favorable alloying elements for ε-martensite formation.

Nitrogen and carbon are also expected to affect the strength of the newly designed two-stage TRIP steels. Field and Van Aken [1] found that nitrogen in α-ferrite was a potential cause for both static and dynamic strain aging in an intercritically annealed 10 wt. pct. Mn steel. It is well established that DSA leads to increased ultimate tensile strengths and reduced elongations. Two additional DSA mechanisms were identified: in microstructures containing ε-martensite trapping of Mn atoms at stacking faults and Mn-C defect pairs in γ-austenite also contribute to dynamic strain aging.

The purpose of this work is to attempt to understand and empirically model the effect of chemistry and microstructure on the measured properties of recently developed medium-Mn two-stage TRIP steels and to show how stacking fault energy calculations can be used to formulate two-stage TRIP alloys.

2. MATERIALS AND METHODS

Eight alloys used for this investigation were melted using induction iron, ferrosilicon, electrolytic manganese, pure aluminum, and carbon in the form of graphite. An argon cover gas was used to shield the melt and calcium wire additions were made to modify oxide inclusions and remove sulfur. Composition was both verified by optical emission spectroscopy and adjusted prior to tapping the furnace into a ladle. A modified ladle using a ceramic dam to force liquid from below the surface to form the pouring stream in a manner similar to a teapot was used for pouring the steel. All alloys were cast with 150K (150 C°) superheat into phenolic no-bake sand molds to form multiple Y-blocks each with dimensions measuring 12.6 x 6 x 1.7 cm. The upper Y-portion of the Y-block acts as a riser, but this was also attached to a Foseco KALPUR insulated riser with a diameter of 13.5 cm and height of 15.3 cm to ensure the soundness of the lower leg of the Y-block casting. The reported chemical analyses were obtained by ion coupled plasma spectrometry after sample dissolution in hydrochloric and nitric acid. Carbon and Nitrogen contents were determined using a LECO CS6000 and a LECO TC500 combustion analyzers, respectively. Alloy composition, calculated room temperature ISFE and martensite start temperatures are listed in Table I. The martensite start temperatures were calculated according to the works of [31, 32]. For brevity alloys will be designated by the room temperature (298K, 25 °C) calculated ISFE values (bulk composition) and designated in the form # SFE. Stacking fault energies were calculated using Olson and Cohen's equation [41] shown below as eq (2)

$$SFE(mJ/m^2) = n\rho(\Delta G^{\gamma\rightarrow\varepsilon}) + 2\sigma^{\gamma/\varepsilon} \tag{2}$$

The driving force for transformation, $\Delta G^{\gamma\rightarrow\varepsilon}$, was obtained using an updated regular solution model [31], n=2, ρ calculated using alloy chemistry and Vegard's law for the planar atomic density of the $\{111\}_{\gamma}$, and $\sigma^{\gamma/\varepsilon}$ is the interfacial energy between the γ-austenite and ε-martensite, which was held constant at 10 mJ/m^2. The start temperature for the ε-martensite was calculated by determining the temperature at which SFE = 0 mJ/m^2 for the case where n = 4 [31]. Themartensite start temperature, M_S^{α}, was calculated according to the work by Field and Van Aken [32], where the strain energy of transformation, ($\Delta G_{str}^{\gamma\rightarrow\alpha}$) was balanced against the chemical driving force ($\Delta G_{Chem}^{\gamma\rightarrow\alpha}$) according to eq. (3) and eq. (4).

$$\Delta G_{str} + \Delta G_{Chem}^{\gamma\rightarrow\alpha} = 0 \tag{3}$$

$$\Delta G_{Str}^{\gamma\rightarrow\alpha} \left({}^{J}\!/_{mol} \right) = E\Omega\delta^2 \left(14.8 - 0.013T \right) \tag{4}$$

where $\Delta G_{Chem}^{\gamma\rightarrow\alpha}$ is calculated according to a modified regular solution model described in Field et al. [32]. Ω is the molar volume for iron of $7.15*10^{-6}$ (m^3/mol), δ is the lattice misfit between the γ-austenite and α-martensite with an approximate strain of $1.11*10^{-2}$ (m/m), T is the temperature in Kelvin and E is the modulus in units of Pa. The start temperature for the α-martensite was calculated by determining the temperature where eq. (2) is true.

Table I. Composition and the calculated start temperature for the ε and α martensites

Alloy	**Composition (wt. pct.)**					**Calculated Parameters**	
	Mn	**Si**	**Al**	**C**	**N**	**Ms^{ε} in K (°C)**	**Ms^{α} in K (°C)**
13.3 SFE	13.9	2.07	2.01	0.09	0.012	284 (11)	397 (124)
13.0 SFE	11.1	1.37	1.49	0.27	0.018	274 (1)	371 (98)
7.8 SFE	15.1	1.95	1.40	0.08	0.017	311 (38)	424 (151)
5.0 SFE	14.3	2.97	0.89	0.16	0.022	360 (87)	428 (155)
-0.2 SFE	10.2	2.38	0.30	0.17	0.024	387 (114)	417 (144)
-1.8 SFE	11.5	2.46	0.38	0.11	0.029	400 (127)	383 (110)
-2.1 SFE	13.8	2.01	0.40	0.10	0.028	405 (132)	381 (108)
-2.2 SFE	13.0	1.57	0.45	0.10	0.045	404 (131)	354 (81)

The steel castings were normalized at 1373K (1100 °C), held at temperature for 2 hours, and air cooled to 298K (25 °C). Castings were milled to an orthogonal prism of dimensions 15.5 x 125 x 50 mm^3 and hot rolled sequentially by heating to 1223K (950°C), rolling, and reheating to 1223K (950 °C). This was repeated to obtain a hot band gauge of 2.5 mm. A total hot reduction of 87.2 ± 6.8 pct. was accomplished and an exit temperature of 1068 ± 15K (775 °C) was measured after the final roll pass to obtain the desired hot band thickness. Hot band tensile properties were measured to determine a target range for cold rolling. Experience processing these alloys suggested that the cold rolling reduction be limited to a range of two to three times the total elongation measured for the hot band condition. Alloys were cold rolled using a Stanat TA 315 in a 4-high roll configuration. Industrial batch annealing was mimicked by placing the cold rolled sheet into stainless steel bags and heated to 873K (600 °C) at a rate of 20K/min, allowed to equilibrate at temperature, holding for 20 hours, and air cooled to 298K (25 °C) at an average rate of 10K/min. Gray iron machining chips were added to the stainless steel bags to provide atmosphere protection.

Tensile bars were cut from both the hot band and batch annealed materials parallel to the rolling direction and the gage edge was milled to produce a standard ASTM E8 [42] tensile bar with a gage length of 50 mm and gage width of 12.5 mm. Gage width surfaces were not ground or machined. Tensile tests were conducted at room temperature and Young's modulus was determined using a clip-on extensometer. Tests were performed in displacement control at a rate of 0.01 mm/sec using a 245 kN servo-hydraulic test frame. A non-contact laser extensometer was used to measure the total strain to failure. Non-metallic inclusions were characterized with an automated feature analysis using an ASPEX scanning electron microscope with an accelerating voltage 20.0 kV, magnification of 1000 x and the threshold size range was set to 0.3 – 40 μm to determine the inclusion population of the developed steels.

X-ray diffraction (XRD) patterns were collected for all mechanically tested conditions to investigate the microstructural development during processing. XRD samples were mechanically polished to 0.1 μm using diamond paste in the Longitudinal-Transverse plane, (polished surface parallel to the rolling plane) and diffraction patterns were obtained with a Phillips X-pert diffractometer using Cu Kα radiation with a nickel filter and a flat graphite monochromator. Phase quantifications were calculated utilizing the Rietveld refinement described by Martin et al. [43] on an Fe-16Cr-6.8Mn-6.1Ni steel for ε-martensite analysis, and modified for the steel chemistry being investigated in this study. Work to correlate the total volume change from the various phases present and total tensile elongation was done on the alloys in both the hot band and batch annealed steels. The lattice parameter of the γ and α` crystalline phases were measured using x-ray diffraction. The ε-martensite lattice parameters were calculated assuming an ideal c/a ratio of 1.633, which can be justified based upon iron-manganese shape memory alloys [44]. The lattice parameter for the ε-martensite was confirmed using transmission electron microscopy. A percent change in volume was calculated according to eq (5).

$$\Delta V^{i \to j} = 100\% \left(\frac{V^i - V^j}{V^i} \right) \tag{5}$$

V^i is the volume of the initial phase and V^f is the volume of the final phase, the total volume change is then calculated by eq (6).

$$Total \Delta V = \Delta V^{\gamma \to \varepsilon} (\gamma_{vol\%}) + \Delta V^{\varepsilon \to \alpha} (\gamma_{vol\%} + \varepsilon_{vol\%}) \tag{6}$$

Specimens for electron back-scattered diffraction (EBSD) were mechanically polished with a 0.02 μm colloidal silica solution using a vibratory polisher and examined in Longitudinal-Short plane (perpendicular to both the rolling plane normal and the rolling direction). Orientation image mapping via pattern analysis was performed on a Helios Nanolab 600 using a Nordlys detector and the Aztec 3.3 software package. The electron beam was operated at an accelerating voltage of 20.0 kV and an emission current 11 nA. Orientation image maps and diffraction patterns were tilt corrected for the system geometry. Degree of recrystallization was determined using the post processing software Channel 5 on multiple EBSD maps to produce a total measured area of 0.1 mm^2, grains containing internal misorientation greater than 5° where considered deformed, and grains with misorientation less than 1° were considered fully recovered. Grain size was measured according to the ASTM E112 – 13 using the Heyn Lineal Intercept method. Transmission electron microscopy (TEM) analysis was performed using an FEI Tecnai F20 TEM. Thin foils for TEM analysis were analyzed in the Longitudinal-Transverse plane and prepared using a solution of 6 pct. perchloric acid, 60 pct. methanol and 34 pct. butoxyethanol and a dual-Jet electropolishing system operating at 243K (-30 °C) utilizing a DC current of 10 - 12mA to keep a constant voltage of 20V. The electron beam was operated at an accelerating voltage of 200 kV.

3. RESULTS

Stress-strain plots of the hot band and annealed condition are shown in Figure 2. A summary of the tensile properties in both conditions are listed in Table II. Microstructural characterization as performed by XRD to determine phase percentages are shown in Table III. Only alloys with positive stacking fault energies exhibit two sequential stages or rates of work hardening in the hot band materials: an initial stage with a low work hardening rate typically associated with ε-martensite formation and a subsequent rapid work hardening rate during the formation of α-martensite as shown in Figure 2(a). The observation of two different rates of work hardening is often described as an inflection in the stress strain curve, but should not be confused with a yield point elongation phenomenon. Hot band steels containing more than 30 pct. γ-austenite (and SFE > 0) produce a yield strength less than 380 MPa, a low work hardening rate (n~0.05), and elongations on the order of 3-7% prior to the onset of rapid work hardening. After cold working and annealing alloys with a bulk ISFE less than 13 mJ/m^2 exhibit an inflection in the stress versus strain plot shown in Figure 2(b). From Table III it is also noted that the alloys with a bulk ISFE ≥ 7.8 mJ/m^2 do not contain any ε-martensite in the starting microstructure. To determine if these alloys exhibited the two-stage TRIP phenomenon XRD was performed on partially strained sections of the tensile bar and is shown in Figure 3 for the 7.8, 13.0 and 13.3SFE alloys. The 7.8SFE alloy does exhibit ε-martensite formation from strains as low as 5 pct whereas XRD patterns of the 13.0SFE and 13.3SFE alloys do not contain ε-martensite in either the partially strained or failure strain condition. From this result it can be deduced that the 13.0 and 13.3SFE alloys are not two-stage TRIP alloys.

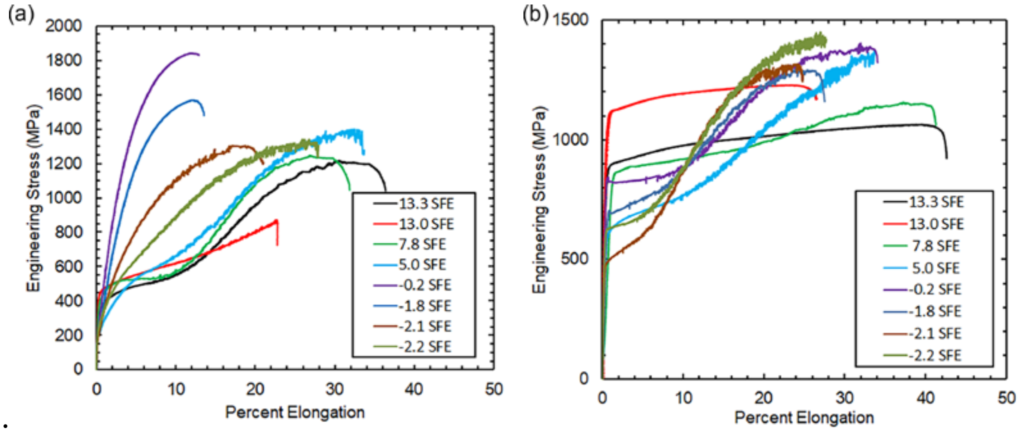

Fig. 2. Stress-strain graph of the (a) hot band and (b) cold worked and annealed steels

Table II. Mechanical properties of the hot band and processed steel with grain size measured by the mean linear intercept.

	Hot Band					**Cold Worked and Annealed**			
Alloy	**YS (MPa)**	**UTS (MPa)**	**e_f (%)**	**Grain Size L_3 (μm)**	**Cold Work (%)**	**YS (MPa)**	**UTS (MPa)**	**e_f (%)**	**Grain Size L_3 (μm)**
13.3 SFE	330	1220	36.4	11.7	65.1	880	1060	42.6	0.48
13.0 SFE	450	785	19.1	12.2	55.0	1120	1330	26.5	0.68
7.8 SFE	380	1250	31.9	13.9	66.4	850	1160	41.3	0.35
5.0 SFE	205	1400	33.7	23.0	69.3	595	1370	33.7	1.56
-0.2 SFE	260	1840	12.9	16.2	35.6	840	1400	34.1	0.34
-1.8 SFE	210	1570	13.6	17.2	33.2	790	1300	27.5	0.50
-2.1 SFE	240	1300	21.0	10.7	53.6	500	1320	24.8	1.31
-2.2 SFE	255	1340	28.0	10.6	57.1	615	1450	27.7	1.23

Table III. Phase quantities of the hot band and processed steel according to x-ray diffraction.

Alloy	Hot Band γ (vol%)	 ε (vol %)	 α (vol %)	Cold Worked and Annealed γ (vol%)	 ε (vol %)	 α (vol %)
13.3 SFE	95	0	5	64	0	31
13.0 SFE	94	0	6	81	0	19
7.8 SFE	79	0	21	60	0	40
5.0 SFE	93	7	0	64	30	6
-0.2 SFE	20	26	54	32	10	58
-1.8 SFE	24	24	52	34	13	53
-2.1 SFE	14	45	41	67	14	19
-2.2 SFE	36	21	43	64	33	3

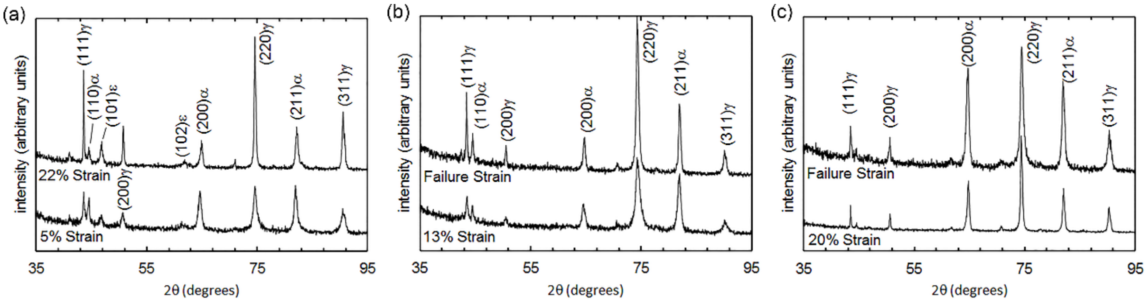

Fig. 3. X-ray diffraction of the partially strained (a) 7.8 SFE, (b) 13.0 SFE and (c) 13.3 SFE alloys, with the peak positions for the γ-austenite, α-ferrite/martensite and ε-martensite labeled

The hot band 13.0SFE alloy failed before the onset of necking while the 5.0SFE, -0.2SFE, and -2.1SFE alloys exhibit limited (< 1.5 pct.) post necking ductility. In addition, neither the batch annealed 5.0 or -2.2 SFE alloys exhibited necking prior to failure. The density (#/mm^2) and area coverage (μm^2/mm^2) of non-metallic inclusions are shown in Table IV. The inclusion family with the highest density for nearly all of the alloys is AlN with the exception of 5.0 SFE and -1.8 SFE steels. The 5.0 SFE alloy has a higher density of MnS type inclusions and the -1.8SFE alloy contains a majority of its inclusions as MnO – SiO_2 type inclusions. The AlN content shows a correlation to the total N content of the steel, with an increase in N associated with an increase in AlN; this is most directly observed in the -2.2 SFE alloy having the highest nitrogen content (0.045 wt. pct.) and the highest density of aluminum nitrides.

Table IV. Inclusion density (ρ) measured as number/mm^2 and area fraction (ppm) measured in $\mu m^2/mm^2$ of non-metallic inclusions measured using the ASPEX automated feature analysis.

	13.3SFE		13.0SFE		7.8SFE		5.0SFE		-0.2SFE		-1.8SFE		-2.1SFE		-2.2SFE	
	ρ	ppm	ρ	ppm	ρ	ppm	ρ	ppm	ρ	ppm	ρ	ppm	ρ	ppm	ρ	ppm
MnO - SiO_2	3	70	18	210	4	100	27	30	137	18	110	23	88	29	101	12
MnO - Al_2O_3	25	21	32	33	22	10	45	61	24	10	76	6	32	55	58	9
AlN	53	8	181	15	50	5	37	12	200	3	56	18	127	2	493	15
MnS	16	4	62	15	6	2	75	11	133	2	26	3	48	2	25	1

EBSD-OIM was utilized to quantitatively determine the grain size and phase constitution of the hot band and batch annealed alloys. EBSD-OIM phase maps showing grain size are shown in Figure 4(a) for the -2.2 SFE and Figure 4(b) for the 13.3 SFE steels in the hot band condition. The cold worked and annealed steels exhibit a high degree of microstructural refinement as shown in Figure 5 for the eight alloys tested. Two types of microstructures were developed after batch annealing. The 13.3, 13.0, 7.8, -0.2, and -1.8SFE alloys produced microstructures consistent with an intercritical anneal to obtain a γ + α-ferrite structure and these steels exhibit the highest degree of microstructural refinement. The 5.0, -2.1, and -2.2SFE alloys exhibited a larger grained (>2 μm) γ-austenite with athermal ε, and α-martensite and it is understood that the microstructure at 873K (600 °C) for these three alloys was nearly 100% γ-austenite. The average mean free path (L_3) between phase boundaries measured in the batch annealed (cold worked and annealed) steel ranged from 320 nm to 1.3 μm.

To better determine the lattice parameter of the three phases of interest γ, ε, and α transmission electron microscopy (TEM) was utilized. A TEM micrograph is shown for the -2.2SFE steel in Figure 6 with the associated diffraction patterns. TEM was utilized to confirm the ε-martensite phase and determine the lattice parameters: a = 2.62, c = 3.96 Å, and c/a=1.51. A Shoji-Wasserman orientation relationship was observed between the parent γ-austenite and the ε-martensite and is in agreement with previous work on the γ, ε, and α orientation relationships observed for athermal martensites [45] and martensites formed during straining [28],

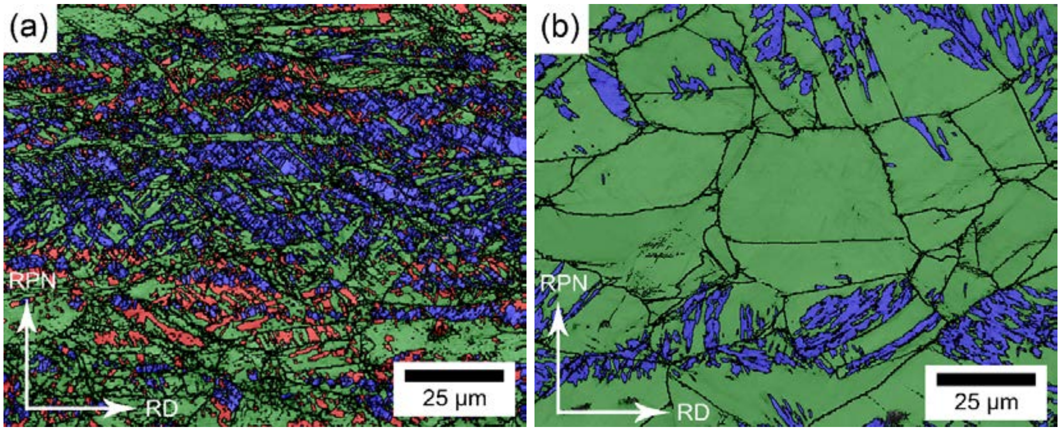

Fig. 4. EBSD-OIM of the hot band (a) -2.2 SFE (Si/Al=3.49) where prior γ-austenite grain boundaries are darkened and (b) 13.3 SFE (Si:Al=1.03) steels. γ-austenite is green ϵ-martensite is red and α-martensite is blue.

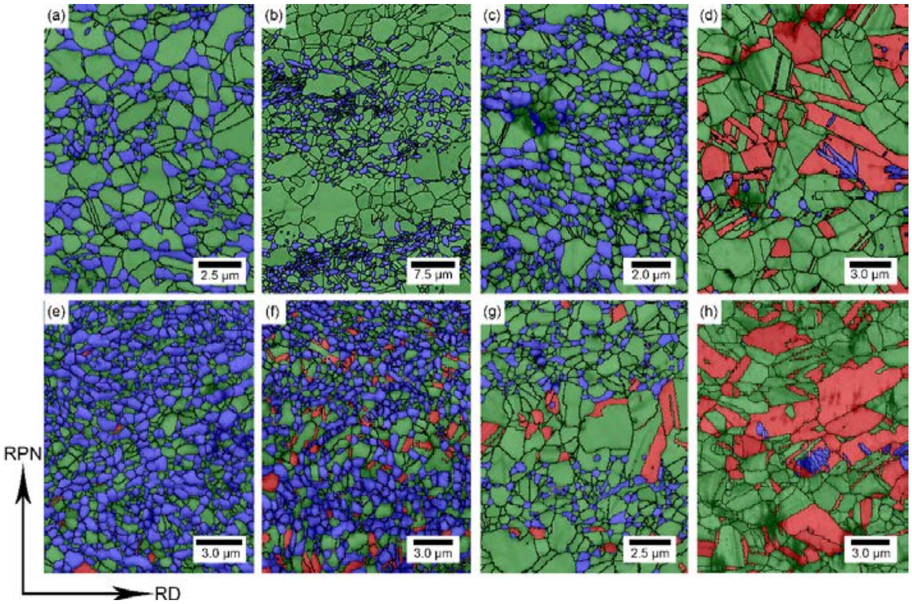

Fig. 5. EBSD-OIM map of the cold worked and annealed steel (a) 13.3 SFE, (b) 13.0 SFE, (c) 7.8 SFE, (d) 5.0 SFE, (e) -0.2 SFE, (f) -1.8 SFE, (g) -2.1 SFE, and (h) -2.2 SFE alloys. γ-austenite is green ε-martensite is red and α-ferrite is blue.

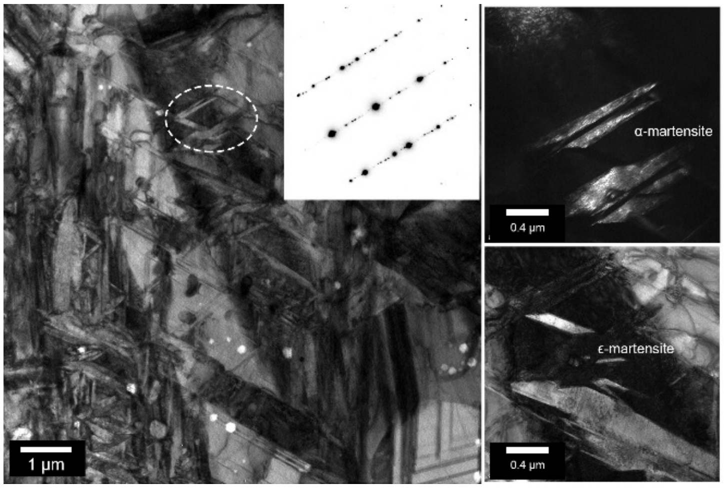

Fig. 6. Transmission electron micrograph of the -2.2 SFE alloy showing the two-stage TRIP products of ε-martensite and α-martensite and the diffraction patterns utilized for darkfield imaging of the ε-martensite and α-martensite.

A Hall-Petch grain size dependence for yield strength is graphed in Figure 7 for the eight alloys tested and 43 additional alloys from literature [11, 13, 15, 40, 46-57] with grain diameters ranging from 30-0.30 μm. Data was taken from austenitic stainless steel, dual-phase α-martensite/α-ferrite, and medium-Mn steels. A linear fit is shown for the data presented in this study, but the 13.0 SFE alloy was excluded because the grain size was bimodal. Figure 7(b) compares the grain size to yield strength relationship for the alloys presented in this study and previously reported medium-Mn steels. The Hall-Petch grain size relationship shown in Figure 7 is very similar to that reported by Lee et al. [17] as shown in eq (1) with a similar grain boundary hardening term, K, (393 MPa•μm$^{1/2}$ versus 332 MPa•μm$^{1/2}$) and friction stress, σ_0, (184 MPa versus 223 MPa) and is discussed in greater detail below.

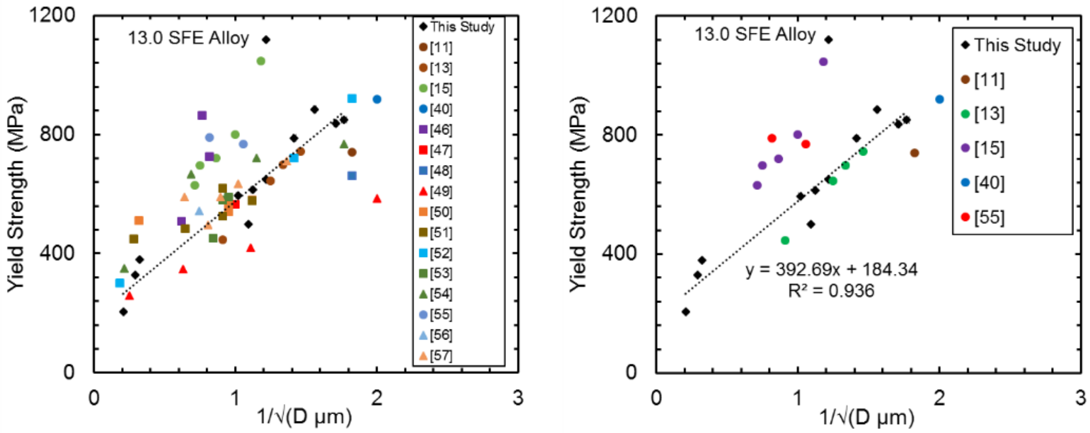

Fig. 7. (a) Comparison of the Hall-Petch inverse root grain size relationship of alloys produced in this study to reported austenitic stainless steels (triangles), dual-phase steels (squares), and medium-Mn steels (circles). (b) Hall-Petch relationship for medium-Mn steels and the steels presented in this work. The line fit is restricted to measurements of this study and is the same in both graphs. The 13.0 SFE alloy was excluded due to the highly bimodal grain size.

From the EBSD-OIM mapping the degree of recovery/recrystallization was measured for the hot band condition to understand the role of Si and Al on the tensile behavior of these steels. The degree of recovery/recrystallization was measured from multiple maps on each specimen to obtain a total map size of 0.1 ± 0.02 mm^2 area. A representative phase map and recovery/recrystallization map of the 7.8SFE steel are shown in Figure 8, and it is observed that there are twinned γ-austenite grains in the structure; however, many of the annealing twins appear bent and the grain aspect ratio shows an elongation parallel to the rolling plane. The volume pct. recovered/recrystallized defined as less than 1° of misorientation within the grain and deformed defined as greater than 5° of misorientation within the grain relative to the Si:Al ratio is shown in Figure 9 with the uncertainty measured to a 95% confidence level. In general, a non-linear behavior is found showing that a greater resistance to recovery/recrystallization is observed with increasing Si/Al ratio.

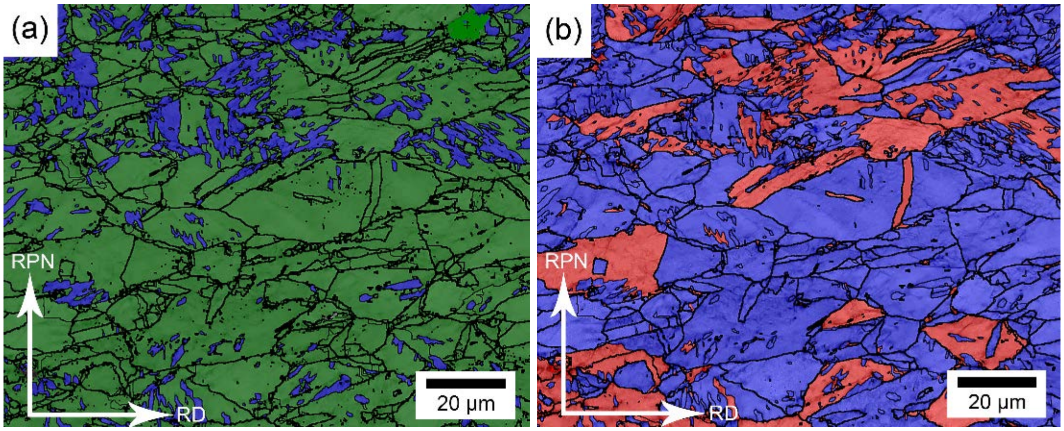

Fig. 8. (a) phase map of the 7.8SFE alloy in the hot band condition where green is γ-austenite and blue α-ferrite/martensite. (b) recrystallization map of the 7.8SFE alloy where blue grains are defined as recrystallized and red grains are defined as substructured and deformed grains. The Si:Al of this alloy is 1.39

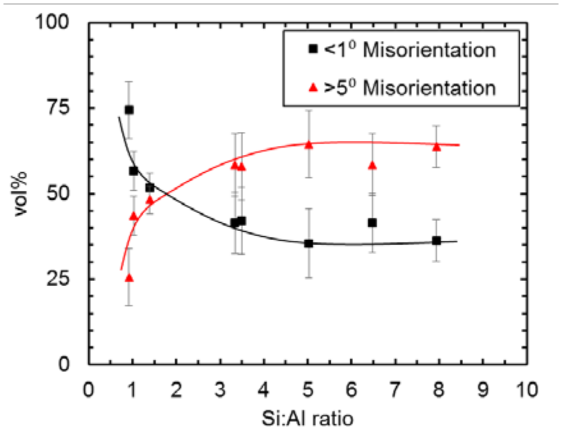

Fig. 9. The state of deformation measured according to EBSD, volume fraction of both the recrystallized and deformed grains are determined by the mean angular distribution as a function of silicon to aluminum ratio.

A Q-R factorization to obtain a least squares fit was used to determine an empirical relationship between the chemistry and ultimate tensile strength and total elongation for the batch annealed steels exhibiting two-stage TRIP behavior, i.e. alloys with ISFE less than 10 mJ/m^2. The derived relationships are shown in eq. (7,8) where x_i represents weight percent alloying element “i”, it should be noted that carbon and nitrogen have large positive effect upon the ultimate strength. A comparison of the calculated and measured strength is shown in Figure 10 and a relative error of ±0.05% was determined for the tested materials.

$$UTS(MPa) = 2579*(x_C) + 13.3*(x_{Mn}) - 41.7*(x_{Si}) - 29.4*(x_{Al}) + 7818*(x_N) + 747 \quad (7)$$

$$\%e_{tot} = 77*(x_C) - 2.0*(x_{Mn}) - 5.0*(x_{Si}) + 19.1*(x_{Al}) - 115*(x_N) + 50.6 \quad (8)$$

Partitioning of the alloying elements during the intercritical annealing at 873K (600 °C) heat treatment of the steels occurs and can be used to differentiate α-ferrite formed during the 873 K (600°C) anneal and α-martensite. Figure 11 shows the partitioning of Al and Mn for the 13.3 SFE and 5.0 SFE alloys. Energy-dispersive x-ray spectroscopy (EDS) mapping was performed during EBSD analysis and reveals that α-ferrite grains formed during annealing are rich in aluminum and lean in Mn. Thus regions identified as α-phase that do not show alloy partitioning can be identified uniquely as α-martensite as shown in Figure 11(b) and are highlighted by arrows in the figure. There are equiaxed α grains, as well as lenticular α crystals within ε-martensite bands, and both are shown in blue. Accompanying EDS maps allow the α-ferrite grains to be differentiated from the α-martensite: equiaxed α-ferrite grains are denuded in manganese and rich in aluminum as a result of solute partitioning during intercritical annealing. Athermal α-martensite could not be differentiated by chemistry and was typically observed within the ε-martensite bands as reported by Field and Van Aken [1] and De Cooman et al. [26]. A summary of the compositions measured from EDS analysis are shown in Table V. Equilibrium calculations performed using FactSage 7.0 with the FSstel database are also included in Table V for reference. To better replicate the composition of the α-ferrite and γ-austenite composition using the thermodynamic software a temperature was determined to reproduce the measured α-ferrite volume fraction from Table IV and adjustments were made from the EBSD analysis if only α-martensite was observed as was the case with the -2.2SFE steel. It was also assumed that the total γ-austenite at the batch annealing temperature included the athermal ε-martensite that formed upon cooling. Carbon and nitrogen reported in Table V are calculated assuming full partitioning to the γ-austenite and the absence of AlN. The average calculated temperature that matched the measured α-ferrite was found to be 808 ± 17K (535 °C). The 65K (65 C°) difference in temperature between calculated and experimental annealing temperature to match the α-ferrite content is likely due to (1) the alloy systems are non-dilute and (2) the kinetics for substitutional diffusion are sluggish at the intercritical annealing temperature and paraequilibrium partitioning might not have been obtained in the 20 hour treatment.

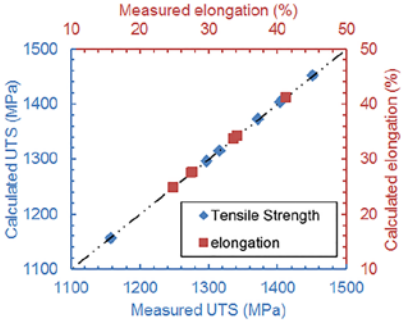

Fig. 10. Graphical comparison of the calculated properties to the measured values showing a fit of ± 0.05% with alloys exhibiting two-stage TRIP behavior, (ISFE < 10 mJ/m^2)

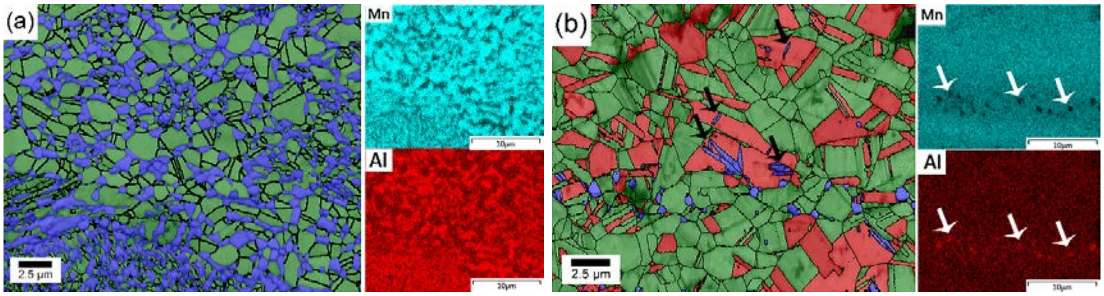

Fig. 11. (a) An EBSD-OIM map and the distribution of Mn and Al, in 13.3 SFE alloy and (b) EBSD-OIM map and the distribution of Mn in the 5.0 SFE alloy where α-martensite is highlighted by black arrows in the EBSD-OIM map and the α-ferrite is highlighted by white arrows in the EDS maps. α-ferrite/α-martensite (blue) grains show increased concentration of aluminum and reduced concentration of manganese, and conversely for the γ-austenite (green).

The total elongation was correlated to the lattice parameter and the calculated volume change associated with the two martensitic reactions determined according to eq (5) and eq 6) and is shown in Figure 12. Two parallel trends are observed. The alloys that contain equiaxed α-ferrite after batch annealing have a greater total ductility for an equivalent volume change compared to the hot band alloys. Batch annealed alloys that are coarser grained (> 2 μm) contain α primarily in the form of α-martensite and exhibit behavior similar to the hot band alloys with respect to the ductility response.

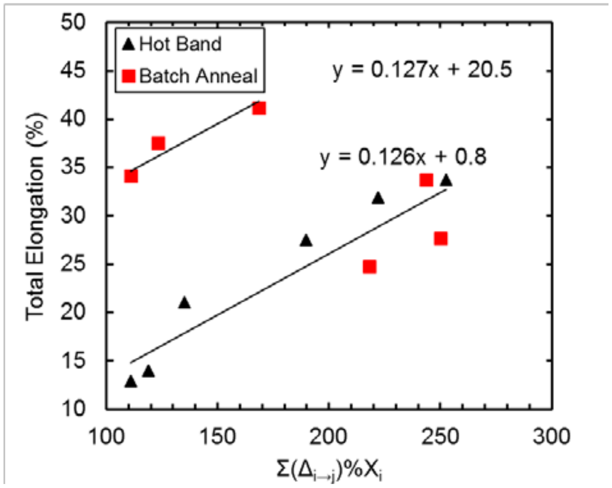

Fig. 12. Volume percent transformable product multiplied by the volume change associated with its martensitic reaction and its effect on the total elongation for the steels exhibiting the two-stage TRIP steels (ISFE ≤ 7.8 mJ/m^2).

Table V. Measured composition of the γ-austenite and α-ferrite after coldworking and annealing the steels at 873K (600°C) with a 95% confidence level standard deviation. Thermodynamic calculations of the phase composition performed to match measured phase quantities. Ms^{α} was not calculated for γ-austenite compositions greater than 14 wt. pct. Mn due to the model limitation described in the work by Field et al. [32]

		EDS								FactSage							
		(Composition wt. pct.)									(Composition wt. pct.)						
	Phase	Mn	Si	Al	C*	N*	SFE (mJ/m^2)	Ms^{ε} K	Ms^{α} K	FactSage Temperature K (°C)	Mn	Si	Al	C	N	Ms^{ε} K	Ms^{α} K
13.3SFE	γ	18.0 ± 0.8	1.95 ± 0.34	1.45 ± 0.29	0.12	0.03	12.1	279	-	**813 (540)**	18.5	2.10	1.76	0.13	0.021	243	-
	α	12.5 ± 1.0	2.06 ± 0.23	2.32 ± 0.27	0.02	0.10					4.06	2.00	2.57	<0.001	0.008		
13.0SFE	γ	12.4 ± 2.2	1.41 ± 1.1	1.25 ± 0.55	0.33	0.01	11.9	283	431	**793 (520)**	13.1	1.41	1.38	0.37	0.022	267	465
	α	10.4 ± 1.2	1.51 ± 0.22	1.43 ± 1.0	0.02	0.10					2.92	1.21	1.96	<0.001	0.002		
7.8SFE	γ	16.8 ± 1.0	1.68 ± 0.21	1.42 ± 0.21	0.12	0.04	10.5	259	-	**818 (545)**	21.0	1.96	1.16	0.12	0.033	258	-
	α	12.5 ± 2.8	1.73 ± 0.23	1.90 ± 0.39	0.02	0.10					4.25	1.94	1.76	<0.001	0.007		
5.0SFE	γ	16.3 ± 1.5	2.47 ± 0.42	0.72 ± 0.11	0.17	0.02	4.7	340	-	**803 (530)**	15.1	2.92	0.79	0.19	0.025	329	-
	α	11.7 ± 2.6	2.6 ± 1.22	1.03 ± 0.23	0.02	0.10					4.52	3.16	1.99	<0.001	0.005		
-0.2SFE	γ	12.3 ± 3.0	2.1 ± 0.52	0.23 ± 0.11	0.36	0.08	3.3	340	421	**793 (520)**	18.4	2.14	0.19	0.40	0.056	323	-
	α	9.01 ± 3.3	2.5 ± 1.32	0.32 ± 0.21	0.02	0.10					4.22	2.55	0.38	<0.001	0.011		
-1.8SFE	γ	13.1 ± 0.8	1.63 ± 0.23	0.26 ± 0.14	0.21	0.05	-0.9	374	396	**788 (515)**	18.5	2.31	0.23	0.22	0.043	350	-
	α	10.2 ± 1.7	1.75 ± 0.23	0.39 ± 0.13	0.02	0.10					4.62	2.62	0.51	<0.001	0.017		
-2.1SFE	γ	15.9 ± 3.1	1.97 ± 0.41	0.38 ± 0.12	0.11	0.01	-0.7	376	-	**833 (560)**	16.0	2.00	0.27	0.14	0.051	371	-
	α	10.9 ± 2.1	2.21 ± 1.10	0.41 ± 0.11	0.02	0.10					4.03	1.99	0.87	<0.001	0.070		
-2.2SFE	γ	13.1 ± 1.4	1.48 ± 0.21	0.43 ± 0.29	0.10	0.04	-2.2	384	357	Only α-martensite was observed in the structure							
	α				-												

*Values determined assuming full partitioning to the γ-austenite in the absence of AlN

4. DISCUSSION

A summary of the property data is shown in Figure 13 relative to the goals set by the U.S. Department of Energy for 3rd generation advanced high strength steel. In terms of ultimate tensile strength and total elongation to failure many of the alloys studied here demonstrate the requisite properties in either the hot band or batch annealed condition. Two of the hot band steels (-0.2 SFE and -1.8 SFE) have properties equivalent to press hardened martensitic steels with ultimate strengths as high as 1840 MPa and total elongation to failure of 12.9%. It should be noted with emphasis that a simple process of hot working and air-cooling obtained these properties. Both the -0.2 SFE and -1.8 SFE steels have the highest Si:Al ratio for the chemistries studied and produced a partially recrystallized microstructure in the hot band condition. The microstructure for these two steels contained mostly (>50%) α-martensite and equal proportions of ε-martensite and γ-austenite. It is reasonable to assume that the mechanical behavior of the hot band steels is dependent upon the ease of recrystallization coming off of the roll mill. As previously noted in literature, silicon [34-36] is thought to exert a drag force upon the growth of recrystallized grains; however, as shown in Figure 10 the addition of Al appears to mitigates this drag effect when present in equal or greater proportion, i.e. Si:Al ≤ 1.0.

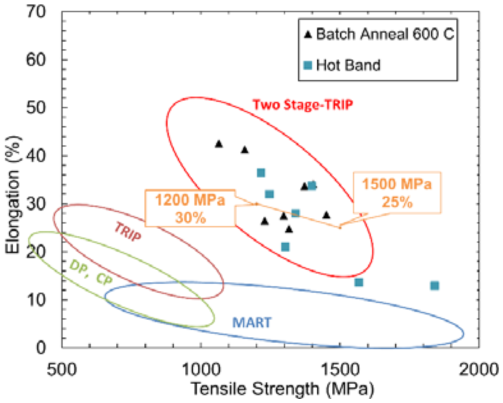

Fig. 13. Population plot of the reported medium manganese steels. DOE targets are shown for 3rd generation advanced high strength steels with designed two-stage TRIP steel behavior outlined within the red oval.

Yield strengths can be increased by microstructural refinement using cold rolling and annealing at 873 K (600 °C) and yield strengths in excess of 700 MPa were obtained when the mean free dislocation path, measured by linear intercept distances of both γ-austenite grain boundaries and athermal martensite interfaces were less than 0.5µm. Here it is interesting to compare the intrinsic stacking fault energies and the resultant Hall-Petch parameters for two types of steels: the TWIP-TRIP steel reported by Lee et al. [17] and the two stage TRIP alloys reported here. An average ISFE for the TWIP-TRIP alloys reported by Lee et al. was calculated using the same thermodynamic parameters used in the study reported here and produced a value of 17.0 mJ/m^2. For the alloys reported here the average ISFE is 2.8 mJ/m^2. A comparison of eq. (1) and the least squares fit for the Hall-Petch plot shown in Figure 7 shows two interesting effects of lowering the ISFE: (1) the Hall-Petch grain boundary hardening parameter increases as ISFE decreases and (2) the intrinsic strength or friction stress (y-axis intercept) decreases with decreasing ISFE. Higher values of the Hall-Petch grain boundary hardening term are often associated with lower ISFE in copper alloyed with aluminum as reported by Rohatgi et al. [58] The higher Hall-Petch grain boundary hardening parameter is often related to ease of dislocation cross-slip and ease of stress relaxation of the grain boundary imposed by dislocation pile-ups. A lower intrinsic stacking fault energy would be expected to reduce cross slip and thus produce a higher Hall-Petch grain boundary hardening parameter. Both TWIP and ε-martensite nucleation are dependent upon nucleation of Shockley partial dislocations, which is dependent upon the unstable stacking fault energy rather than the ISFE. At present, there is no thermodynamic model capable of calculating this value and density functional theory has yet to model these more complicated multi-element alloys. Rohatgi et al. show that the friction stress increases with aluminum addition to copper with a 2/3 power dependence of the alloy concentration. The friction stress of the two-stage TRIP alloys was found to best correlate to the aluminum content of the steel. The friction stress for each alloy was calculated using the average grain boundary strengthening term (393 MPa•μm$^{1/2}$) and the mean free path measured for each alloy. The calculated friction stress plotted against the ½ power dependence of the aluminum concentration (at.%) in the annealed γ-austenite is shown in Figure 14 along with the alloys reported by Lee et al. [17].

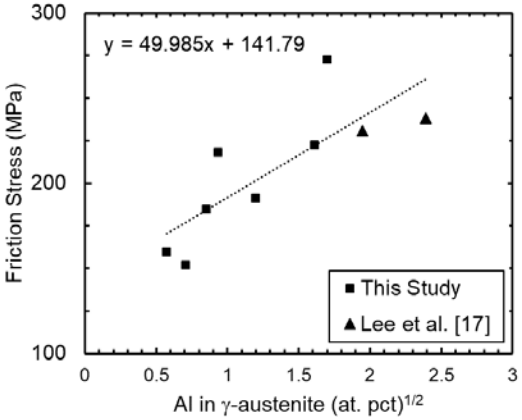

Fig. 14. A linear fit to the friction stress as a function of aluminum concentration (at. pct.) to the ½ power of the alloys investigated in this study and the alloys reported by Lee et al [17] for reference in the regression analysis. The 13.0 SFE alloy was excluded due to the bimodal grain structure and the exceptionally high friction stress calculated.

The steels that exhibit the TWIP – TRIP effect, alloys 13.3SFE and 13.0SFE, have a higher friction stress 272 MPa and 635 MPa compared to the two-stage TRIP alloys. The distinction between TWIP and ε-martensite is the spacing of partial dislocations; twins require partials on every $\{111\}_\gamma$ plane compared to ε-martensite which requires a partial dislocation on alternating $\{111\}_\gamma$ planes as describe by Olson and Cohen [41]. With fewer required dislocations it is reasonable to believe that ε-martensite formation in the two-stage TRIP steels would have a lower friction stress compared to the TWIP steels.

Remy and Pineau [3], Remy [4], and Allain et al. [5], all stated that ε-martensite will be produced from a stress induced martensitic reaction if the ISFE ≤ 12 mJ/m^2. They also proposed that a combination of TWIP and ε-martensite will occur when the ISFE is between 12 – 25 mJ/m^2, calculated according to the model utilized throughout this work, the results of this work are consistent when considering the ISFE of the γ-austenite formed after annealing. Based on the results from Figure 3 and Table V alloys with ISFE ≥ 11.9 mJ/m^2 using the thermodynamic parameters reported in this work are TWIP – TRIP steels.

The tensile strength and total ductility of the cold worked and annealed alloy was empirically related to the chemistry in eq (7, 8). The 13.3 and 13.0 SFE alloys were excluded from the model because they were observed to exhibit a TWIP-TRIP response. From the results of eq. 7 and 8 it is noted that both carbon and nitrogen have large positive effects on the tensile strength of these two-stage TRIP alloys. Nitrogen also appears to have a negative effect on the total ductility and this dual effect is potentially tied to the DSA response observed in these steels. A summary of the strain aging response of the steels investigated is shown in Table VI with the concentration of Mn, C, and Al in the annealed γ-austenite according to the EDS results. The concentration of carbon and nitrogen in α-ferrite calculated according to the FactSage results and the total α-ferrite measured according to EBSD-OIM are also included in Table VI. Alloys with > 50 vol. pct. α-ferrite (-0.2SFE and -1.8SFE) exhibit both DSA and yield point behavior which according to the work by Field and Van Aken is due to nitrogen pinning of dislocations in α-ferrite. Table VI also identifies these alloys as having the highest concentration of N (> 0.011 wt. pct.) in the α-ferrite and is consistent with the results from Field and Van Aken [1]. Additionally, it was proposed by Field and Van Aken that the DSA in the two-stage TRIP steels can also be caused by Mn trapping at stacking faults or ε-martensite. This is in close agreement to what is observed for the two-stage TRIP 7.8SFE alloy, where DSA is not observed in the initial tensile response when ε-martensite is not present, however at the later strains (> 10 pct. strain) DSA is evident and from Figure 3(a) ε-martensite is also measured within the structure. Field and Van Aken also investigated a two-stage TRIP steel with Cr replacing the conventional aluminum and from this substitution the dynamic strain aging associated with interstitials, from the precipitation of $M_{23}(C,N)_6$, was mitigated. Also noted by Field and Van Aken was ;that DSA arising from Mn interacting with the ε-martensite fault structure still remained. The TWIP – TRIP alloys (13.3SFE and 13.0SFE) however show no evidence of DSA; however, ε-martensite is not observed during the tensile deformation of these steels. This observation corroborates the hypothesis that Mn interacting with ε-martensite is associated with the DSA of the two-stage TRIP steels.

Table VI. Presence of strain aging for the alloys studied with the concentration of the alloying elements which have been shown to cause DSA in the α-ferrite and γ-austenite. Volume fraction of α-ferrite is also shown after intercritical annealing from EBSD-OIM measurements

			Concentration in γ-austenite (wt. pct.)			Concentration in α-ferrite (wt. pct.)		
Alloy	DSA	Yield Point	Al	Mn	C*	α-ferrite	$C^{\#}$	$N^{\#}$
13.3 SFE	None	None	1.45	18.0	0.12	0.31	<0.001	0.008
13.0 SFE	None	None	1.25	12.4	0.33	0.19	<0.001	0.002
7.8 SFE	Late Stage	None	1.42	16.8	0.12	0.40	<0.001	0.007
5.0 SFE	Strong DSA	None	0.72	16.3	0.17	0.03	<0.001	0.005
-0.2 SFE	Strong DSA	Yes	0.23	12.3	0.36	0.58	<0.001	0.011
-1.8 SFE	Strong DSA	Yes	0.26	13.1	0.21	0.53	<0.001	0.017
-2.1 SFE	Strong DSA	None	0.38	15.9	0.11	0.08	<0.001	0.007
-2.2 SFE	Strong DSA	None	0.43	13.1	0.10	0.00	-	

* Values calculated assuming full partitioning to the γ-austenite,

[#] Values calculated using FactSage 7.0 using the FSstel database

Microstructural constituents also have a strong effect on the total ductility of the steel. The product of the volume change for the martensitic transformations and the total transformable components correlated well with the total ductility of the steels designed to undergo the γ→ε→α TRIP sequence upon loading, as shown in Figure 12. Of note, however, are the Batch Annealed alloys 5.0, -2.1, and -2.2 SFE alloys exhibiting behavior similar to the hot band steels. This effect is tied to the starting structure of those alloys with there being a low concentration of α-ferrite (< 8 vol. pct.) in the starting structure as shown in Table VI. It has been shown that the α-martensite that forms from the strain induced transformation is hard and brittle [17], this brittle α-martensite will not contribute significantly to the total ductility. The three two-stage TRIP alloys containing significant α-ferrite in the starting structure (7.8, -0.2, and -1.8 SFE) exhibit increased ductility and this is potentially due to the deformation of the α-ferrite. Theoretically the y-intercept of the two equations would be the ductility of the steel without γ-austenite or ε-martensite. In the hot band steels this is 0.8 pct. strain and for the fresh α-martensite this is a reasonable value, from Figure 2(a) post necking ductility was limited to 1-2 pct. strain if occurring. The α-ferrite in the batch annealed condition however contributes 20.5 pct. strain to the ductility. Both data sets exhibit a similar slope associated with the volume transformation and the slope indicated that the two consecutive martensitic reactions contribute to the total elongation of the steels as ~0.13 times the product of the volume change during transformation and the percent of the phase transforming.

Aluminum's complicated effect on the dynamic recrystallization of the hot-band steels can also be related to the γ-austenite stability and is attributed to the difference in the Ms temperatures ($\Delta Ms = Ms^{\varepsilon} - Ms^{\alpha}$) temperature as discussed by Field et al. [32]. They showed in steels exhibiting ε-martensite that the difference in Ms temperatures correlated strongly to the total amount of retained γ-austenite. Aluminum will suppress the Ms^{ε}, as shown by Pisarik and Van Aken [31], and increases Ms^{α}, according to the work by Field et al. [32], this drives the ΔMs to be more negative and leads to greater retained γ-austenite in the room temperature microstructure. In contrast silicon had a very weak effect on both Ms temperatures according to those works [31,32], and it can be seen in Figure 15 that there is also a decrease in the γ-austenite content with an increase in the Si:Al ratio.

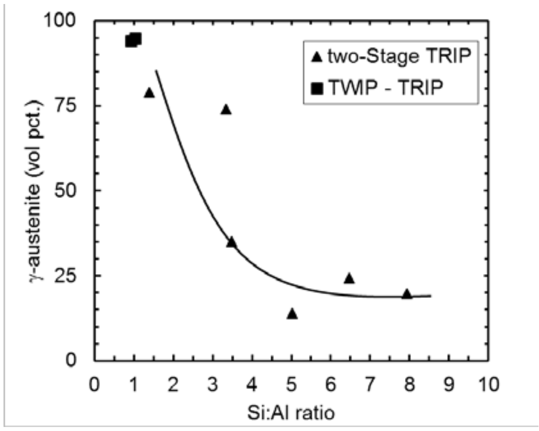

Fig 15. Effect of Si:Al ratio on the γ-austenite content of the hot band medium-Mn steels investigated in this study

From these results and the best understanding of the two-stage TRIP steels accorded by this investigation, as well as previous works on medium-Mn two-stage TRIP systems [1,32] two additional alloys were cast and processed in a manner described in the experimental procedure of this paper. The composition, bulk ISFE, and Ms temperatures are listed in Table VII. Silicon content was reduced to ~1 wt. pct. to improve recovery and recrystallization in the hot band condition. Chromium was added in sufficient quantity to produce $M_{23}(C,N)_6$ precipitation and thus mitigate dynamic strain aging associated with interstitials. One alloy was also alloyed with aluminum to investigate if the elevated ISFE of 10.6 mJ/m^2 would provide the two-stage TRIP response. These alloys are designated Cr and Cr+Al. The hot band microstructures and tensile properties of the Cr and the Cr + Al alloys are shown in Figure 16 along with tensile results from the NXG^{TM}1200 steel produced by AKSteel and NanoSteel [59]. It is noted that the Cr alloy contains a significant volume fraction of ε-martensite (47 vol. pct.) and this is understood to be due to the elevated Ms^{ε} temperature (376 K). The Cr alloy also exhibits continuous DSA over the entire strain range of the tensile test whereas the Cr+Al begins to show DSA at the start of the tensile curve inflection in a similar fashion to the NXG^{TM}1200 steel. The greater magnitude of the ΔMs calculated for the Cr + Al compared to the Cr alloy is expressed in a primarily austenitic structure after rolling (98 vol. pct.). After cold rolling and annealing at 923K (650 °C) for 20 hours the precipitation of the $M_{23}(C,N)_6$ and NbC is calculated using the FactSage thermodynamic software package and the ISFE of the γ-austenite is altered from the single phase composition value as calculated in Table VII. Specifically the Cr, C, and N contents are reduced and the volume fraction of carbides and the ISFE of the γ-austenite is recalculated utilizing the multiphase equilibria from FactSage with the values shown in Table VIII. Precipitation of $M_{23}(C,N)_6$ during annealing produces a lower ISFE and increases the ε-martensite start temperature in each alloy, which is most significant for the Cr+Al alloy that now shows ε-martensite in the annealed microstructure. The tensile properties and microstructure of the cold rolled and annealed alloys are shown in Figure 17. The tensile response of the Cr alloy is little changed from the hot band condition; however, an increased yield strength and improved ductility is demonstrated in the Cr+Al alloy and shows remarkable similarity to the NXG^{TM}1200 steel.

.

Table VII. Composition and calculated thermodynamic parameters of the second iteration of two-stage TRIP alloys.

Alloy	**Composition (wt. pct.)**							**Calculated Parameters***			
	C	Mn	Si	Cr	Al	N	Nb	SFE mJ/m^2	Ms$^{\varepsilon}$ K (°C)	Ms$^{\alpha}$ K (°C)	ΔMs (C°)
Cr	0.16	13.9	1.1	3.3	0.03	0.016	0.042	-0.9	376 (103)	493 (219)	-116
Cr + Al	0.17	14.0	1.2	3.2	1.6	0.033	0.051	10.6	269 (-4)	505 (232)	-236

* Values calculated for a single phase γ-austenite

Table VIII. Composition and calculated thermodynamic parameters of the γ-austenite from multiphase equilibria simulation using FactSage

	γ-austenite									**Carbides (wt. %)**	
Alloy	Composition (wt. pct.)						SFE (mJ/m^2)	Ms$^{\varepsilon}$ K (°C)	Ms$^{\alpha}$ K (°C)	$M_{23}(C,N)_6$	NbC
Cr	0.06	13.8	1.1	2.5	-	0.005	-4.6	400 (127)	416 (143)	1.78	0.076
Cr + Al	0.07	13.9	1.2	2.3	1.5	<0.001	6.6	301 (28)	441 (168)	1.81	0.048

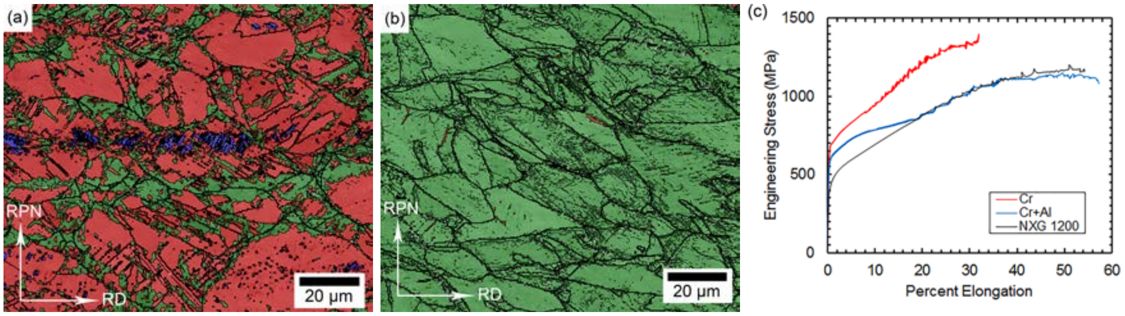

Fig. 16. EBSD-OIM maps of the hot band (a) Cr alloy, (b) Cr + Al alloy and (c) tensile response of the hot band two-stage TRIP alloys with the NXG^{TM} 1200 alloy for comparison. Austenite is shown in green, ε-martensite is red and the α-martensite is blue.

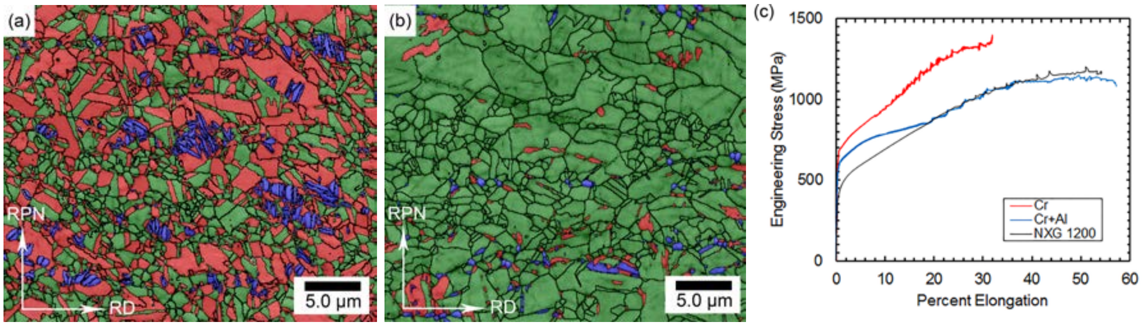

Fig. 17. EBSD-OIM maps of the cold worked and annealed (a) Cr alloy, (b) Cr + Al alloy and (c) tensile response of the cold worked and annealed two-stage TRIP alloys with the NXG^{TM} 1200 alloy for comparison. Austenite is shown in green, ε-martensite is red and the α-martensite is blue.

5. CONCLUSION

A methodology for designing two stage TRIP alloys has been presented using thermodynamic calculations of intrinsic stacking fault energy and martensite start temperatures for both ε and α martensites. Ideally the start temperature for ε-martensite is kept near ambient temperature with the α-martensite temperature being 100 to 200K greater than that of the ε-martensite. Chromium should be added in sufficient quantity, precipitated as $M_{23}(C,N)_6$ during the 600°C anneal, to mitigate dynamic strain aging associated with interstitial carbon in γ-austenite or nitrogen in α-ferrite as shown previously by the authors in reference 1. Addition of Nb, precipitated as NbC during hot rolling, is used in conjunction with annealing at 600°C after cold rolling to obtain a fine grained austenite with desired yield strengths greater than 500 MPa. Aluminum, silicon and manganese additions are balanced to encourage the following: (1) recrystallization during thermomechanical processing to produce an equiax austenite grain size on the order of 1-2μm, i.e. Si:Al~1.0 (2) addition of aluminum increases solid solution strengthening, (3) an γ-austenite composition after the 600°C anneal with an intrinsic stacking fault energy for two-stage TRIP, i.e. ISFE ≤ 10.5 mJ/m^2, and (4) the requisite start temperatures to maximize the γ-austenite content in the steel that leads to a two-stage TRIP response. Nearly all of the steels investigated exhibit strength and ductility in excess of the break through targets for future 3rd generation advanced high strength steel. Total ductility was correlated to the product of the volume change and the total volume percent of the TRIP components in the starting microstructure for the two-stage TRIP steels in both the hot band and batch annealed condition. Design of two-stage TRIP steels using intrinsic stacking fault energy and martensite start temperatures determined from the chemistry of austenite has proven to be a reliable to provide the required properties for future 3rd generation advanced high strength steels with strength and ductility defined by the department of energy.

Acknowledgements

This work was supported by the Peaslee Steel Manufacturing Research Center (PSMRC). Companies directly involved in this work include AK Steel, ArcelorMittal, Nucor Steel, and U. S. Steel. The FEI Helios NanoLab dual beam FIB was obtained with a Major Research Instrumentation grant from the National Science Foundation under contract DMR-0723128. The FEI Tecnai F20 scanning/transmission electron microscope was obtained through a major research instrumentation grant from the National Science Foundation under contract DMR-0922851. The authors also acknowledge the support of the Materials Research Center and in particular Dr. Clarissa Wisner for training on the SEM, Dr. Jingjing Qing's assistance in operation of the TEM was instrumental in the requisite research as well as Dr. Eric Bohannan for performing the XRD work. Special

thanks are also extended to Dr. Narayan Pottore and Dr. Bernard Chukwulebe at ArcelorMittal, Todd Link from U.S. Steel, Eric Gallo at Nucor, and Dr. Luis Garza from AK Steel for their discussion and guidance on the engineering requirements for future 3rd generation advanced high strength steels.

References

[1] D.M. Field and D.C. Van Aken, *Proceedings of the Intl. Symp. on New Developments in Advanced High-Strength Steels,* Keystone, Colorado, 2017

[2] G. Frommeyer, U. Brux, and P. Neumann, *ISJ Inter*. 2003, vol. 43, pp. 438-446

[3] L. Remy, and A. Pineau *Mater. Sci and Eng.* 1976, vol. 26 pp. 123-132

[4] S. Allain, J.P. Chateau, and O. Bouaziz, *Mater Sci and Eng.* 2004, vol. 387, pp. 143-147

[5] T.H. Lee, E. Shin, C.S. Oh, H.Y. Ha, and S.J. Kim, *Acta Mater.* 2010, vol. 58, 3173-3186

[6] Q. Li, Xu. Huang, and W. Huang: *Met Sci. Eng.*, 2016, vol. 662, pp. 129-135.

[7] E.J. Seo, L. C, Y. Estrin, and B.C. De Cooman, *Acta Materialia*, 2016, vol. 113, pp. 124-139

[8] L. Cho, E.J. Seo, and B.C. De Cooman, *Scripta Materialia*, 2016, vol. 123, pp. 69-72

[9] T. Tschiyama, T. Inoe, J. Tobata, D. Akami, and S. Takaki, *Scripta Mat.* 2016, vol. 122, pp. 36-39

[10] D-W. Suh, S-J Park, T-H. Lee, C-S. Oh, and S-J. Kim, *Met Trans A*, 2010, vol. 41A, pp. 397-408

[11] D-W. Suh, J-H Ryu, M-S. Joo, H-S Yang, H.K.D.H. Bhadeshia, *Met Trans A*, 2013, vol. 44A, pp. 286-293

[12] J. Shi, X. Sun, M. Wang, W. Hui, H. Dong, and W. Cao, *Scripta Mat,* 2010, vol. 63, pp. 815-818

[13] Z.H. Cai, H. Ding, R.D.Misra, and Z.Y. Ying, *Acta Materialia*, 2015, vol. 84, pp. 229-236

[14] R. Zhang, W.Q. Ca, Z.J. Peng, J. Shi, H. Dong, and C.X. Huang, *Mater. Sci. & Eng. A*, 2013, vol. 583, pp. 84-88

[15] Y. Zhang, L. Wang, K. O. Findley, and J. Speer, *Met Trans. A*, 2017, vol. 48A, pp. 2140-2149

[16] H. Luo, H. Dong, and M. Huang, *Mater. & Design,* 2015, vol. 83, pp.42-48

[17] S. Lee, W. Woo, and B.C. De Cooman, *Met. Trans A*, 2016, vol. 47A, pp. 2125-2140

[18] H. Song, S.S. Sohn, J-H Kwak, B-J lee, and S. Lee, *Met Trans A*, 2016, vol. 47A, pp.2674-2685

[19] O. Grässel, L. Krüger, G. Frommeyer, and L.W. Meyer: *International Journal of Plasticity*, 2000, vol. 16, pp. 1391-1409

[20] M.C. McGrath, D.C. Van Aken, N.I. Medvedeva, and J.E. Medvedeva, *Metall. Mater. Trans. A*, Vol. 44A, 2013, pp. 4634-4643.

[21] D.C. Van Aken, S.T. Pisarik, and M.C. McGrath, *Proceedings of the Intl. Symp. on New Developments in Advanced High-Strength Steels*, Vail, Colorado, 2013, pp. 119-129.

[22] S.T. Pisarik, D.C. Van Aken, K.Limmer, and J.E. Medvedeva, *AIST2014 Proceedings*

[23] D. M. Field, and D.C. Van Aken, *Met Trans A.*, (2016) Vol. 47A pp.1912-1917

[24] S.J. Lee, S.W. Lee, B.C. De Cooman: *Int. J. Mater. Res.*, 2013, vol. 104, pp. 423–29.

[25] X-S. Yang, S. Sun, H-H Ruan, S-Q Shi, and T-Y. Zhang, *Acta Materialia*, 2017, vol. 136, pp. 347-354

[26] B.C. De Cooman, P. Gibbs, S. Lee, and D.K. Matlock, *Met Trans A*, 2013, vol. 44A, pp. 2563-2572

[27] S.K. Huang, Y.H. Wen, N.Li, J.Teng, S.Ding, Y.G. Xu, *Mater Characterization* vol.59, 2008, pp.681-687

[28] S. Shin, M. Kwon, W. Cho, I. S. Suh, and B.C. De Cooman, *Mater. Sci. & Eng.* 2017, vol. 683, pp. 187-194

[29] Medvedeva, N.I, M.S Park, D.C. Van Aken, and J.E. Medvedeva, *J. Alloys Compd.*, Vol. 582, 2014, pp. 475-482

[30] K.R. Limmer J.E. Medvedeva, D.C. Van Aken, N.I. Medvedeva *Computational Materials Science,* DOI: 10.1016/j.commatsci.2014.12.015

[31] S.T. Pisarik and D.C. Van Aken, *Met Trans A.*, Vol. 47A 2016 pp1009-1018

[32] D.M. Field, D.S. Baker, and D.C. Van Aken, *Met Trans A*, 2017, DOI. 10.100/s 11661-017-4020-2

[33] R. Skolly, ArcelorMittal personal communication.

[34] P.P. Suikkanen, V.T.E. Lang, M.C.Somani, D.A. Prter, and L.P. Karjalainen: *ISIJ International*, 2012, vol. 52, pp. 471-476

[35] Z, Li-Juan, W. Di, and Z. Xian-ming: *Jour. Iron and Steel research international*, 2007, vol. 14, pp. 61-65

[36] L.J. Zhu, D. Wu, X.M. Zhao *Acta Metall*. 2008 vol. 21, pp. 163-168

[37] M.C. Somani, L.P. Karjalainenm D.A. Porter, and R.A. Morgridge: Proc. Int. Conf. on Thermomechanical Processing Mechanics: Microstructures and Controls, University of Sheffield, Sheffield GB, (2003), 436.

[38] S.F. Medina, and J. E. Mancilla, *ISIJ Int.* 1996, vol. 36, pp.1036-1070

[39] S.F. Medina, and A. Quispe: *ISIJ Int.* 2001, vol. 41, pp.774-780

[40] S-J. Lee, J. Kim, S.N. Kane, and B.C. De Cooman, *Acta Materialia*, 2011, vol. 59, pp.6809-6819

[41] G.B. Olson, M. Cohen *Met Trans A* Vol 7 1976 pp. 1897-1904

[42] ASTM E 8/E 8M-08, Standard Test Methods for Tension Testing of Metallic Materials

[43] S. Martin, C. Ullrich, D. Simek, U. Martin, and D. Rafaja, *J. Appl. Crystallogr.*, 2011, vol. 44, pp. 779-787

[44] N. Stanford and D.P. Dunne *Acta Materialia*, 2010, Vol. 58, pp.6752-6762

[45] S. T. Pisarik, and D. C. Van Aken, *Met Trans A.*, 2014, vol. 45, pp. 3173-3178

[46] M. Papa Rao, V. Subramanya Sarma, and S. Sankaran *Met Trans A* 2014, vol 45A pp. 5313-5317

[47] M. Papa Rao, V. Subramanya Sarma, and S. Sankaran *Mater. Sci. & Eng. A* 2013, vol 568 pp. 171-175

[48] O. Saray, G. Purcek, I. Karaman, H. Maier, *Met Trans A* 2012, vol. 43A. 4320-4330

[49] V.S.A. Challa, R.D.K. Misra, M.C. Comani and Z.D. Wang, *Mater. Sci. & Eng* 2016 vol. 661 pp.51-60

[50] Y. Son, Y.K. Lee, K-T Park, C. S. Lee, and D. H. Shin *Acta Materialia* 2005, vol. 53, pp. 3125-3134

[51] M. Calcagnotto, Y. Adachi, D. Ponge, and D. Raabe *Acta Meterialia* 2011, vol. 59 pp. 658-670

[52] D. H. Shin, and K-T. Park, *Mater. Sci. & Eng. A* 2005, vol. 410-411, pp. 299-302

[53] M. Calcagnotto, D. Ponge, E. Demir, and D. Raabe, *Mater. Sci. & Eng. A* 2010 vol. 527, pp. 2738-2746

[54] R.D.K. Misra, P.K.C. Vankatsurya, M.C. Somani, and L.P. Karjalinen, M*et Trans A*, 2012, vol. 43A, pp. 5286-5297

[55] P.J. Gibbs, E. De Moor, M.J. Merwin, B. Clausen, J.G. Speer, and D.K. Matlock, *Met Trans A*, 2011, vol. 42A, pp. 3691-3701

[56] G. Dini, A. Najafizadeh, R. Ueji, and S.M. Monir-Vaghefi, *Materials Letters*, 2010, vol. 64, pp. 15-18

[57] S. Rajasekhara, P.J. Ferreira, L.P. Karjalainenm and A. Kyröläinen, *Met Trans A.* 2007, vol. 38A, pp. 1202-1210

[58] A. Rohatgi, K.S. Vecchio, and G.T. Gray III, *Met Trans A*, 2001, vol. 32A, pp.135-145

SECTION

3. CONCLUSION

A new composition based method for calculating the chemical driving force of the γ→α transformation, $\Delta G_{Chem}^{\gamma\rightarrow\alpha}$, using a regular solution model has been used to predict the strain energy necessary to overcome for the formation of α-martensite. A composition and temperature dependent strain energy $\Delta G_{Str}^{\gamma\rightarrow\alpha}$ has been proposed for the formation of α-martensite, and by setting $\Delta G_{Chem}^{\gamma\rightarrow\alpha} + \Delta G_{Str}^{\gamma\rightarrow\alpha} = 0$, an M_S^{α} can be determined. The role of the chemical dependent Young's modulus, lattice misfit, and molar volume is important in providing a unified expression between $\Delta G_{Chem}^{\gamma\rightarrow\alpha}$ and M_S^{α} for both lath and plate martensites. The model has an uncertainty of ± 100K (100 C°), but within this uncertainty the model has explanatory power for the microstructures observed in mid-manganese steels. The model is limited in its ability to predict α-martensite to compositions less than 15wt. pct. Mn. Processing history was also shown to play a role in the prediction of ε-martensite and that using a larger n=8 value for the ε-martensite embryo size can provide better correlation to the observed microstructure.

Utilization of the thermodynamic model to produce a Cr modified alloy was successful and it was shown to be a two-stage TRIP steel with a significantly reduced DSA response during tensile testing. The reduction in DSA was attributed to the formation of $M_{23}(C,N)_6$.

Nearly all of the steels investigated exhibit strength and ductility in excess of the break through target for future steels in the batch annealed condition. The two-stage

TRIP phenomenon can be obtained in steels with γ-austenite formulated to have an ISFE $\leq$ 10.5 mJ/m^2. It was observed that the tensile behavior of the hot-band can be related to the silicon to aluminum ratio and the degree of recrystallization in the microstructure. Total ductility was correlated to the product of the volume change and total TRIP components in the starting structure for the two-stage TRIP steels in both the hot band and batch annealed condition. The empirical model of properties based on chemistry has been shown to be reliable within the compositional range for bulk chemistry of the batch annealed two-stage TRIP alloys.

4. PROPOSED FUTURE ALLOYS

A series of compositions, based upon previous two-stage TRIP alloys, was investigated to obtain a primarily austenitic microstructure in the hot band condition. The proposed chemistries were each formulated to obtain a ΔM_s value of -96 ± 4 C° in the single-phase austenite for the hot-rolled product that assumes a finishing temperature of 950 °C (~1750 °F) followed by slow cooling to mimic a hot-band coil. A chromium containing series is suggested due to the inherent issues of castability associated with elevated aluminum contents. Three potential two-Stage TRIP alloys are shown in Table I with values given in wt. %; calculated room temperature stacking fault energy (SFE), and Ms temperatures for the ε, and α martensites are also shown for a single-phase homogeneous γ-austenite cooled to room temperature. Intercritical annealing or batch annealing is expected to reduce the carbon in the austenite as a result of $M_{23}C_6$ precipitation. FactSage was used to estimate the austenite chemistry during intercritical annealing and the FactSage results were calibrated relative to the observed microstructures of eight previous alloys after cold work and batch annealing at 600°C (1112°F) for 20 hours. Reasonable agreement was obtained between batch annealed microstructures at room temperature and FactSage predictions of austenite compositions at 525 ± 10 °C. Microstructural optimization was conducted based upon γ-austenite chemistry as predicted by FactSage at 525°C and calculated values of SFE, Ms^{ε}, and Ms^{α}. Alloy 2 is recommended for future investigation and the rationale is explained in greater detail below.

As reported in literature, alloying with Si, Al, and Cr promote the formation of hexagonal ε-martensite. [8, 14, 15, 50] Aluminum addition is beneficial with respect to recrystallization during hot rolling; however, these aluminum-containing alloys are more difficult to continuously cast. Furthermore, alloys with high Si show significant resistance to recrystallization during hot-working as shown in Figure 4.1. Chromium appears to be a suitable replacement for Al as shown by the work of Limmer et al., [8] since the unstable stacking fault energy is reduced in a similar fashion to the addition of either Si or Al. In addition, Cr has the benefit of reducing static strain aging, yield point elongation and dynamic strain aging [50].

It is also desired that the proposed alloy be flexible enough to produce either plate for military armor or automotive sheet. Missouri S&T high strain rate testing on two-stage TRIP alloys has shown a positive strain rate dependence where both the flow stress and the true fracture strain increase with increasing strain rates. These attributes are important for both military armor and crashworthiness of automotive sheet. The proposed alloy should thus be formulated for production as single phase γ-austenite with a fine grained microstructure in the hot rolled plate or as automotive sheet by cold-work and intercritical annealing where a tri-phase microstructure is produced, i.e. $M_{23}(C,N)_6$ to reduce dynamic strain aging of the ferrite formed during intercritical annealing and an γ-austenite composition that would produce the two-stage TRIP behavior.

Chemistry of the γ-austenite, whether as a single phase or tri-phase microstructure, should be formulated to maximize the amount of room temperature γ-austenite or ε-martensite. Past work on manganese alloys containing more than 13 wt. % Mn suggests that the difference in martensite start temperatures between Ms^{ε} and Ms^{α} should be negative to obtain higher volume fractions of austenite as shown in Figure 4.2.

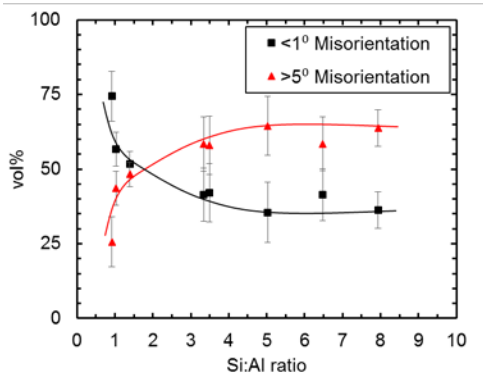

Figure 4.1. The state of deformation measured according to EBSD, volume fraction of grains with internal misorientation both >5° and <1° are determined by the mean angular distribution as a function of silicon to aluminum ratio.

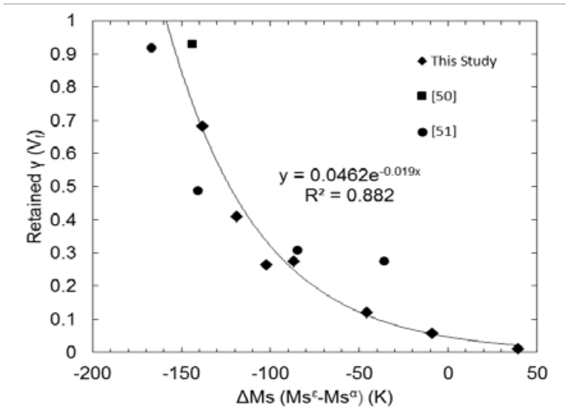

Figure 4.2. Volume fraction of retained austenite at room temperature showing that formation of α-martensite prior to ε-martensite is beneficial in retaining austenite.

An iterative process was used to formulate three potential alloys for investigation. Table 4.1 shows the chemistry of the potential alloys with the calculated values of SFE, Ms^{ε}, Ms^{α}, and the difference in martensite start temperatures as $\Delta Ms = Ms^{\varepsilon} - Ms^{\alpha}$. The effect of Cr, Mn, and Si on the ΔMs with C and N fixed at 0.15 and 0.003 wt. % respectively is shown in Figure 4.3.

Table 4.1. Composition, calculated stacking fault energy and calculated start temperatures for ε and α martensites, of the three proposed two-Stage TRIP alloys.

Alloy	**Composition (wt. pct.)**						**Calculated Parameters***			
	Mn	**Si**	**Cr**	**C**	**N**	**Nb**	**SFE mJ/m^2**	**Ms^{ε} (°C)**	**Ms^{α} (°C)**	**ΔMs (C°)**
1	14.5	1	1	0.20	0.003	0.05	-2.1	111	203	-92
2	13.75	1	3	0.15	0.003	0.05	-1.3	106	203	-97
3	13.0	1	5	0.10	0.003	0.05	-0.4	101	200	-99

**Calculated values assumed a homogeneous, single-phase γ-austenite*

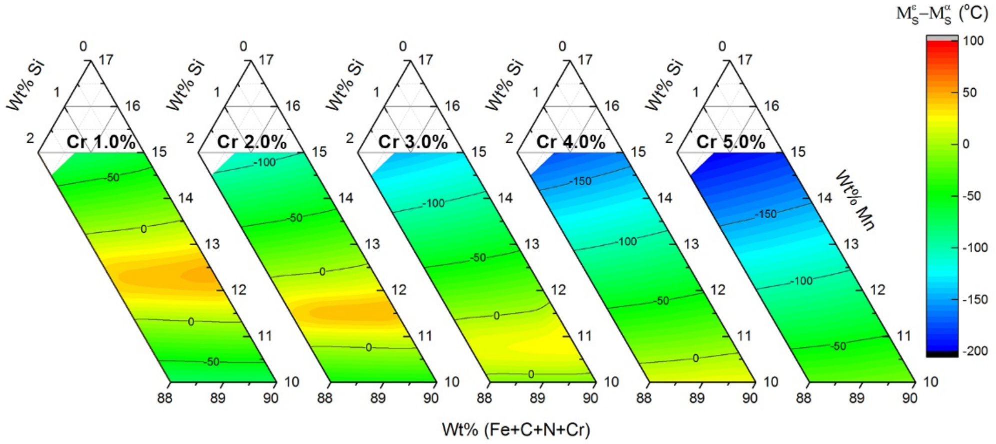

Figure 4.3. Effect of Cr, Mn, and Si on the ΔMs of potential two-Stage TRIP alloys.

Room temperature stacking fault energies were calculated according to the original work of Olson and Cohen [19] using eq. (1) and n=2.

$$SFE(mJ / m^2) = n\rho(\Delta G^{\gamma\rightarrow\varepsilon}) + 2\sigma^{\gamma/\varepsilon} \tag{1}$$

The start temperature for the ε-martensite was calculated by determining the temperature at which SFE = 0 mJ/m^2 for the case of n = 4 [62]. The M_S^α was calculated according to the work of Field et al. [63], where the strain energy of transformation, $\left(\Delta G_{Str}^{\gamma\rightarrow\alpha}\right)$ was balanced against the chemical driving force $\left(\Delta G_{Chem}^{\gamma\rightarrow\alpha}\right)$ according to eq. (2) and eq. (3).

$$\Delta G_{str} + \Delta G_{chem}^{\gamma\rightarrow\alpha} = 0 \tag{2}$$

$$\Delta G_{str}(J / mol) = E\Omega\delta^2(14.8 - 0.13T) \tag{3}$$

where $\Delta G_{Chem}^{\gamma\rightarrow\alpha}$ is calculated according to a modified regular solution model described by Field et al. [63]. Ω is the molar volume for iron, and δ is the lattice misfit between the γ-austenite and α-martensite. Single-phase ΔMs values were held constant at -96 ± 4 C° based on results from the initial two-stage TRIP trials. The composition, Ms temperatures, and microstructural components of a previously produced Al-containing, two-stage TRIP, steel and the most recent Cr-containing alloy of interest are shown in Table 3.2, and these alloys shall be designated according to their room temperature SFE for a single phase γ-austenite microstructure.

Table 4.2. Composition, calculated stacking fault energy and calculated start temperatures for ε and α martensites. Volume fractions of phases determined from XRD of hot band alloys, α denotes α-martensite.

Alloy	**Composition (wt. pct.)**						**Calculated Parameters***			**Vol % Phase**		
	Mn	**Si**	**Al**	**Cr**	**C**	**N**	**Ms^{ε} (°C)**	**Ms^{α} (°C)**	**ΔMs (C°)**	**γ**	**ε**	**α**
7.8 SFE	15.1	1.95	1.40	-	0.08	0.017	42	154	-112	79	0	21
0.7 SFE	11.9	1.2	-	4.6	0.17	0.043	93	194	-101	62	24	14

***Calculated values assumed a homogeneous, single-phase austenite*

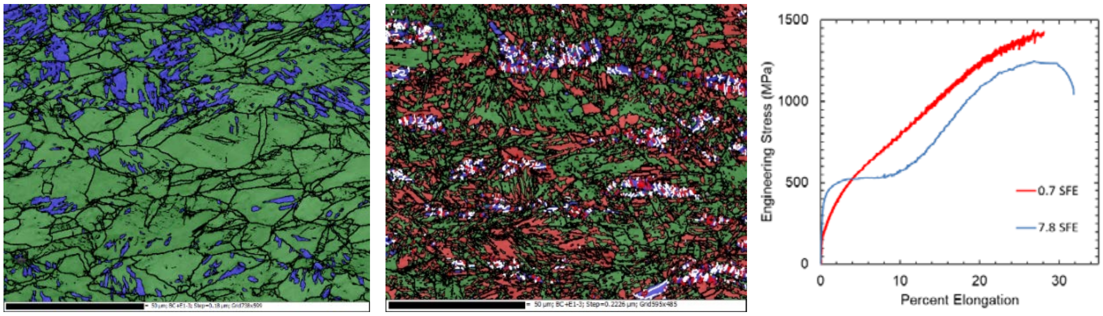

(a) (b) (c)

Figure 4.4. Hot band EBSD microstructure of the (a) 7.8 SFE alloy and the (b) 0.7 SFE alloy, where green is γ-austenite, red is ε-martensite and blue is α-martensite. (c) tensile tests of the hot band 7.8 and 0.7 SFE alloy.

When comparing the 7.8 SFE and 0.7 SFE the ΔMs are within 11 C° and the amount of retained austenite is very similar. It can also be seen that the 7.8 SFE alloy has a more negative ΔMs value (-112 C°) and contains a larger volume fraction of γ-austenite in the hot band structure compared to the 0.7 SFE alloy. Field et al. [63] demonstrated that having a higher Ms^{α} temperature than Ms^{ε} is beneficial in retaining γ-austenite. This phenomenon was explained by comparing the minimum required defect size for the critical nuclei for α-martensite ($n = 14$) and ε-martensite ($n = 4$). Initial formation of α-martensite (n > 14) will use up the easy nucleating sites for ε-martensite (n > 4) reducing the amount of transformed γ-austenite. Segmenting of the austenite by α-martensite has the added benefit of constricting the growth of subsequent ε-martensite laths and thus reducing the volume transformation from a single ε-martensite nucleus. Total ε-martensite formed can also be related to Ms^{ε} as shown in Figure 4.4(b) and comparison with the XRD results reported in Table 4.2. The higher Ms^{ε} temperature of 93 °C in the 0.7 SFE alloy produces 24% ε-martensite compared to 0% ε-martensite produced in the 7.8 SFE steel with an Ms^{ε} temperature of 42 °C.

Addition of Nb and Cr are expected to decrease the stability of the austenite through the formation of NbC and $M_{23}C_6$ carbides. FactSage 7.0™ with the FSstel database was utilized to understand the solidification path, solvus temperatures of NbC and $M_{23}C_6$, and the composition of the intercritical γ-austenite for the alloys proposed in Table 5.1. The solidification range (calculated according to a Schiel segregation model using the 15% liquid as the solidus), A_3 temperature, and solvus temperatures for the $M_{23}C_6$ and NbC are shown in Table 4.3.

Table 4.3. Solidification range, and solvus temperatures for the α-ferrite and carbides.

Alloy	**Solidification Range (C°)**	**Solvus Temperature (°C)**			
		α-ferrite	**$M_{23}C_6$**	**M_7C_3**	**NbC**
1	76	575	607	658	1240
2	68	570	750	-	1200
3	57	579	770	-	1150

All three alloys have solidification ranges greater than 50 C°, which are expected to encourage long metallurgical lengths during continuous casting. Furthermore, FactSage does not predict any α-ferrite at the intercritical annealing temperature of 600 °C for the proposed alloys. The solvus temperature for the $M_{23}C_6$ is significantly lower in Alloy 1 than the other two alloys; however, this resulted from the formation of an M_7C_3 carbide associated with the higher carbon content. M_7C_3 was not predicted in the other two alloys. Thus, Alloy 1 is excluded from further consideration as it may not have the desired effect of reducing nitrogen by precipitation of $M_{23}(C,N)_6$ during batch annealing. The phase fraction as a function of temperature for the three proposed alloys is shown in Figure 4.5, the weight fraction of NbC was constant for all three compositions at 0.057 wt. %.

In an effort to predict the transformation characteristics of the austenite formed during batch annealing a study comparing known microstructures in batch annealed materials produced at Missouri S&T were compared to the weight fractions of α-ferrite predicted using FactSage software. In addition, the predicted chemistry of the austenite was compared to the athermal martensite formed as observed after cooling to room temperature. A study of eight alloys suggests a calculation temperature of 525 ± 10 °C (depending upon the alloy system) best fits the experimental results obtained by annealing at 600 °C. This is shown in greater detail in the Appendix. This temperature discrepancy between predicted and observed microstructures is attributed to the non-dilute solution condition for these heavily alloyed Mn-steels and contributions of a magnetic component to thermodynamic equilibrium.

Predicted batch annealed microstructures for the proposed alloys are reported in Table 4.4 showing the austenite composition, calculated SFE, martensite start temperature difference, and phase composition by mass for the austenite. All three alloys show significant manganese enrichment of the austenite and the SFE is negative for all three indicating that the Ms^{ε} is above room temperature. The negative difference in calculated Ms temperatures would suggest that the Ms^{α} is higher than the Ms^{ε}; however, the Field et al. model [63] for the athermal Ms^{α} temperature may not apply to steels with manganese greater than 15 wt. %. A maximum carbon content in the austenite is predicted for Alloy 2. Alloy 3 has almost no carbon in the austenite formed during batch annealing as a result of the elevated chromium content and $M_{23}C_6$ carbide precipitation. This alloy also had the lowest bulk carbon chemistry.

Phase chemistry for γ-austenite, NbC, and $M_{23}C_6$ as a function of process temperature is shown in Figure 4.6 for Alloy 2. The γ-austenite loses both Cr, and C at lower annealing temperatures (< 750 °C) as shown in Figure 4.6(a). It should be noted that both Cr and C are important elements for the SFE of the designed alloys. Figure 4.6(d) shows the effect of annealing temperature on the ΔMs and the expected volume fraction retained γ-austenite based on the composition predicted by the FactSage calculations. Values suggested for the ΔMs are only relative and the weight fraction of retained γ-austenite should be greater than what is calculated from Table 4.4. A higher processing temperature may be necessary to reduce the amount of Mn partitioning, which may encourage the desired two-stage TRIP behavior. A study of annealing temperature will be considered if this alloy is produced.

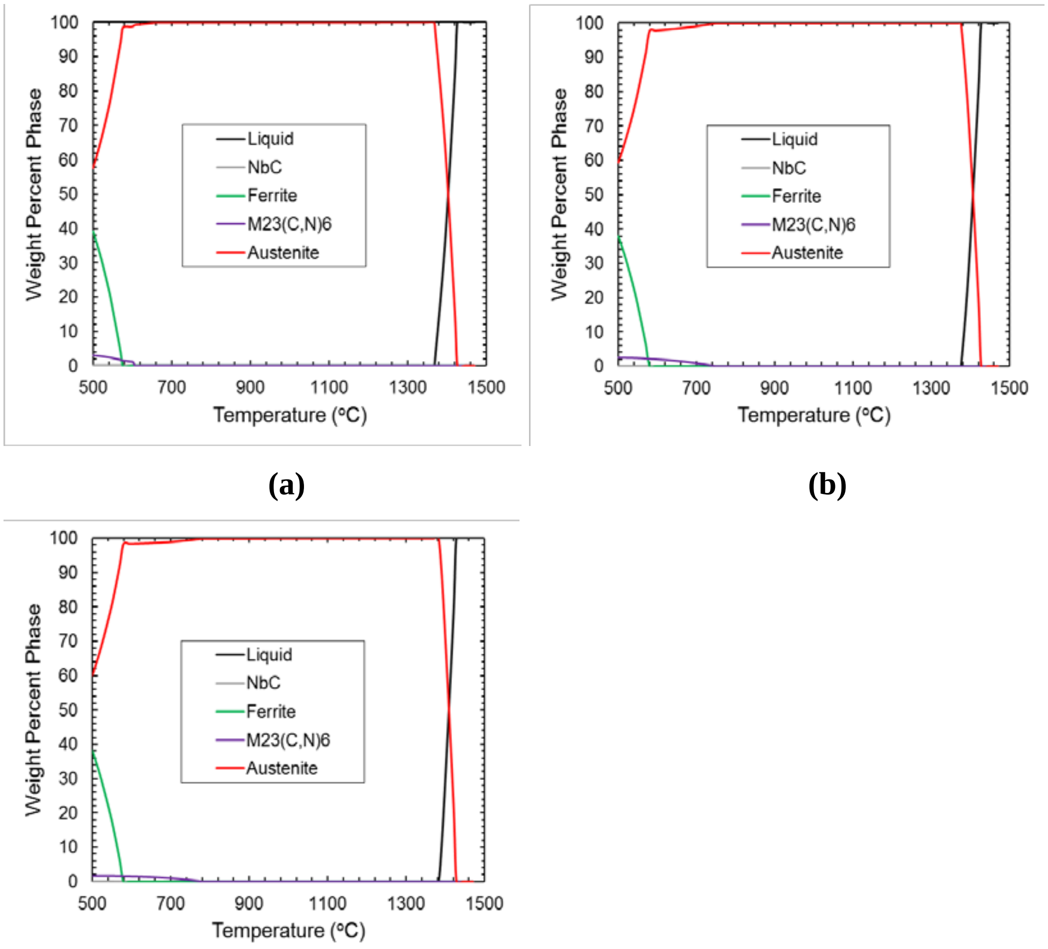

(a) **(b)**

(c)

Figure 4.5. Phases as a function of temperature for the (a) composition 1, (b) composition 2, and (c) composition 3.

Table 4.4. Calculated composition, and calculated ΔMs, of the three proposed two-Stage TRIP alloys, intercritical α-ferrite, and $M_{23}C_6$ is determined from FactSage calculation, at an intercritical annealing temperature of 525 °C. Room temperature γ-austenite content was based on ΔMs calculation

Alloy	Austenite Composition (wt. pct.)					Calculated parameters				
	Mn	Si	Cr	C	N	SFE mJ/m^2	ΔMs (C°)	$M_{23}C_6$ (wt. %)	α-ferrite (wt. %)	γ-austenite (wt. %)
1	17.8	1.02	0.45	0.06	0.001	-3.3	-121	2.8	29	46
2	17.6	1.01	1.85	0.07	0.001	-1.4	-165	2.5	31	50
3	17.0	0.96	4.34	0.001	0.001	-0.6	-172	1.7	32	60

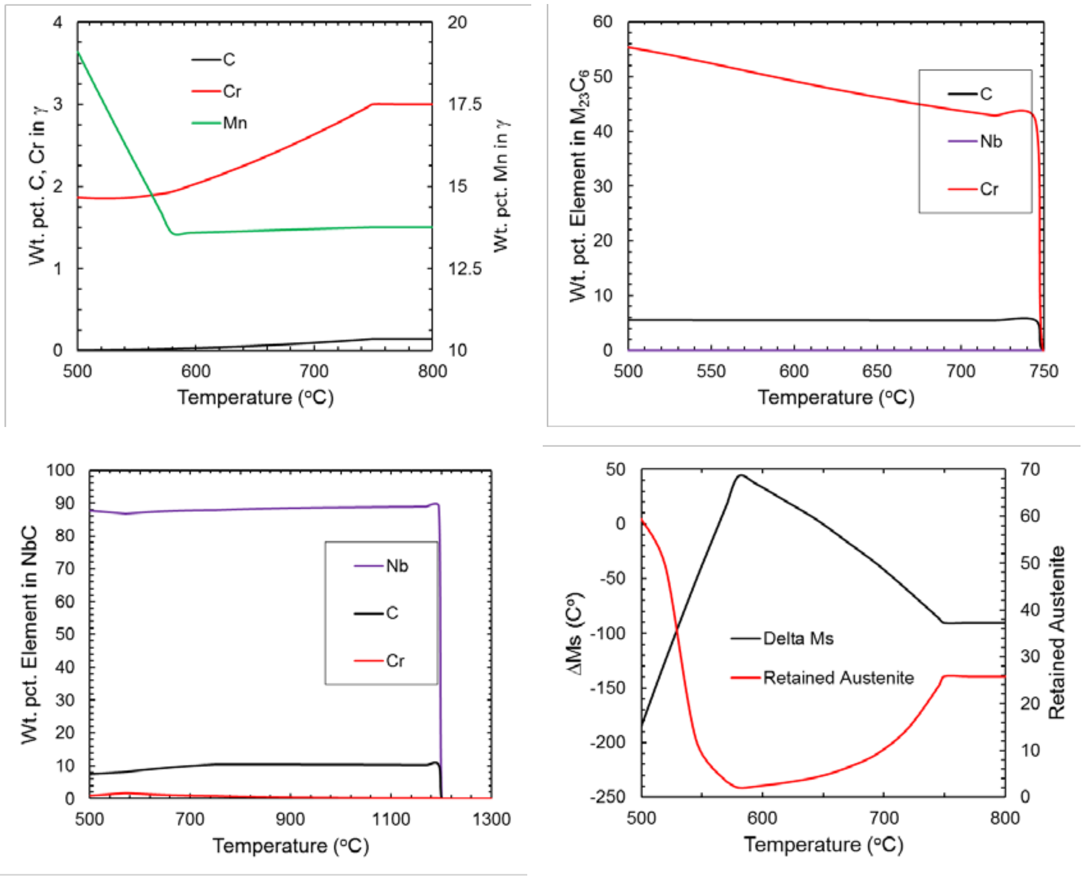

Figure 4.6. Example calculation of the composition of the (top left) γ-austenite, (top right) $M_{23}C_6$, and (bottom left) NbC in Alloy 2. At the lower annealing temperature austenite becomes enriched in Mn however from formation of carbides loses carbon, and chromium. (bottom right) the recalculated ΔMs and expected retained γ-austenite with process temperature.

In summary, Alloy 2 is recommended for study. This alloy can be produced in either a fully austenitic state, combined as austenite and $M_{23}(C,N)_6$ or as a tri-phase combination of ferrite, austenite and $M_{23}(C,N)_6$. In each process condition the austenite should first transform to ε-martensite when mechanically loaded. Flexibility in both phase constitution and phase chemistry will allow a more thorough investigation of the dynamic strain aging observed in these medium manganese steels.

APPENDIX

CALCULATIONS FOR SUGGESTED FUTURE ALLOYS

The following calculations were made to calibrate FactSage predictions for intercritical annealing with the observed batch annealed microstructures for the alloys shown in Table AI. The objective was to determine the best temperature at which these thermodynamic calculations replicate the observed weight fraction of α-ferrite and austenite composition to produce the structures observed. It should be noted that the measured volume percent of α-phase in Table AII is a combination of α-ferrite and α-martensite with the majority being α-ferrite in the batch annealed microstructure. This assumption is based on the morphology of the α-phase which is typically equiaxed, as shown in Figure A1 and Figure A2. Furthermore, it is assumed that the total austenite includes the portion of ε-martensite at the batch annealing temperature. The FactSage temperatures that best matched the 600 °C batch annealed microstructures averaged to be 525 ± 9.6 °C (68%CL).

Table AI. Bulk chemistries of the previously produced two-stage TRIP steels are shown with calculated SFE, calculated Ms$^{\alpha}$, Ms$^{\varepsilon}$, and ΔMs temperatures for single phase austenite.

Alloy	**Composition (wt. pct.)**							**Calculated Parameters***		
	Mn	**Si**	**Al**	**Cr**	**C**	**N**	**Nb**	**Ms$^{\varepsilon}$ (°C)**	**Ms$^{\alpha}$ (°C)**	**ΔMs (C°)**
13.3SFE	13.9	2.07	2.01	-	0.09	0.012	-	-3	117	-120
7.8SFE	15.1	1.95	1.4	-	0.08	0.017	-	42	154	-112
5.0SFE	14.3	2.97	0.89	-	0.16	0.022	-	63	158	-95
-0.2SFE	10.2	2.38	0.3	-	0.17	0.024	-	93	150	-57
-1.8SFE	11.5	2.46	0.38	-	0.11	0.029	-	105	163	-58
-2.1SFE	13.8	2.01	0.4	-	0.1	0.028	-	110	86	24
-2.2SFE	13	1.57	0.45	-	0.1	0.045	-	109	46	63
0.7SFE	11.9	1.2	-	4.6	0.17	0.043	0.045	92	202	-110

**Calculated values assumed a homogeneous, single-phase austenite*

Table IIA. Austenite chemistry as predicted by Factsage for the eight alloys shown in Table IA after adjusting the temperature of calculation to obtain an equivalent α-ferrite content.

	Composition (wt. pct.)					**FactSage**	**Calc. Parameters**		**Measured Phases (vol. %)**		
	Mn	**Si**	**Al**	**Cr**	**C**	**Temp. (°C)**	**Ms^{ε} (°C)**	**SFE mJ/m^2**	**γ**	**ε**	**α**
13.3SFE	18.5	2.10	1.76	-	0.13	540	-30	15.9	69	0	31
7.8SFE	21.0	1.96	1.16	-	0.12	545	-15	14.2	60	0	40
5.0SFE	16.4	2.92	0.79	-	0.19	530	56	6.1	64	30	6
-0.2SFE	18.6	2.14	0.19	-	0.40	520	50	6.9	32	10	58
-1.8SFE	18.5	2.31	0.23	-	0.22	515	77	3.5	34	13	53
-2.1SFE	17.3	2.00	0.27	-	0.14	560	98	0.4	67	14	19
-2.2SFE	14.8	1.60	0.31	-	0.12	555	113	-2.3	64	33	3
0.7SFE	15.9	1.23	-	2.98	0.05	525	119	-2.6	37	33	30

Validation of the calculations shown in Table AII is provided in Figure A1 and Figure A2. It should be noted that the thermodynamic model [63] for predicting Ms^{α} may not work for Mn greater than 15 wt.% and ε-martensite is more likely at these higher manganese levels. After intercritical annealing γ-austenite is enriched in manganese and calculated to contain up to 21 wt. % Mn. It is interesting to note that the 13.3SFE and 7.8SFE alloys have calculated Ms^{ε} temperatures below 0 °C and contain no ε-martensite in their room temperature microstructures as shown in Table AII from XRD analysis as well as shown in the EBSD phase maps in Figure A1. Alloys that have calculated Ms^{ε} temperatures above ambient contain athermal ε-martensite in their room temperature microstructures as shown in Figure 2A for the alloys -1.8SFE and 0.7SFE.

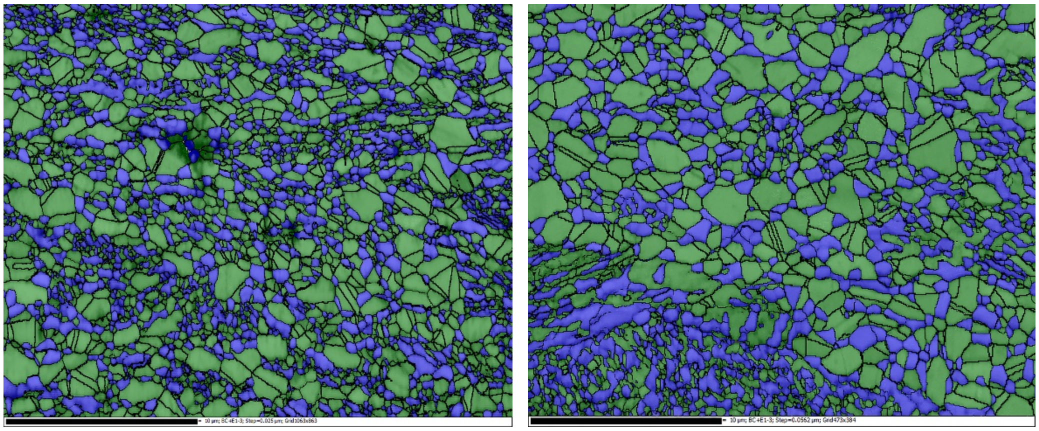

(a) (b)

Figure 1A. Batch annealed EBSD-OIM of the (a) 13.3SFE alloy and (b) 7.8SFE alloy with α-ferrite blue and γ-austenite is green.

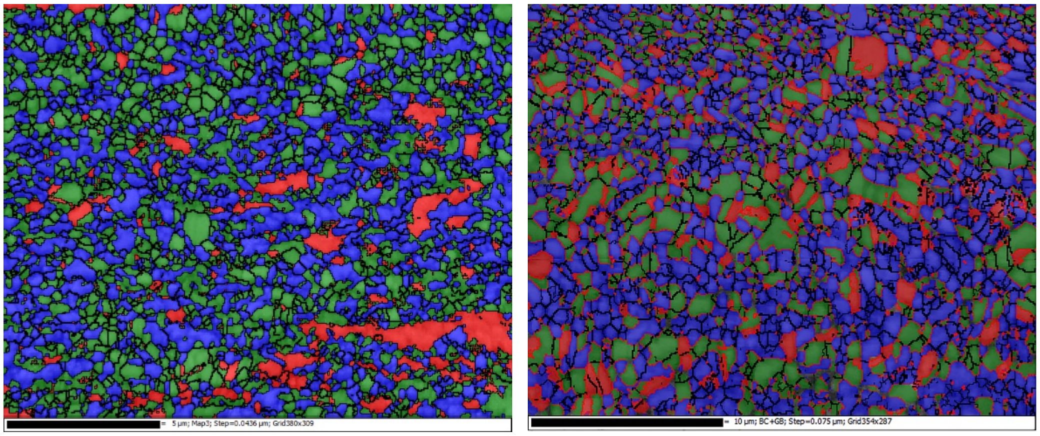

(a) (b)

Figure 2A. Batch annealed EBSD-OIM of the (a) 0.7SFE alloy and (b) -1.8SFE alloy with α-ferrite blue, γ-austenite is green, and ε-martensite is red.

BIBLIOGRAPHY

[1] J. Fekete and J. Hall: NIST Internal Report 6668, National Institute of Standards and Technology, Washington, DC, May 2012.

[2.] C.D. Horvath, and M. Cannon 2012 *Future Material Opportunities and Direction for Lightweighting Automotive Body Structures* [power point slide 17]

[3] Q. Li, Xu. Huang, and W.Huang, *Met. Sci. & Eng.* Vol.662, 2016 pp. 129-135

[4] M.C. McGrath, D.C. Van Aken, N.I. Medvedeva, and J.E. Medvedeva. *Met Trans. A.*, vol. 44A, 2013, pp. 4634-4643

[5] D.C. Van Aken, S.T. Pisarik, M.C. McGrath. *International Symposium on New Development in Advanced High Strength Steel.* Vail 2013, pp. 119-129.

[6] S.T. Pisarik, D.C. Van Aken, K. Limmer, and J.E. Medvedeva. 2014. *AIST2014*. pp. 3013-3023.

[7] A. Dumay, J.P. Chateau, S. Allain, S. Migot, and O. Bouaziz. *Materials Science and Engineering A*, vol. 2008, pp. 184-187

[8] K.R. Limmer, J.E. Medvedeva, D.C. Van Aken, N.I. Medvedeva, *Comp. Mater. Sci.* vol. 99, 2015, pp. 253-255

[9] R.B. Figueiredo, F.L. Sicupira, L.R.C. Malheiros, M. Kawasaki, D.B. Santos, and T.G. Langdon., *Mat. Sci. & Eng A*, vol. 625, 2015, pp.114-118

[10] D. P. Escobar, S. S. F. de Dafe, and D. B. Santos, *Jour. Mater. Research and Tech*, vol. 4, 2015, pp.162-170

[11] O. Grässel, G. Frommeyer, C. Derder, and H. Hofmann, *Jour. Physics IV France,* vol. 7, 1997, pp. 383-388

[12] S. T. Pisarik, and D. C. Van Aken., *Met Trans A*, vol. 45, 2014, pp. 3173-3178

[13] C.C. Kinney, I.Yi, K.R. Pytlewski, A.G. Khachaturyan, N.J. Kim, and J.W. Morris Jr, *Acta Materialia*, vol. 125, 2017, pp. 442-454

[14] S. Shin, M. Kwon, W. Cho, I. S. Suh, and B.C. De Cooman, *Mater. Sci. & Eng.* 2017, vol. 683, pp. 187-194

[15] S.K. Huang, Y.H. Wen, N. Li, J. Teng, S. Ding, Y.G. Xu, *Materials Characterization*, 2008, vol. 59, pp. 681-687

[16] H.S. Yang, J.H. Jang, H.K.D.H. Bhadeshia and D.W. Suh, *CALPHAD*, vol. 36, 2012, pp. 16-22

[17] S. T. Pisarik, and D. C. Van Aken., *Met Trans A*, vol. 47, 2016, pp. 1009-1018

[18] Cohen, G.B. Olson and M. *Met Trans A*, Vol. 7, 1976, pp. 1905-1914.

[19] Cohenn, G.B. Olson and M., *Met Trans A*, Vol. 7, 1976, pp. 1897-1904

[20] A. Holden, J.D. Bolton, and E.R. Petty. *Journal of Iron and Steel Inst* Vol. 209, 1971, pp. 721-728

[21] M. Acet, T. Schneider, B. Gehrmann, and E.F. Wasserman, *Journal De Physique*. Vol. 5, 1995, pp. 379-384.

[22] B.C. DeCooman, and J.G. Speer. Austenite decomposition in Fe-C-X Alloy Systems. Fundamentals of Steel Product Physical Metallurgy. Materials Park : ASM International, 2011, p. 173.

[23] Z. Jicheng, and J. Zhanpeng. *Acta Metallurgia,* Vol. 38, 1990, pp. 425-431.

[24] Anita, V. Raghavan and D. *Met Trans A*, Vol. 27A, 1996, pp. 1127-1132.

[25] Andrews, K.W., *Journal of Iron and Steel Institue* Vol. 203, 1965, pp. 721-727.

[26] C. D. Horvath, C. M. Enloe, J. P. Singh, and J. J.Coryell, *Intl. Symp. On New Developments in AHSS,* “Persistent Challenges to Advanced High-Strength Steel Implementation” Keystone, CO. 2017.

[27] J.F. Enrietto, *Jour. Of the Iron and Steel Inst.* 1966, pp. 252-258

[28] W. Wepner, *Arch. Eisenh.,* 1955, vol. 22, pp. 71-81

[29] D-W. Suh, S-J Park, T-H. Lee, C-S. Oh, and S-J. Kim, *Met Trans A*, 2010, vol. 41A, pp. 397-408

[30] D-W. Suh, J-H Ryu, M-S. Joo, H-S Yang, H.K.D.H. Bhadeshia, *Met Trans A*, 2013, vol. 44A, pp. 286-293

[31] H. Luo, H. Dong, and M. Huang, *Mater. & Design*, 2015, vol. 83, pp.42-48

[32] S. Lee, S-J. Lee, S. Santhosh Kumar, K. Lee, and B.C. De Cooman, *Met Trans A*, 2011, vol. 42A, pp. 3638-3651

[33] Y. Zhang, L. Wang, K. O. Findley, and J. Speer, *Met Trans. A*, 2017, vol. 48A, pp. 2140-2149

[34] J. Han, S-H. Kang, S-J. Lee, and Y-K Lee, *Jour. Alloy & Compound.* 2016, vol. 681, pp. 580-588

[35] J. Han, S-J. Lee, J-G. Jung, and Y-K. Lee, *Acta Materialia*, 2014, vol. 78, pp. 369-377

[36] P.J. Gibbs, E. De Moor, M.J. Merwin, B. Clausen, J.G. Speer, and D.K. Matlock, *Met Trans A*, 2011, vol. 42A, pp. 3691-3701

[37] A. Arlazarov, M. Goune, O. Bouaziz, A. Hazotte, G. Petigand, and P. Barges, *Mater Sci and Eng. A.* 2012, vol. 545, pp. 31-39

[38] P. Rodriguez, *Bull. Mater. Sci* 1984, vol. 6. Pp.653-663

[39] Y.N. Dastur and W.C. Leslie *Met. Trans. A* 1981, vol. 12A, pp. 749-759

[40] S-J. Lee, J. Kim, S.N. Kane, and B.C. De Cooman, *Acta Materialia*, 2011, vol. 59, pp.6809-6819

[41] J. Shi, X. Sun, M. Wang, W. Hui, H. Dong, and W. Cao, *Scripta Mat*, 2010, vol. 63, pp. 815-818

[42] D. M. Field, D.C. Van Aken, *Met Trans A.*, 2016 vol. 47A pp.1912-1917

[43] L. Remy, and A. Pineau *Mater. Sci and Eng.* 1976, vol. 26 pp. 123-132

[44] S. Allain, J.P. Chateau, and O. Bouaziz, *Mater Sci and Eng.* 2004, vol. 387, pp. 143-147

[45] T.H. Lee, E. Shin, C.S. Oh, H.Y. Ha, and S.J. Kim, *Acta Mater.* 2010, vol. 58, 3173-3186

[46] S. Lee, W. Woo, and B.C. De Cooman, *Met. Trans A*, 2016, vol. 47A, pp. 2125-2140

[47] H. Song, S.S. Sohn, J-H Kwak, B-J lee, and S. Lee, *Met Trans A*, 2016, vol. 47A, pp.2674-2685

[48] O. Grässel, L. Krüger, G. Frommeyer, and L.W. Meyer: *International Journal of Plasticity*, 2000, vol. 16, pp. 1391-1409

[49] R. Zhang, W.Q. Ca, Z.J. Peng, J. Shi, H. Dong, and C.X. Huang, *Mater. Sci. & Eng. A*, 2013, vol. 583, pp. 84-88

[50] D.M. Field and D.C. Van Aken, *Proceedings of the Intl. Symp. on New Developments in Advanced High-Strength Steels*, Keystone, Colorado, 2017

[51] S.J. Lee, S.W. Lee, B.C. De Cooman: *Int. J. Mater. Res.*, 2013, vol. 104, pp. 423–29.

[52] X-S. Yang, S. Sun, H-H Ruan, S-Q Shi, and T-Y. Zhang, *Acta Materialia*, 2017, vol. 136, pp. 347-354

[53] B.C. De Cooman, P. Gibbs, S. Lee, and D.K. Matlock, *Met Trans A*, 2013, vol. 44A, pp. 2563-2572

[54] R. Skolly, ArcelorMittal personal communication.

[55] P.P. Suikkanen, V.T.E. Lang, M.C.Somani, D.A. Prter, and L.P. Karjalainen: *ISIJ International*, 2012, vol. 52, pp. 471-476

[56] Z, Li-Juan, W. Di, and Z. Xian-ming: *Jour. Iron and Steel research international*, 2007, vol. 14, pp. 61-65

[57] L.J. Zhu, D. Wu, X.M. Zhao *Acta Metall.* 2008 vol. 21, pp. 163-168

[58] M.C. Somani, L.P. Karjalainenm D.A. Porter, and R.A. Morgridge: Proc. Int. Conf. on Thermomechanical Processing Mechanics: Microstructures and Controls, University of Sheffield, Sheffield GB, (2003), 436.

[59] S.F. Medina, and J. E. Mancilla, *ISIJ Int.* 1996, vol. 36, pp.1036-1070

[60] S.F. Medina, and A. Quispe: *ISIJ Int.* 2001, vol. 41, pp.774-780

[61] K.R. Limmer J.E. Medvedeva, D.C. Van Aken, N.I. Medvedeva *Computational Materials Science*, DOI: 10.1016/j.commatsci.2014.12.015

[62] S.T. Pisarik and D.C. Van Aken, *Met Trans A.*, Vol. 47A 2016 pp1009-1018

[63] D.M. Field, D.S. Baker, and D.C. Van Aken, *Met Trans A*, 2017, DOI. 10.100/s 11661-017-4020-2

VITA

Daniel Morye Field was born in 1985 in Santa Monica California. He attended the Ventura County Community Colleges from 2009 to 2011 and continued his education at Missouri University of Science and Technology in the fall of 2011 and received his B.S. in Metallurgical Engineering (Dec. 2013). Upon graduation he attended the Missouri University of Science and Technology in 2014 studying the medium-Mn two-stage TRIP steels for automotive applications. In 2014 he was awarded the Chancellors Fellowship and in 2015 won first place in the Chancellors Fellowship Competition. In 2016 he was awarded the G.A.A.N.N fellowship from the U.S. Department of Education to continue his studies as a Ph.D. candidate. He received his Ph.D. in Metallurgical Engineering from Missouri University of Science and Technology in May 2018 under Dr. David. C. Van Aken.